Eindhoven University of Technology

MASTER

A planar passive electromagnetic deflector for millimetre-wave frequencies

Kastelijn, M.C.T.

Award date:
2007

Link to publication

Eindhoven University of Technology
Department of Electrical Engineering
Telecommunications and Electromagnetism

A Planar Passive Electromagnetic Deflector for Millimetre-Wave Frequencies

M.C.T. Kastelijn

August 2007

Master of Science Thesis
Project period: November 2006 - August 2007
Department: Radiocommunications (ECR)
Supervisors:
ir. J.A.G. Akkermans
dr. P.F.M. Smulders
Graduation professor:
Prof. dr. E.R. Fledderus

Contents

1 Introduction 1
- 1.1 SiGi-Spot project 1
- 1.2 Antenna configuration 1
- 1.3 Extended antenna coverage 1
  - 1.3.1 Conformal array 2
  - 1.3.2 Reflector antenna 2
  - 1.3.3 Dielectric lens antenna 2
  - 1.3.4 Reflectarray antenna 2
  - 1.3.5 Transmitarray antenna 3
- 1.4 Proposed approach 3
- 1.5 Deflector-based configuration 4
- 1.6 Structure of the thesis 4

2 Design of the deflector 7
- 2.1 Introduction 7
- 2.2 Deflector element 7
- 2.3 Deflecting behaviour 7
  - 2.3.1 Scenarios 9
- 2.4 Source/deflector model 9
- 2.5 Source/deflector simulations 11
- 2.6 Scenario dependent deflector design 12
- 2.7 Conclusion 13

3 Generic structures on a grounded dielectric slab 15
- 3.1 Introduction 15
- 3.2 General field solution 15
  - 3.2.1 Maxwell's equations and constitutive relations 15
  - 3.2.2 Vector potential and Green's function 16
  - 3.2.3 Helmholtz equation and boundary conditions 17
- 3.3 Field solution of the grounded dielectric slab 18
  - 3.3.1 Configuration 18
  - 3.3.2 Vector potential and Green's function 19
  - 3.3.3 Helmholtz equation and boundary conditions 19
  - 3.3.4 Spectral domain description 20
  - 3.3.5 Solution 21
  - 3.3.6 Numerical approach 24
  - 3.3.7 Example 24
- 3.4 Generic structures using the Method of Moments 27
  - 3.4.1 Formulation 27
  - 3.4.2 Basis Functions 30
  - 3.4.3 Input impedance 31
- 3.5 Example problem: microstrip dipole 32

3.6 Conclusion 35

4 **Optimization of antenna structures** **37**
4.1 Introduction 37
4.2 Approach 37
4.3 Cost function 37
4.3.1 Definition 37
4.3.2 Least squares cost function 38
4.3.3 Derivatives 38
4.4 Example: microstrip dipole 39
4.4.1 Cost function 39
4.4.2 Taylor approximation 40
4.4.3 Results 41
4.5 Conclusion 41

5 **Analysis of a canonical element** **43**
5.1 Introduction 43
5.2 Configuration 43
5.2.1 Source 43
5.3 Field analysis 44
5.3.1 Extinction theorem 44
5.3.2 Similar problem 44
5.4 MoM approach 47
5.5 Transmitted power for a typical element 48
5.6 Optimisation 49
5.6.1 Cost function and derivatives 49
5.6.2 Results 50
5.7 Conclusion 50

6 **Realisation of a deflector** **53**
6.1 Introduction 53
6.2 Phase-shifting deflector element 53
6.2.1 Variable patch size 53
6.2.2 Transmission lines 54
6.3 Design of the deflector 55
6.4 Simulation results 56
6.5 Conclusion 56

7 **Measurement and simulation results** **57**
7.1 Introduction 57
7.2 Construction of the deflectors 57
7.3 Measurement setup 57
7.3.1 Calibration 58
7.4 Results 58
7.5 Discussion 59
7.6 Conclusion 59

8 **Conclusions and recommendations** **61**
8.1 Conclusions 61
8.2 Recommendations 62

A **Plane waves and Fourier transform** **65**

B **Antenna Parameters** **67**

C Taylor approximation **69**

D Plane wave incident on a grounded dielectric slab **71**

E Spectral domain Green's functions of the grounded dielectric slab with magnetic sources **73**

F Complex element-wise product **75**
- F.1 Definition 75
- F.2 Properties 75
  - F.2.1 Commutativity 75
  - F.2.2 Associativity 75
  - F.2.3 Distributivity 76
  - F.2.4 Derivation 76
  - F.2.5 Relation with ordinary modulus 76

Acknowledgments **77**

Bibliography **79**

List of Figures

1.1 Proposed configuration 5

2.1 Functional schematic of the phase shifting element 8
2.2 Linear phase shift along a series of deflector elements 8
2.3 Piece-wise linear phase shift 9
2.4 Source/deflector model schematic 9
2.5 Scenario 1; high directivity/low steerability 9
2.6 Scenario 2; low directivity/high steerability 9
2.7 Parameters of the deflector 11
2.8 Normalised distance over which contributing elements are located (○); 2^{nd} derivative of phase-position curve [rad/m^2] (×); scaled phase-position curve [rad] (△) 12
2.9 Trade-off between deflector size ($W_{deflector}$), steerability ($\Delta\gamma_{out}$) and outgoing beam width ($BW_{-3dB,out}$); colour indicates deflector size 14
2.10 Trade-off between deflector size ($W_{deflector}$) and outgoing beam width ($BW_{-3dB,out}$); scenario 1 (blue) and scenario 2 (red) 14
2.11 Radiation pattern of outer steering angles for scenario 1; $\gamma_{l,out} = 82^\circ$ ($-$) and $\gamma_{l,out} = 97^\circ$ ($- \cdot$) 14
2.12 Radiation pattern of outer steering angles for scenario 2; $\gamma_{l,out} = 60^\circ$ ($-$) and $\gamma_{l,out} = 110^\circ$ ($- \cdot$) 14

3.1 Configuration of the grounded dielectric slab 18
3.2 Evaluation of the imaginary part of E_{2x} as function of K_ρ; frequency (f) as parameter with $z = 0.2$ mm (left) and observation height above the slab (z) as parameter with $f = 60$ GHz (right) 25
3.3 Evaluation of the imaginary part of E_{2y} as function of K_ρ; frequency (f) as parameter with $z = 0.2$ mm (left) and observation height above the slab (z) as parameter with $f = 60$ GHz (right) 25
3.4 Electric field in the yz-plane (x-component); real part (left) and imaginary part (right) 27
3.5 Electric field in the yz-plane (y-component); real part (left) and imaginary part (right) 28
3.6 Layout of rooftop basis functions 31
3.7 Source model in the circuit domain 32
3.8 Source model in the electromagnetic domain 32
3.9 Current distribution the dipole; magnitude (left) and angle (right) 35
3.10 Directivity of the dipole; θ-cut; $\phi = 0^\circ$ (left) and $\phi = 90^\circ$ (right) 36
3.11 Input impedance of the dipole; real part (above) and imaginary part (below) . . . 36

4.1 Original cost function and Taylor approximation of several orders 42

5.1 Configuration of the canonical element in 3D 44
5.2 Front view of the canonical element 44

5.3 Extinction theorem; initial situation (left); $\vec{0}$-field in V_1 due to added surface currents (right) 45
5.4 Space decomposition of the similar problem 45
5.5 Similar problem configuration after replacing V_s with PEC and removing the non-radiating electric surface currents 46
5.6 Transmitted power for the typical deflector element 49
5.7 Taylor approximation of the cost function; cost function (-⊖-), 1^{st}-order approximation (− −), 2^{nd}-order approximation (− ·), 4^{th}-order approximation (· ·) and 8^{th}-order approximation (−) 50
5.8 Transmitted power for the optimised deflector element 51

6.1 Patch-patch-slot-patch configuration 54
6.2 Transmission properties of the patch-patch-slot-patch configuration 54
6.3 Stack of the deflector element 54
6.4 Initial design of the deflector element 54
6.5 Compact design of the deflector element 55
6.6 Final design of the deflector element 55
6.7 Deflector elements; −120 degrees (left), 0 degrees (middle) and 120 degrees (right) 55
6.8 Radiation pattern (3D); $f = 60$ GHz 56
6.9 Radiation pattern (θ-cut, $\phi = 0$ deg); $f = 57$ GHz (− −), $f = 60$ GHz (−) and $f = 63$ GHz (− ·) 56

7.1 Measurement setup; conical horn not shown 58
7.2 Gain of deflector A (deflecting plane, $f = 60$ GHz); measured (—); simulated (− −) 59
7.3 Gain of deflector B (deflecting plane, $f = 60$ GHz); measured (—); simulated (− −) 59
7.4 Normalised gain of both deflectors; measured (—); simulated (− −) 60
7.5 Measured gain of both deflectors; deflector A (− −); deflector B (—) 60

C.1 False validation of a Taylor approximation 70

D.1 Electric field components at the dielectric slab 71

Chapter 1

Introduction

1.1 SiGi-Spot project

Nowadays a large number of media applications are in need for ultra-broadband wireless transmission over short distances. Current wireless LAN technology is is not suitable for this, because the available capacity is limited by bandwidth restrictions in the conventional frequency bands. The SiGi-Spot project [47] addresses the use of the 60 GHz band, in which more than 5 GHz of spectral space has been allocated for licence-free use. By using this resource, data rates in the order of gigabits per second become feasible. Typical applications that can be foreseen are in the area of consumer electronics, e.g., the wireless connection between a DVD player and a plasma screen. The high free-space loss at 60 GHz makes this band very suitable for indoor communication, but at the same time requires high gain and highly steerable antennas.

1.2 Antenna configuration

The proposed antenna configuration in the SiGi-Spot project consists of a planar array of balanced-fed aperture-coupled patch antennas [2, 4]. An important feature of this design is the ability to electronically steer a beam with high directivity towards a desired direction. The design can be realised in a printed circuit board technique. Therefore, it has the advantages of low cost and easy integration. Another important aspect of the design is its wideband behaviour, while retaining good efficiency. However, a typical planar antenna array has limited steering capabilities due to a non-uniform element pattern. It is not possible to obtain beams with high directivity at angles far from broadside, due to the low gain of the antenna elements at these angles. Additionally, a planar array can suffer from scan blindness, which limits the scan range as well [40]. These are the main reasons that the coverage of a single antenna array is limited. We are interested in extending the coverage of the currently proposed antenna configuration, while retaining the advantages of low cost, easy integration and wideband behaviour with good efficiency. Moreover, we would like to have a customisable design, so that the coverage of the antenna system can be tailored to the application in mind.

1.3 Extended antenna coverage

Several antenna configurations are known that are able to achieve a larger coverage compared to a planar array of patch antennas. For the application in mind however, they should also meet the specifications mentioned in the previous section, regarding cost, integration, bandwidth and efficiency.

1.3.1 Conformal array

Instead of a planar array of source elements, a conformal array of antenna elements [33] could be used. In a conformal array, multiple source elements are placed on an arbitrary shape, for example a sphere or a cylinder. In this way, every direction of interest is covered by a certain group of source elements. In [27], microstrip patch antennas are placed on a cylindrical surface to produce an omni-directional radiation pattern. By applying different feed signals to each element, it is possible to radiate energy into different directions with beams of high directivity. In [18, 5], two algorithms are described to determine appropriate feed signals to obtain desired beam patterns. Disadvantages of such conformal arrays however, are relatively high production costs and the fact that they are not easy to integrate. Another approach might be to use several planar antenna arrays, arranged into a 3D configuration, for example in the shape of a pyramid. Each array is able to cover part of space. Production costs are lower compared to shapes with smooth curves and the design is easier to integrate, but a problem is the extensive feed network, required to feed each of the elements separately. Especially at the edges of the planar arrays, interconnection problems can occur.

1.3.2 Reflector antenna

Another option is to use a (parabolic) shaped reflector in combination with a steerable source antenna. A good overview of reflector antennas is given by [45]. Although a reflector antenna can be a simple solution, the source antenna or the reflector itself causes shadowing, and it is cumbersome to customise the reflector for different applications.

1.3.3 Dielectric lens antenna

The dielectric lens antenna consists of a source antenna surrounded by dielectric material, which is able to focus or bend the source radiation towards a certain direction. A good overview of the different types of lens antennas is given in [20]. A significant amount of work on lens antennas has been performed for millimetre-wave applications. For example, the designs presented in [17, 15, 16] achieve an omni-directional coverage. It is also possible to design lens antennas that form a beam of high directivity towards a fixed desired direction [13, 54, 9], but this type of lens antenna is not able to focus or steer radiation towards different directions. Another type of lens antenna, consisting of a steerable source antenna array and a lens with multiple focus points [54, 43], is able to steer towards different directions and could be a suitable solution. Disadvantages of lens antennas are relatively high internal reflections [51]. These reflections can be lowered by using appropriate matching layers, but this increases the production costs of the lens.

1.3.4 Reflectarray antenna

Another commonly used configuration to extend coverage is based on a reflectarray [7]. Like the reflector antenna, radiation of a steerable source is reflected towards a desired direction. Instead of a parabolic-shaped reflector, a planar array of phase-shifting elements can be used. These elements reflect incident radiation, while performing a certain phase shift. This way, the phase distribution of the reflected wave is changed and can be steered towards a desired direction. In [23, 8, 26], the phase-shifting property of the element is achieved by varying length stubs and more recently, in [39, 41], by patches of variable size. The extensive use of reflectarrays to extend coverage of a steerable antenna system is mostly due to the low cost and the fact that a reflectarray is highly customisable. There are also disadvantages however. Varying the size of the patches to achieve the phase-shifting property of the elements changes the resonance frequency of the patches, causing the reflectarray to be limited in bandwidth. An improvement has been made in [14], where two layers of patches are used, to create a reflectarray that allows for more freedom in the design. This way the bandwidth of the reflectarray can be improved. Two other disadvantages of reflectarrays are the fact that only that part of the environment can be covered, that is on the reflecting side of the reflectarray, and the fact that the source causes shadowing.

1.3.5 Transmitarray antenna

Another type of antennas is the class of transmitarrays. Transmitarrays consist of an array of receiving and transmitting antenna elements, located back-to-back on opposite sides of the structure [29]. Transmitarrays can be active or passive. In an active transmitarray, RF circuitry and active devices are placed in between the receiving and transmitting antenna elements to amplify the signal. Active transmitarrays are also known as transmission-type spatial power combiners, first reported in [49]. Many significant advancements have since been made, leading to active transmitarrays for frequencies in the range of 10 GHz and above. For example, in [24], arrays of anti-resonant slot antennas are combined with active devices, yielding an active transmitarray operating at 35 GHz. In [35], arrays of coplanar waveguide (CPW)-fed microstrip patch antennas are used to create a passive and an active transmitarray operating at 10 GHz. In [34], an active transmitarray is presented, consisting of microstrip patch based structures using through-plate coaxial transitions, operating at 34 GHz. These designs use a (hard) horn feed, which produces an approximated plane wave to feed the transmitarray, and use elements which apply identical phase shifts. This way, the active elements of the transmitarray transmit the amplified signals in phase and thereby achieve increased gain.

A transmitarray antenna can be used for beam forming purposes if it is constructed of phase-shifting elements [29]. Such a transmitarray is similar to the reflectarray in the sense that it uses these phase-shifting elements to change the phase distribution of the incident wave. Unlike the reflectarray antenna, which reflects the electromagnetic wave from the surface, incident waves are transmitted through the surface. In this comparison, an advantage of a transmitarray is that shadowing by the source is avoided, because the incident wave is transmitted away from the source array system. However, the elements of a transmitarray are more complicated than the elements of a reflectarray, because they have to provide the transmission and apply the required phase-shift to the incident wave at the same time, whereas in a reflectarray, the elements only have to apply the required phase-shift to the incident wave. The incident wave is totally reflected due to the presence of a ground plane.

Some studies for suitable array elements have been performed. In [29], aperture-coupled microstrip patch antennas are used which achieve a bandwidth of 1.9% at a frequency of 1.8 GHz. In [25], microstrip patches and coupling slots are used, which obtain a 1 GHz bandwidth at a frequency of 35 GHz. In [10] tapered slot antennas are used in combination with active devices, to achieve gain in the frequency range of 8-11 GHz. In [50], edge-fed and aperture-coupled stacked patch antennas are used. The aperture-coupled stacked patch element achieves a bandwidth of more than 5 GHz at a frequency of 10 GHz. In [38], the concept of a flat lens is explored, from the view of a frequency selective surface (FSS) [37, 32]. A frequency selective surface consists of elements, which transmit waves only within a selected frequency band. In [38], a phase-shifting property is added to the elements of an FSS. This way, a passive transmitarray capable of beam forming is obtained. The elements are constructed of arrays of aperture-coupled microstrip patches, with varying length striplines in between to provide a custom phase shift. Simulations show 90% transmission in a 5% bandwidth around a frequency of 8 GHz. The same concept of an electromagnetic lens has already been described in a patent, dating from 1961 [28], in which is indicated that the characteristics of the lens can be varied by adjusting the electrical length of transmission lines. It is also indicated that, using this principle, it is possible to create a lens which is able to produce a scanning beam of radiation.

1.4 Proposed approach

The alternatives presented in the previous section all have their advantages and drawbacks. A conformal array on a curved surface can have good performance, but is costly and not easy to integrate. Several planar arrays, arranged in a 3D structure can be more cost-effective, but suffer from interconnection problems. A reflector in combination with a steerable source antenna causes shadowing and is not very customisable. Lens antennas exist in a variety of forms. Omnidirectional or fixed-directional lenses are not suitable for our application in mind. A steerable source antenna in combination with a lens with multiple focus points could be a suitable solution. A drawback of a lens is that internal reflections are relatively high and using matching layers to reduce internal reflections is expensive. Designs based on reflectarrays are highly customisable and possibly low-cost and easy to integrate. To this end, microstrip patches can be used as phase-shifting elements. Due to a reflecting ground plane, a reflectarray is nearly 100% efficient. However, reflectarrays tend to be limited in bandwidth and the source causes shadowing. Transmitarrays possibly have the same advantages as reflectarrays, and the added advantage that the source does not cause shadowing. Like reflectarrays, they are highly customisable and can be low-cost and easy to integrate. Care should be taken, however, in designing a wideband, efficient phase-shifting element. Active transmitarrays can increase the gain of the source beam, but passive transmitarrays are inherently easier to design, because they do not require active elements. In this thesis, an attempt is made to design a passive transmitarray, which is able to achieve extended coverage and meets the required specifications of low-cost, easy to integrate, wideband performance with good efficiency. To meet these specifications, a suitable choice would be to design phase-shifting elements based on the proposed balanced-fed, aperture-coupled patch antennas presented in [2].

1.5 Deflector-based configuration

Based on a passive transmitarray, we present a flexible antenna configuration, which is able to achieve extended coverage and can be customised for multiple scenarios, with the same effort and low manufacturing costs. Because this passive transmitarray is used to deflect electromagnetic waves, radiated by the source, towards a new direction, it will be called *deflector*. It is used in combination with a steerable source planar array of balanced-fed aperture-coupled patch antennas. The proposed configuration, which consists of a source and a deflecting part, is shown in Fig. 1.1. This figure shows a pyramid-shaped deflecting part, which can be constructed from multiple planar deflectors. The steerable source can focus power, in the form of an electromagnetic wave, on a certain confined area of a deflector. Depending on which area the power is focused, the deflector bends this wave towards a certain direction. In this way, power can be emitted towards directions that are out of reach of the source itself. Also, the power can be focused towards a certain direction, so narrower beams with higher directivity can be realised.

It is assumed that the source in Fig. 1.1 is able to steer along the entire ϕ-range and that there is no need to influence this behaviour. The deflector can however alter or extend the coverage by deflecting along the θ-direction.

1.6 Structure of the thesis

In Chapter 2, the design of the deflector is considered. It is explained that the deflector consists of phase-shifting elements, and how these elements are able to deflect electromagnetic waves. It is also explained that a trade-off exists between directivity and steerability of the deflector. A model is given for the deflector in combination with a steerable source. Using this model, it is investigated how the deflector should be designed to realise a certain desired behaviour. Two possible designs and simulation results are given.

To model a simplified alternative for the final deflector element, the modelling and analysis of generic planar structures on top of a dielectric slab is considered in Chapter 3. Starting from Maxwell's equations, the Green's function of the dielectric slab is found. Using this Green's function, the field solution of a point source on top of the slab is given as an example. The field solution of generic structures on top of the slab is found using a Method of Moments (MoM)

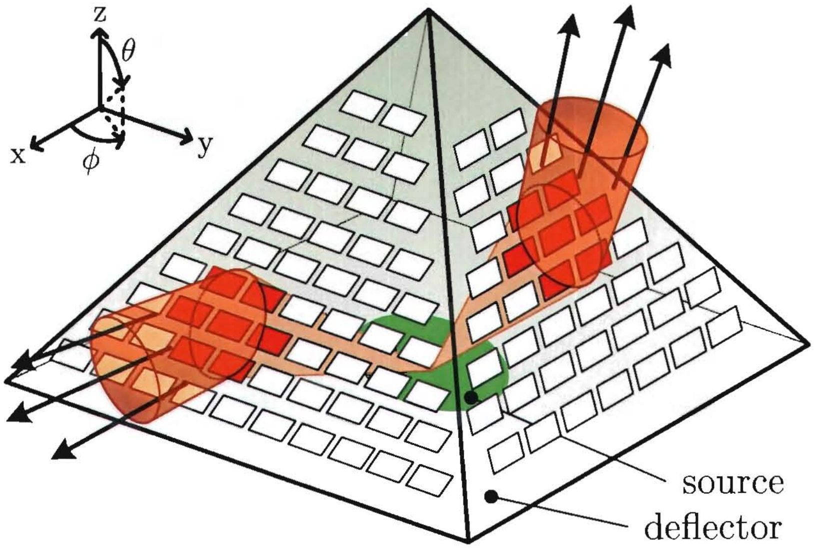

Figure 1.1: Proposed configuration

approach. As an example, the radiation pattern and input impedance of a microstrip dipole is given.

To obtain an optimised design for the deflector element, an optimisation method is presented in Chapter 4. This method is able to find a global optimum using a Taylor expansion of a cost function. The method is explained and an example is given.

In Chapter 5, the deflector element is studied by introducing a simplified alternative for the final element. This canonical element is modelled with help of the results presented in Chapter 3 and its transmission properties are calculated as function of frequency. Furthermore, the element is optimised using the method presented in Chapter 4.

In Chapter 6, a deflector is realised. The final phase-shifting deflector element, based on the canonical element of Chapter 5, is introduced. The design of a deflector, consisting of these phase-shifting elements, is given and simulation results are presented.

To verify the performance of the deflector, two real deflectors are constructed in Chapter 7. Measurements are performed and the results are compared to simulation results.

Finally, in Chapter 8, a summary and conclusions of the work and recommendations for further research are given.

Chapter 2

Design of the deflector

2.1 Introduction

The deflector is a two-sided structure, able to receive incident RF power on its *downside* and emit this power on its *upside*. At the downside, RF power is incident on the deflector in the form of an EM wave, which has a certain phase distribution along the deflector's surface. The received power is transferred through the deflector and emitted in the form of an EM wave at the upside. The deflector is designed to change the phase distribution at the downside into the desired phase distribution at the upside. The phase distribution at the upside determines the steering and/or focusing behaviour. This behaviour is called *deflecting* from this point on. In order to extend coverage, the deflector should be designed for a suitable centre steering angle and steerability, which is the maximum deviation from the centre steering angle.

The deflector consists of phase-shifting elements. This is explained in Section 2.2. The relation between phase distribution at the upside and deflecting behaviour is explained in Section 2.3. This behaviour is modelled in Section 2.4. Simulation results for two designs are given in Section 2.5 and 2.6.

2.2 Deflector element

The deflector applies a phase shift, that varies along the surface. To create this varying phase shift, the deflector is constructed of multiple finite-sized, passive, phase shifting elements. Each element applies an appropriate phase shift. This is shown in Fig. 2.1. An EM wave arrives at the surface with a certain phase distribution. At the downside of element 1, the phase is equal to $\varphi_{1,down}$. The received RF power is transferred to the upside of the element, while a phase shift of $\Delta\varphi_1$ is applied. At the upside, it is emitted in the form of an EM wave. The same principles apply to element 2, which applies a phase shift of $\Delta\varphi_2$. The difference between the phase shifts at the upside of the elements determines the phase distribution at the upside of the deflector, which in turn determines the deflecting behaviour.

2.3 Deflecting behaviour

As mentioned in the previous section, the phase distribution at the upside of the deflector determines the deflecting behaviour. There is a trade-off between directivity and steerability, which is clarified in the remainder of this section. In Chapter 1 it has been explained, that the deflector only needs to deflect along the θ-direction. Therefore, only the 1-dimensional case is considered in the present analysis. To steer towards a certain θ-direction θ_{st}, a phase shift ($\Delta\varphi_k$) can be applied along a series of elements $k \in 1 \ldots K$, with inter element distance d, resulting in a certain phase distribution at the upside ($\Delta\varphi_{k,up}$). This is depicted is Fig. 2.2. The emitted EM waves add in

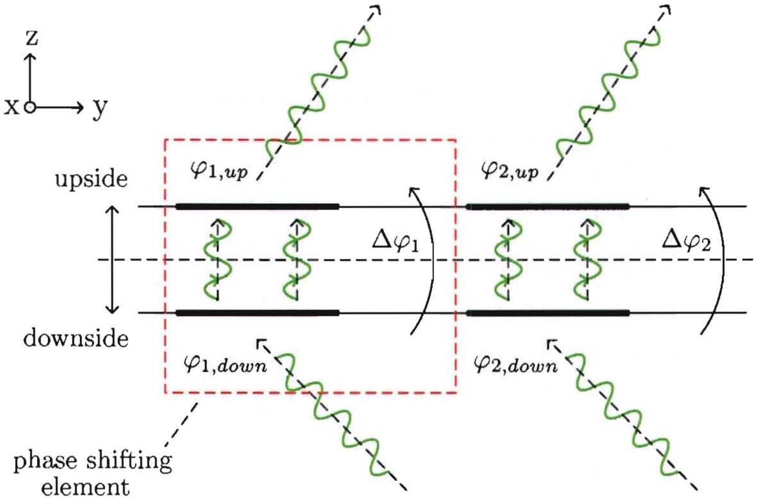

Figure 2.1: Functional schematic of the phase shifting element

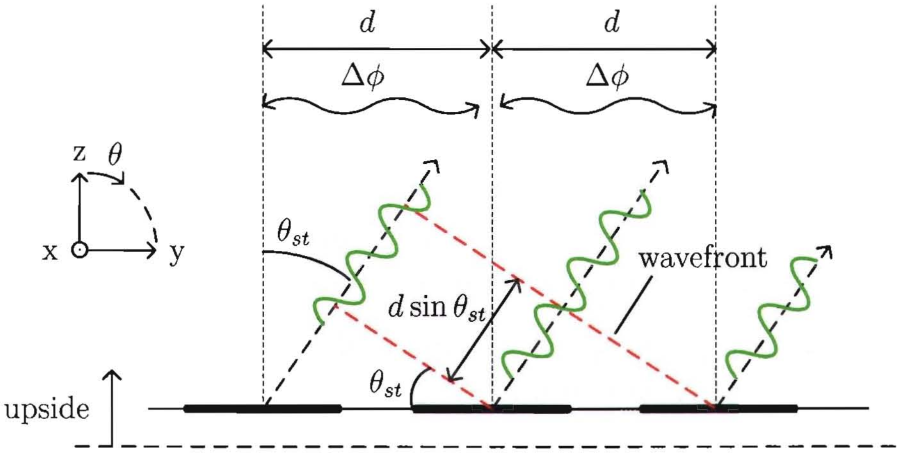

Figure 2.2: Linear phase shift along a series of deflector elements

phase in the direction of θ_{st}, if for every element k holds

$$\frac{kd}{\lambda}\sin\theta_{st} = \frac{\Delta\varphi_{k,up}}{2\pi} + n, \qquad n \in \text{Integer} \tag{2.1}$$

because towards that direction, the difference in phase due to the path length difference $kd\sin\theta_{st}$ of the contributing waves is exactly compensated by the impressed phase shift $\Delta\varphi_{k,up}$. The relative phase at the upside of an element as function of that element's position is called the *phase-position curve*. Eq. (2.1) results in a linear phase-position curve if $\Delta\varphi_{k,up} = k\Delta\varphi_{up}$. As mentioned in Chapter 1, the deflector is able to steer the RF power towards a certain direction, depending on which area at the downside is focused on. If the deflector is to steer to multiple angles $\theta_{st}^{(n)}$, $n = 1\dots N$, then for each angle $\theta_{st}^{(n)}$, a group of elements exists, with among them a corresponding relative phase shift of $\Delta\varphi^{(n)}$. In this case, the phase-position curve is piece-wise linear, having a linear part with slope $\Delta\varphi^{(n)}/d$ for each steering angle $\theta_{st}^{(n)}$. This is depicted in Fig. 2.3 for three steering angles. If more steering angles are defined, less elements per steering angle can be used on a fixed sized deflector with fixed sized elements. Therefore, a trade-off between directivity and steerability of the deflector exists. To steer across a continuous range of angles $\theta^{(1)} \leq \theta_{st} \leq \theta^{(2)}$,

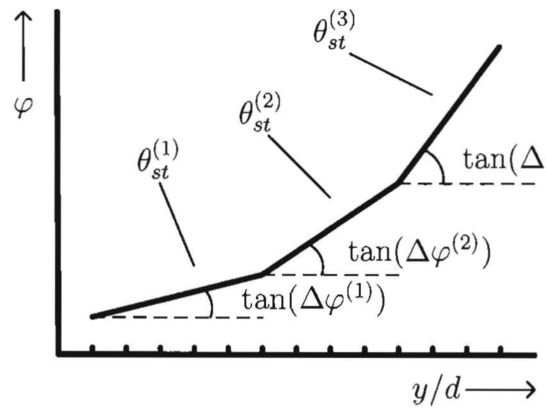

Figure 2.3: Piece-wise linear phase shift

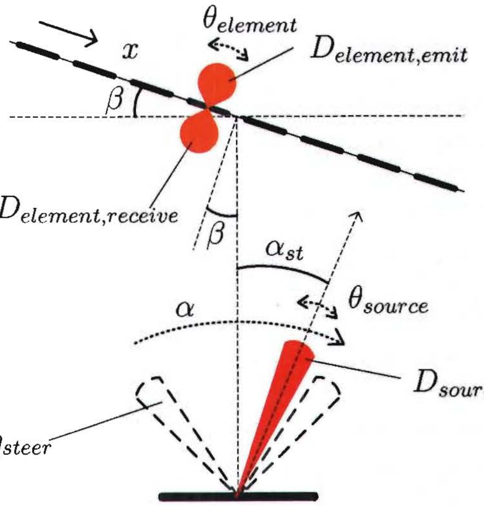

Figure 2.4: Source/deflector model schematic

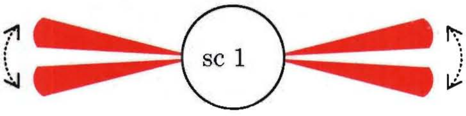

Figure 2.5: Scenario 1; high directivity/low steerability

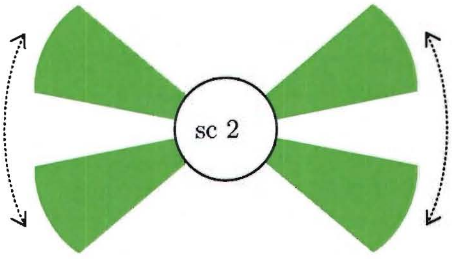

Figure 2.6: Scenario 2; low directivity/high steerability

a smooth phase-position curve is used, with a slope varying from $\Delta\varphi^{(1)}/d$ to $\Delta\varphi^{(2)}/d$.

2.3.1 Scenarios

In the design of the deflector, there is a trade-off between directivity and steerability, as explained in detail in the previous Section. Some applications may require an antenna setup that achieves high directivity at the cost of steering flexibility. This case is called *scenario 1.* Other applications may require steerability in all directions and can afford low directivity. This is called *scenario 2.* These scenarios are shown in Fig. 2.5 and 2.6. Each scenario requires its own deflecting behaviour, so for each scenario the required phase shift distribution is different. What phase shift distribution is suitable for a particular scenario, is investigated with the help of a model described in Section 2.4 and accompanying simulations in Section 2.5.

2.4 Source/deflector model

The behaviour of the deflector is modelled in combination with a steerable source, as shown in Fig. 2.4. The model consists of a steerable source and a deflector, which is made up of a series of deflector elements. The source has the following properties:

- The source beam directivity ($D_{source}(\theta_{source})$), which is defined as the amount of power radiated by the source in the direction of θ_{source}, relative to the amount radiated by an isotropic radiator. θ_{source} is defined relative to α_{st}, the angle the source is steered to;

- The source steering efficiency ($\eta_{steer}(\alpha)$), which is defined as the total amount of power radiated by the source when it is steered to the direction α, relative to the total amount of power radiated when steered to the broadside direction ($\alpha = 0$).

The deflector is situated above the source at a normalised height of 1, tilted under an angle β. The position on the deflector is indicated with $x \in X$, where X denotes the 1-dimensional domain over which the deflector extends, with $x = 0$ being the position straight above the source. The deflector elements receive power on the downside and emit that power on the upside. A deflector element has the following properties:

- The element receive directivity ($D_{element,receive}(\theta_{element})$);
- The element emit directivity ($D_{element,emit}(\theta_{element})$);
- The element size ($W_{element}$).

The power transfer efficiency ($\eta_T(x)$) is defined as the relative amount of power received in the deflector as function of position x, if the source is steered towards position x, which is under an angle α_{st}. It is equal to

$$\eta_T(x) = \eta_{steer}(\alpha_{st}) \cdot \eta_{element,receive}(\theta_{element}), \tag{2.2}$$

where both arguments α_{st} and $\theta_{element}$ are depending on x and β. The path loss difference is not taken into account, because it is assumed to be small among the group of elements that is focused on. The deflector is infinite in size, although only a finite part of it is used. This is depicted in Fig. 2.7. For steering purposes, only the part of the deflector is used, where the power transfer efficiency is greater than some minimum. The domain X_{steer} is defined as

$$X_{steer} = \left\{ x \in X \;\middle|\; \eta_T(x) \geq \eta_{T,min} \right\}, \tag{2.3}$$

where $\eta_{T,min}$ is defined as the minimum power transfer efficiency that is still considered acceptable for the outer steer angles, γ_l and γ_h. The lower limit of X_{steer} is denoted by x_l and the upper limit by x_h. The angles α_l and α_h are defined as the angles the source steers to, in order to emit the maximum amount of power on the deflector towards positions x_l and x_h, respectively. Furthermore, the angles α_{min} and α_{max} are defined as

$$\alpha_{min} = \alpha_l - D_{beam,-3dB}/2, \tag{2.4}$$

$$\alpha_{max} = \alpha_h + D_{beam,-3dB}/2, \tag{2.5}$$

where $D_{beam,-3dB}$ is defined as the -3dB beam width of the source. The part of the deflector that is used is defined by $X_{deflector}$, which is equal to

$$X_{deflector} = \left\{ x \in X \;\middle|\; x_{min} \leq x \leq x_{max} \right\}, \tag{2.6}$$

where x_{min} and x_{max} are defined as the positions on the deflector, which correspond to the angles α_{min} and α_{max}, respectively.
Within X_{steer}, the phase-position curve has a varying slope for the purpose of steering. For $x \leq x_l$, the slope of the curve is equal to the slope at x_l and for $x \geq x_h$, the slope of the curve is equal to the slope at x_h. From x_l through x_h, the change in slope of the phase-position curve allows the deflector to deflect RF power towards angles γ_l through γ_h. The elements within X_{steer} that are illuminated by the source beam do not produce a linear phase shift among them at the upside of the deflector. The outgoing beam width is determined by the variation in slope of the phase-position curve among the contributing elements. An element is defined as contributing if it is illuminated by a significant amount of energy. This is the case if it is located within the incident -10 dB beam width of the source. The amount of contributing elements is dependent on the position on the structure between x_l and x_h that the source steers to. The more elements are contributing, the larger the variation of this slope and the larger the outgoing beam width. Therefore, in order to

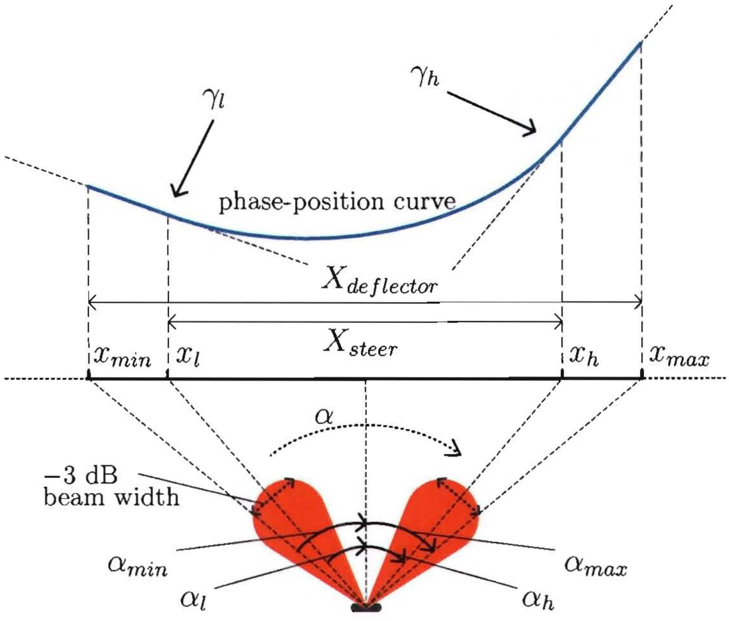

Figure 2.7: Parameters of the deflector

obtain a constant outgoing beam width over the entire range of steering angles, the local increase or decrease in slope of the phase-position curve should be inversely proportional to the number of contributing elements. This is depicted in Fig. 2.8, which shows typical curves for a deflector under a positive tilt angle $\beta = 45°$. The ○-marked curve shows the normalised distance over which contributing elements are located ($d_{contributing}$). The ×-marked curve shows the second derivative, i.e. the increase or decrease in slope, of the phase-position curve, which is inversely proportional to the incident beam width. The first derivative or slope of the phase-position curve is not shown. It is found by integrating the ×-marked curve with respect to x and scaling it in such way, that the endpoints of the curve correspond to the outer steering angles γ_l and γ_h. The △-marked curve is the actual phase-position curve, found by integrating the first derivative with respect to x.

2.5 Source/deflector simulations

The model of Section 2.4 is used to simulate the behaviour of various deflector designs. The purpose of these simulations is to determine which design is most suitable for a particular scenario. Of particular interest is the trade-off between steerability, the outgoing -3dB beam width of the deflector and the size of the deflector. The simulations requires the following fixed parameters:

- The source beam directivity ($D_{beam}(\theta_{beam})$);
- The source steering efficiency ($\eta_{steer}(\alpha)$);
- The element receive directivity ($D_{element,receive}(\theta_{element})$);
- The element emit directivity ($D_{element,emit}(\theta_{element})$;
- The minimum power transfer efficiency that is still considered acceptable ($\eta_{T,min}$);
- The deflector tilt angle (β);
- The deflector element size ($W_{element}$).

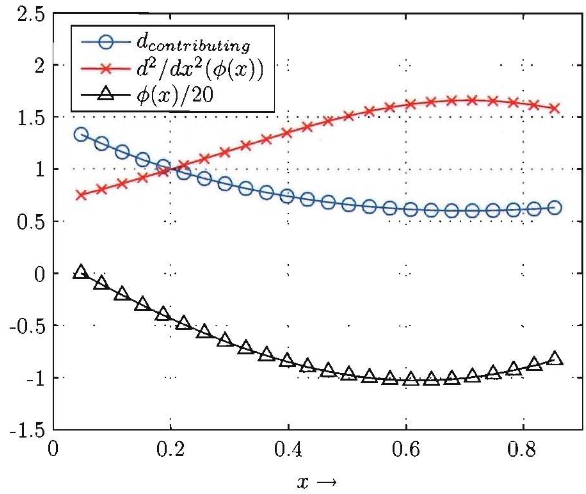

Figure 2.8: Normalised distance over which contributing elements are located (○); 2^{nd} derivative of phase-position curve [rad/m^2] (×); scaled phase-position curve [rad] (△)

The input for a simulation consists of the desired steerability ($\Delta\gamma$) and the target deflector size ($W_{deflector}$). These quantities taken into account, a suitable phase-position curve is determined, using the method described in the previous section. The simulator then calculates the resulting outgoing beams for various source steering angles. The element emit efficiency is also taken into account.

The simulation result consists of the average outgoing -3dB beam width ($BW_{-3dB,out}$), together with the actual steerability ($\Delta\gamma_{out}$) and is related to the deflector size ($W_{deflector}$). The actual steerability is defined as the difference between the angles of the outgoing beams, when steered towards x_l and x_h, respectively. The results of multiple simulations with varying input arguments are collected, to yield the relation between $BW_{-3dB,out}$, $\Delta\gamma_{out}$ and $W_{deflector}$.

2.6 Scenario dependent deflector design

The relation between $BW_{-3dB,out}$, $\Delta\gamma_{out}$ and $W_{deflector}$ is used to choose a deflector design for both scenarios 1 and 2, which are described in Section 2.3.1. The parameters for the simulations are chosen as follows:

- The source beam directivity $D_{beam}(\theta_{beam})$ is that of a 16dBi horn antenna, for the purpose of illustration. It is obtained from a full-wave simulation;
- The source steering efficiency $\eta_{steer}(\alpha) = \cos(\alpha)$. The steering efficiency is thus equal to 0.5 for $\alpha = \pm 60°$;
- The element receive directivity is equal to the element emit directivity: $D_{element,receive}(\theta_{element}) = D_{element,emit}(\theta_{element}) = \cos^2(\theta_{element})$;
- The minimum power transfer efficiency that is still considered acceptable $\eta_{T,min} = 0.5$;
- The deflector tilt angle $\beta = 45°$;
- The deflector element size $W_{element} = 0.5\lambda$.

The trade-off between deflector size ($W_{deflector}$), steerability ($\Delta\gamma_{out}$) and outgoing beam width ($BW_{-3dB,out}$) is visualised in Fig. 2.9. Suppose scenario 1 requires a steerability of 15^o and

scenario 2 a steerability of 50^o, both around $\theta = 90^o$. This means that for scenario 1, $\gamma_l = 82.5^o$ and $\gamma_h = 97.5^o$, and for scenario 2, $\gamma_l = 65^o$ and $\gamma_h = 115^o$. Fig. 2.10 shows the remaining trade-off between $BW_{-3dB,out}$ and $W_{deflector}$ for both scenarios. If we choose $W_{deflector} = 20\lambda$, we obtain $BW_{-3dB,out} = 11.5^\circ$ for scenario 1 and $BW_{-3dB,out} = 13.5^\circ$ for scenario 2. Fig. 2.11 and Fig. 2.12 show the resulting radiation patterns for both scenarios.
Because the deflector element emit directivity is non-uniform over the angular domain, the relative output power is lower for large angles and the resulting outgoing steering angles differ slightly from the design goals γ_l and γ_h. It is clear that the larger steerability of scenario 2 comes at a cost of a broader outgoing beam, compared to scenario 1.

2.7 Conclusion

The design of the deflector has been introduced. It has been explained that the deflector changes the phase distribution of the incident wave on the downside into a different phase distribution on the upside, which determines the deflecting behaviour. The change in phase distribution is performed by multiple phase-shifting deflector elements. It has also been explained that a trade-off exists between directivity and steerability and this has been expressed by defining two scenarios. The parameters of the deflector have been introduced and the behaviour of the deflector together with a source has been modelled. This behaviour is simulated and simulation results have been given for deflector designs that are suitable for the two scenarios.

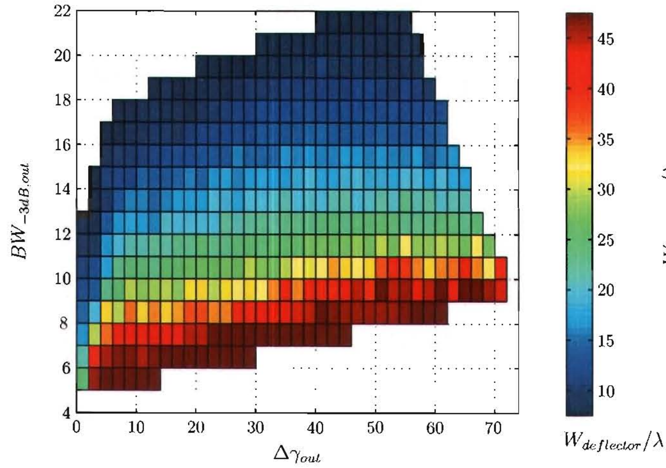

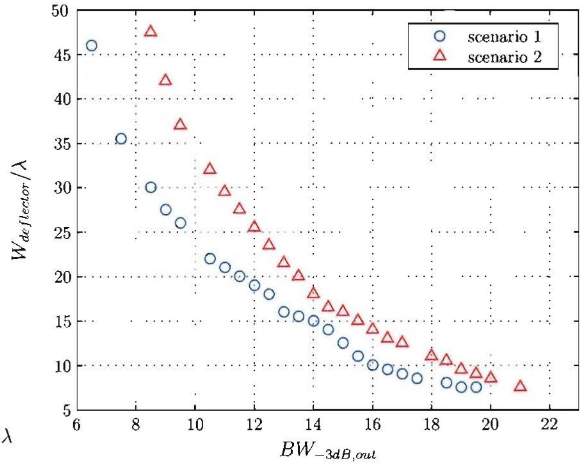

Figure 2.9: Trade-off between deflector size ($W_{deflector}$), steerability ($\Delta\gamma_{out}$) and outgoing beam width ($BW_{-3dB,out}$); colour indicates deflector size

Figure 2.10: Trade-off between deflector size ($W_{deflector}$) and outgoing beam width ($BW_{-3dB,out}$); scenario 1 (blue) and scenario 2 (red)

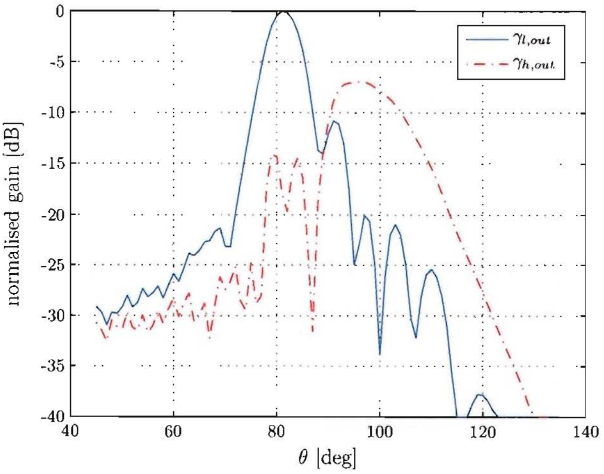

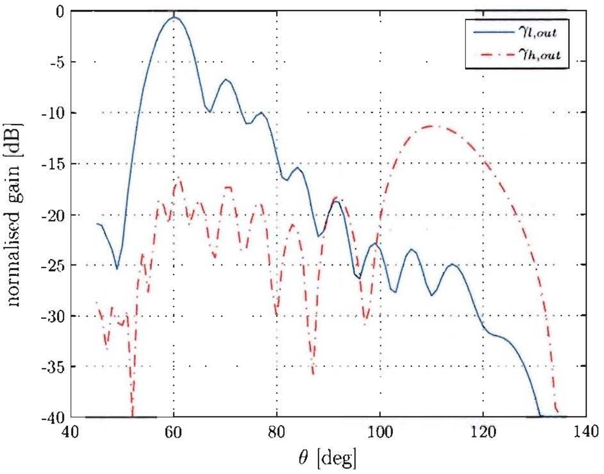

Figure 2.11: Radiation pattern of outer steering angles for scenario 1; $\gamma_{l,out} = 82°$ $(-)$ and $\gamma_{l,out} = 97°$ $(- \cdot)$

Figure 2.12: Radiation pattern of outer steering angles for scenario 2; $\gamma_{l,out} = 60°$ $(-)$ and $\gamma_{l,out} = 110°$ $(- \cdot)$

Chapter 3

Generic structures on a grounded dielectric slab

3.1 Introduction

To model a simplified alternative for the final deflector element, the modelling and analysis of generic planar structures on top of a grounded dielectric slab is considered. This is done in a number of steps. In Section 3.2, the field solution of a system containing only isotropic, homogeneous, linear, time-invariant materials is given. The vector potential and Green's function are introduced. In Section 3.3, the field solution of the grounded dielectric slab is given, using the Green's function, found by applying the proper boundary conditions. In Section 3.4, a generic structure on top of the slab is modelled, using the Method of Moments (MoM) [22]. In Section 3.5, a microstrip dipole antenna is given as an example.

3.2 General field solution

The general field solution is derived in a number of steps. First, Maxwell's equation with the accompanying constitutive relations are introduced in the time and the frequency domain. Then the fields are written in terms of a vector potential, which is related to the source current distribution through a Green's function. After this, the Helmholtz equation for the vector potential is given, which can be solved by applying the proper boundary conditions.

3.2.1 Maxwell's equations and constitutive relations

Maxwell's equations in the time domain are given by [44]

$$\begin{aligned}
\nabla \times \vec{E}(\vec{r},t) &= -\frac{\partial}{\partial t}\vec{B}(\vec{r},t) - \vec{J}_m(\vec{r},t), \\
\nabla \times \vec{H}(\vec{r},t) &= \frac{\partial}{\partial t}\vec{D}(\vec{r},t) + \vec{J}(\vec{r},t), \\
\nabla \cdot \vec{D}(\vec{r},t) &= \rho(\vec{r},t), \\
\nabla \cdot \vec{B}(\vec{r},t) &= \rho_m(\vec{r},t). \qquad (3.1)
\end{aligned}$$

The accompanying continuity equations are

$$\begin{aligned}
\nabla \cdot \vec{J}(\vec{r},t) + \frac{\partial}{\partial t}\rho(\vec{r},t) &= 0, \\
\nabla \cdot \vec{J}_m(\vec{r},t) + \frac{\partial}{\partial t}\rho_m(\vec{r},t) &= 0, \qquad (3.2)
\end{aligned}$$

where $\vec{E}$ is the *electric field*, $\vec{H}$ the *magnetic field*, $\vec{D}$ the *electric flux density*, $\vec{B}$ the *magnetic flux density*, $\vec{J}$ the *electric current distribution*, $\vec{J}_m$ the *magnetic current distribution*, ρ the *electric charge density* and ρ_m the *magnetic charge density*.

In the present analysis, we assume that there is no magnetic current or charge in the system. In App. E, the analysis is performed for the case of no electric current or charge present in the system. In general, functional relations exist between each of ($\vec{D}$, $\vec{B}$ and $\vec{J}$) and ($\vec{E}$, $\vec{H}$). The kind of relation depends on the material. We assume the materials to be isotropic, which means that (1) $\vec{D}$, $\vec{B}$ and $\vec{J}$ are aligned with the fields they depend on and (2) that $\vec{D}$ and $\vec{J}$ are only a function of $\vec{E}$ and $\vec{B}$ only a function of $\vec{H}$. We also assume the materials to be linear, time-invariant and homogeneous, which means that the relations reduce to a simple proportionality, i.e.

$$\begin{aligned}\vec{D}(\vec{r}) &= \varepsilon\vec{E}(\vec{r}),\\ \vec{B}(\vec{r}) &= \mu\vec{H}(\vec{r}),\\ \vec{J}(\vec{r}) &= \sigma\vec{E}(\vec{r}),\end{aligned} \tag{3.3}$$

where ε is called the *permittivity*, μ the *permeability* and σ the *conductivity* of the medium. The relations (3.3) are called the *constitutive relations*.

If we assume only time-harmonic solutions (which means $e^{j\omega t}$-dependency of the quantities in Eq. (3.1)) and take into account the assumptions above and the constitutive relations (Eq. (3.3)), Eq. (3.1) can be written in the frequency domain as

$$\begin{aligned}\nabla\times\vec{E}(\vec{r}) &= -j\omega\mu\vec{H}(\vec{r}),\\ \nabla\times\vec{H}(\vec{r}) &= j\omega\varepsilon\vec{E}(\vec{r})+\vec{J}(\vec{r}),\\ \nabla\cdot\vec{E}(\vec{r}) &= \rho(\vec{r})/\varepsilon,\\ \nabla\cdot\vec{H}(\vec{r}) &= 0.\end{aligned} \tag{3.4}$$

Together with the continuity equation

$$\nabla\cdot\vec{J}(\vec{r})+j\omega\rho(\vec{r}) = 0. \tag{3.5}$$

3.2.2 Vector potential and Green's function

For most problems, including a generic structure on the grounded dielectric slab, it is not possible to obtain closed-form solutions of Maxwell's equations in the spectral domain (Eq. (3.4)). To facilitate in this problem, the Green's function is introduced. A Green's function is the response of some (field) quantity to a point source. Green's functions can relate directly to the electric or magnetic field, but we make use of the Green's function that relates to a vector potential, which we will introduce shortly. Once this vector potential is known, the actual fields can obtained through a linear relation.

Because the magnetic field has zero divergence, it can be written as a curl of another vector $\vec{A}$, the *magnetic vector potential*, as

$$\vec{H}(\vec{r}) = \nabla\times\vec{A}(\vec{r}). \tag{3.6}$$

Substituting this relation in the first equation of (3.4) yields

$$\nabla\times(\vec{E}(\vec{r})+j\omega\mu\vec{A}(\vec{r})) = 0. \tag{3.7}$$

Therefore, $\vec{E}$ can be written as

$$\vec{E} = -\nabla V - j\omega\mu\vec{A}. \tag{3.8}$$

where V is a *scalar potential*. To make sure the scalar and vector potential are uniquely determined by the charge and current distribution in the system, we relate them through the *Lorenz* gauge [21]

$$\nabla\cdot\vec{A} = -j\omega\varepsilon^c V. \tag{3.9}$$

where $\varepsilon^c = \varepsilon + \frac{\sigma}{j\omega}$ is called the *complex permittivity*. The choice of the Lorenz gauge will be clear shortly. If Eq. (3.9) is substituted into Eq. (3.8) we obtain an expression which relates the fields to the vector potential only. Together with Eq. (3.6), the field solution can be written as a function of the magnetic vector potential only, as

$$\begin{aligned} \vec{H}(\vec{r}) &= \nabla \times \vec{A}(\vec{r}), \\ \vec{E}(\vec{r}) &= \frac{-j\omega\mu}{k^2}\left[k^2 + \nabla\nabla\cdot\right]\vec{A}, \end{aligned} \tag{3.10}$$

where $k = \omega\sqrt{\varepsilon^c\mu}$ is called the *propagation constant*.
In vacuum, this evaluates to

$$k = k_0 = \omega\sqrt{\varepsilon_0\mu_0} = \frac{2\pi f}{c} = \frac{2\pi}{\lambda_0}. \tag{3.11}$$

with $\omega = 2\pi f$, $c = 1/\sqrt{\varepsilon_0\mu_0}$ and $\lambda_0 = c/f$, where f is the frequency.
To find a solution for $\vec{A}$, a Green's function is defined which relates $\vec{A}$ to a unit current source. The total vector magnetic potential $\vec{A}$ due to an arbitrary current distribution $\vec{J}(\vec{r}_0)$ is found by the superposition integral

$$\vec{A}(\vec{r}) = \int_{V_0} \bar{\bar{G}}(\vec{r},\vec{r}_0)\cdot\vec{J}(\vec{r}_0)\, dV_0, \tag{3.12}$$

where V_0 contains the source currents. The dyadic Green's function is a 3x3 matrix of the form

$$\bar{\bar{G}}(\vec{r},\vec{r}_0) = \begin{pmatrix} G_{xx} & G_{xy} & G_{xz} \\ G_{yx} & G_{yy} & G_{yz} \\ G_{zx} & G_{zy} & G_{zz} \end{pmatrix}. \tag{3.13}$$

Combining Eq. (3.10) and (3.12), the electric field $\vec{E}$ can be written as a function of the source current distribution $\vec{J}$ as

$$\vec{E}(\vec{r}) = -\frac{j\omega\mu}{k^2}(k^2 + \nabla\nabla\cdot)\int_{V_0} \bar{\bar{G}}(\vec{r},\vec{r_0})\cdot\vec{J}(\vec{r_0})\, dV_0. \tag{3.14}$$

3.2.3 Helmholtz equation and boundary conditions

To obtain a solution for $\vec{A}$, we write the second equation of (3.4), using Eq. (3.6), (3.8) and the Lorenz gauge (3.9), as

$$\begin{aligned} \nabla \times \vec{H} &= j\omega\varepsilon\vec{E} + \vec{J}, \\ \nabla \times (\nabla \times \vec{A}) &= j\omega\varepsilon^c\vec{E} + \vec{J^p}, \\ \nabla(\nabla\cdot\vec{A}) - \nabla^2\vec{A} &= j\omega\varepsilon^c(-\nabla V - j\omega\mu\vec{A}) + \vec{J^p}, \\ -j\omega\varepsilon^c\nabla V - \nabla^2\vec{A} &= -j\omega\varepsilon^c\nabla V + \omega^2\varepsilon^c\mu\vec{A} + \vec{J^p}, \\ -\nabla^2\vec{A} - \omega^2\varepsilon^c\mu\vec{A} &= \vec{J^p}, \end{aligned} \tag{3.15}$$

where $\vec{J} = \sigma\vec{E} + \vec{J^p}$ and $\varepsilon^c = \varepsilon + \frac{\sigma}{j\omega}$ was used. $\vec{J^p}$ is called the *primary* or *source current*. From this point on, we will omit the superscripts p in $\vec{J^p}$ and c in ε^c. This results in the well-known Helmholtz equation for the vector potential, which is

$$\nabla^2\vec{A} + \omega^2\varepsilon\mu\vec{A} = -\vec{J}. \tag{3.16}$$

The solution to this equation must satisfy the proper boundary conditions, which depend on the configuration.

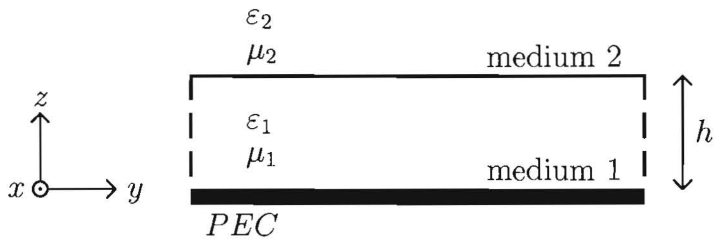

Figure 3.1: Configuration of the grounded dielectric slab

3.3 Field solution of the grounded dielectric slab

A comprehensive treatment of wave propagation, radiation and scattering in inhomogeneous media is provided in [11]. Wave propagation in stratified media is also covered in [53]. The field solution of the grounded dielectric slab can be obtained, for example, by using methods described in [31, 30, 52], but here, we follow the method as described in [46]. The field solution of the grounded dielectric slab is obtained by applying the boundary conditions, inherent to the configuration of the grounded dielectric slab, to the general field solution. This configuration is introduced in the first section. Next, expressions for the vector potential and Green's function are given explicitly for the case of surface currents on top of the slab. The Helmholtz equations and boundary conditions are transformed into the spectral domain, where a closed-form solution of the Green's function is obtained. The field solution is written in terms of this closed-form solution of the Green's function and the source current distribution. An expression for the electric far field is given. After this, a numerical approach is presented to obtain the field solution in the spatial domain. Finally, an example is given.

3.3.1 Configuration

We will examine the fields produced by a unit electric current point source on top of a grounded dielectric slab. Fig. 3.1 shows the configuration. The slab has height h and is infinite in size in the transverse (x and y) direction. The bottom of the slab is made of a perfect electric conducting (PEC) material. The slab itself is denoted as medium 1 and the material above the slab, which is air in general, is denoted as medium 2. The complex permittivity is denoted as $\varepsilon_i = \varepsilon_0 \varepsilon_{ri}$ and the permittivity is denoted as $\mu_i = \mu_0 \mu_{ri}$, where i is the number of the medium. It is assumed that in every medium $\mu_i = \mu_0$.
The boundary conditions for this configuration result in

$$\begin{aligned} \vec{u}_z \times \vec{E}_1 &= \vec{0} && z = 0, \\ \left.\begin{aligned} \vec{u}_z \times \vec{E}_1 &= \vec{u}_z \times \vec{E}_2 \\ \vec{u}_z \times \vec{H}_1 - \vec{u}_z \times \vec{H}_2 &= -\vec{J}_s \end{aligned}\right\} && z = h. \end{aligned} \tag{3.17}$$

We assume that the current only exists at $z = h$, so that we can write the current distribution as

$$\vec{J}(\vec{r}) = \vec{J}_s(x, y)\delta(z - h). \tag{3.18}$$

Further on, we will use the notation

$$\vec{\Upsilon}(x, y) = \vec{J}_s(x, y). \tag{3.19}$$

3.3.2 Vector potential and Green's function

We will consider a point source in the x or y-direction only. For a point source in the i-direction, where $i = x$ or $i = y$, at position $\vec{r}_s$, i.e.

$$\vec{J}(\vec{r}) = \vec{u}_i \delta(\vec{r} - \vec{r}_s), \tag{3.20}$$

the magnetic vector potential (Eq. (3.12)) becomes

$$\begin{aligned} \vec{A}(\vec{r}) &= \int_{V_0} \bar{\bar{G}}(\vec{r}, \vec{r}_0) \vec{u}_i \delta(\vec{r}_0 - \vec{r}_s)\, dV_0 \\ &= \bar{\bar{G}}(\vec{r}, \vec{r}_s) \vec{u}_i \\ &= G_{xi}(\vec{r}, \vec{r}_s) \vec{u}_x + G_{yi}(\vec{r}, \vec{r}_s) \vec{u}_y + G_{zi}(\vec{r}, \vec{r}_s) \vec{u}_z. \end{aligned} \tag{3.21}$$

In a layered medium, like a grounded dielectric slab, 2 components of the magnetic vector potential are needed to describe the fields. It is convenient to choose one component in the same direction as the source, and the other component directed orthogonal to the source. Because we are interested in an x or y-directed point source, it is convenient to choose G_{zi} as the second component. This has been shown by Sommerfeld [48]. Therefore, for an x-directed point source we have

$$\vec{A}(\vec{r}) = G_{xx}(\vec{r}, \vec{r}_s) \vec{u}_x + G_{zx}(\vec{r}, \vec{r}_s) \vec{u}_z, \tag{3.22}$$

and for a y-directed point source we have

$$\vec{A}(\vec{r}) = G_{yy}(\vec{r}, \vec{r}_s) \vec{u}_y + G_{zy}(\vec{r}, \vec{r}_s) \vec{u}_z. \tag{3.23}$$

We continue the analysis for an x-directed point source. The results can easily be transferred to the case of a y-directed point source. The fields, resulting from an x-directed point source are found by combining Eq. (3.10) and (3.22), for each homogeneous layer separately. This results in

$$\vec{H} = \begin{pmatrix} \partial_y A_z - \partial_z A_y \\ \partial_z A_x - \partial_x A_z \\ \partial_x A_y - \partial_y A_x \end{pmatrix} = \begin{pmatrix} \partial_y G_{zx} \\ \partial_z G_{xx} - \partial_x G_{zx} \\ -\partial_y G_{xx} \end{pmatrix}, \tag{3.24}$$

$$\begin{aligned} \vec{E} &= \frac{-j\omega\mu}{k^2} \begin{pmatrix} (k^2 + \partial_x^2) A_x + \partial_x \partial_y A_y + \partial_x \partial_z A_z \\ (k^2 + \partial_y^2) A_y + \partial_x \partial_y A_x + \partial_y \partial_z A_z \\ (k^2 + \partial_z^2) A_z + \partial_x \partial_z A_x + \partial_y \partial_z A_y \end{pmatrix} \\ &= \frac{-j\omega\mu}{k^2} \begin{pmatrix} (k^2 + \partial_x^2) G_{xx} + \partial_x \partial_z G_{zx} \\ \partial_x \partial_y G_{xx} + \partial_y \partial_z G_{zx} \\ (k^2 + \partial_z^2) G_{zx} + \partial_x \partial_z G_{xx} \end{pmatrix}. \end{aligned} \tag{3.25}$$

3.3.3 Helmholtz equation and boundary conditions

Combining Eq. (3.16), Eq. (3.18) and (3.22) results in Helmholtz equations for the non zero components of the dyadic Green's function:

$$\begin{aligned} \nabla^2 G_{xx}(\vec{r}, \vec{r}_s) + \varepsilon_r k_0^2 G_{xx}(\vec{r}, \vec{r}_s) &= -J_x(\vec{r}), \\ \nabla^2 G_{zx}(\vec{r}, \vec{r}_s) + \varepsilon_r k_0^2 G_{zx}(\vec{r}, \vec{r}_s) &= 0, \end{aligned} \tag{3.26}$$

where $k_0 = \omega\sqrt{\varepsilon_0 \mu_0}$ and

$$J_x(\vec{r}) = \delta(\vec{r} - \vec{r}_s) = \delta(x - x_s)\delta(y - y_s)\delta(z - h). \tag{3.27}$$

To solve this set of differential equations, we will consider them in both media separately, and apply the proper boundary conditions. In medium 1, we have

$$\begin{aligned} \nabla^2 G_{1xx}(\vec{r}, \vec{r}_s) + \varepsilon_{r1} k_0^2 G_{1xx}(\vec{r}, \vec{r}_s) &= 0, \\ \nabla^2 G_{1zx}(\vec{r}, \vec{r}_s) + \varepsilon_{r1} k_0^2 G_{1zx}(\vec{r}, \vec{r}_s) &= 0, \end{aligned} \tag{3.28}$$

and in medium 2 we have

$$\begin{aligned} \nabla^2 G_{2xx}(\vec{r},\vec{r}_s) + \varepsilon_{r2} k_0^2 G_{2xx}(\vec{r},\vec{r}_s) &= 0, \\ \nabla^2 G_{2zx}(\vec{r},\vec{r}_s) + \varepsilon_{r2} k_0^2 G_{2zx}(\vec{r},\vec{r}_s) &= 0. \end{aligned} \tag{3.29}$$

The boundary conditions from Eq. (3.17) result in (using Eq. (3.24) and (3.25)):

$$\begin{aligned} &\left.\begin{aligned} G_{1xx} &= 0 \\ \partial_x G_{1xx} + \partial_z G_{1zx} &= 0 \end{aligned}\right\} \quad z = 0, \\ &\left.\begin{aligned} G_{1xx} &= G_{2xx} \\ \varepsilon_{r2}\left[\partial_x^2 G_{1xx} + \partial_x \partial_z G_{1zx}\right] &= \varepsilon_{r1}\left[\partial_x^2 G_{2xx} + \partial_x \partial_z G_{2zx}\right] \\ \partial_y G_{1zx} &= \partial_y G_{2zx} \\ \partial_z G_{1xx} - \partial_z G_{2xx} &= \delta(x - x_s)\delta(y - y_s) \end{aligned}\right\} \quad z = h, \end{aligned} \tag{3.30}$$

where we have omitted the dependence on $(\vec{r},\vec{r}_s)$ for clarity.

3.3.4 Spectral domain description

In the spectral domain, an analytical expression of the dyadic Green's function can be obtained. We obtain the spectral-domain Green's function by applying the Fourier transform ($\mathcal{F}_{xy}\{\cdot\}$) with respect to the transverse coordinates (App. A) of the spatial-domain form Green's function. This results in

$$\hat{G}(k_x, k_y, z, \vec{r}_s) = \mathcal{F}_{xy}\left\{G(x, y, z, \vec{r}_s)\right\} = \int_{-\infty}^{\infty}\int_{-\infty}^{\infty} G(x, y, z, \vec{r}_s) e^{j(k_x x + k_y y)} dx dy. \tag{3.31}$$

Once we have a solution in the spectral domain, the original spatial-domain Green's function can by obtained by applying the inverse Fourier transform ($\mathcal{F}^{-1}_{k_x k_y}\{\cdot\}$) of the spectral domain form. This results in

$$G(x, y, z, \vec{r}_s) = \mathcal{F}^{-1}_{k_x k_y}\left\{\hat{G}(k_x, k_y, z, \vec{r}_s)\right\} = \frac{1}{4\pi^2}\int_{-\infty}^{\infty}\int_{-\infty}^{\infty} \hat{G}(k_x, k_y, z, \vec{r}_s) e^{-j(k_x x + k_y y)} dk_x dk_y. \tag{3.32}$$

The spectral-domain form of Helmholtz equations (Eq. (3.28) and (3.29)) becomes

$$\begin{aligned} &\left.\begin{aligned} \partial_z^2 \hat{G}_{1xx}(k_x, k_y, z, \vec{r}_s) + k_{z1}^2 \hat{G}_{1xx}(k_x, k_y, z, \vec{r}_s) &= 0 \\ \partial_z^2 \hat{G}_{1zx}(k_x, k_y, z, \vec{r}_s) + k_{z1}^2 \hat{G}_{1zx}(k_x, k_y, z, \vec{r}_s) &= 0 \end{aligned}\right\} \quad 0 < z < h, \\ &\left.\begin{aligned} \partial_z^2 \hat{G}_{2xx}(k_x, k_y, z, \vec{r}_s) + k_{z2}^2 \hat{G}_{2xx}(k_x, k_y, z, \vec{r}_s) &= 0 \\ \partial_z^2 \hat{G}_{2zx}(k_x, k_y, z, \vec{r}_s) + k_{z2}^2 \hat{G}_{2zx}(k_x, k_y, z, \vec{r}_s) &= 0 \end{aligned}\right\} \quad h < z < \infty, \end{aligned} \tag{3.33}$$

in which the z-components of the wave vector in each region are given by

$$\begin{aligned} k_{z1} &= \sqrt{\varepsilon_{r1} k_o^2 - k_x^2 - k_y^2} \qquad (\mathrm{Im}(k_{z1}) < 0 \text{ or } \mathrm{Im}(k_{z1}) = 0 \wedge \mathrm{Re}(k_{z1}) > 0), \\ k_{z2} &= \sqrt{\varepsilon_{r2} k_o^2 - k_x^2 - k_y^2} \qquad (\mathrm{Im}(k_{z2}) < 0 \text{ or } \mathrm{Im}(k_{z2}) = 0 \wedge \mathrm{Re}(k_{z2}) > 0). \end{aligned}$$

The boundary conditions in Eq. (3.30) are transformed to the spectral domain, resulting in

$$\begin{array}{l}\left.\begin{aligned} \hat{G}_{1xx} &= 0 \\ \partial_z \hat{G}_{1zx} &= 0 \end{aligned}\right\} \quad z = 0, \\ \left.\begin{aligned} \hat{G}_{1xx} &= \hat{G}_{2xx} \\ \varepsilon_{r2}\left[k_x^2 \hat{G}_{1xx} + jk_x \partial_z \hat{G}_{1zx}\right] &= \varepsilon_{r1}\left[k_x^2 \hat{G}_{2xx} + jk_x \partial_z \hat{G}_{2zx}\right] \\ \hat{G}_{1zx} &= \hat{G}_{2zx} \\ \partial_z \hat{G}_{1xx} - \partial_z \hat{G}_{2xx} &= e^{jk_x x_s} e^{jk_y y_s} \end{aligned}\right\} \quad z = h, \end{array} \tag{3.34}$$

where we have omitted the dependence on $(k_x, k_y, z, \vec{r}_s)$ for clarity.

3.3.5 Solution

Spectral-domain Green's function

The components of the spectral-domain Green's function all satisfy a homogenous Helmholtz equation. The general solution can be written as

$$\begin{aligned} \hat{G}_{1xx} &= C_{1xx} e^{-jk_{z1} z} + D_{1xx} e^{-jk_{z1}(h-z)}, \\ \hat{G}_{1zx} &= C_{1zx} e^{-jk_{z1} z} + D_{1zx} e^{-jk_{z1}(h-z)}, \\ \hat{G}_{2xx} &= C_{2xx} e^{-jk_{z2}(z-h)}, \\ \hat{G}_{2zx} &= C_{2zx} e^{-jk_{z2}(z-h)}. \end{aligned} \tag{3.35}$$

The unknown constants can be determined by applying boundary conditions (Eq. (3.34)). By solving this set of linear equations analytically, we obtain, for the unknown coefficients in Eq. (3.35)

$$\begin{aligned} C_{1xx} &= -1/D \cdot e^{jk_x x_s} e^{jk_y y_s}, \\ D_{1xx} &= e^{jk_{z1} h}/D \cdot e^{jk_x x_s} e^{jk_y y_s}, \\ C_{1zx} &= N/D \cdot e^{jk_x x_s} e^{jk_y y_s}, \\ D_{1zx} &= e^{jk_{z1} h} \cdot N/D \cdot e^{jk_x x_s} e^{jk_y y_s}, \\ C_{2xx} &= 2j \sin(k_{z1} h)/D \cdot e^{jk_x x_s} e^{jk_y y_s}, \\ C_{2zx} &= 2\cos(k_{z1} h) \cdot N/D \cdot e^{jk_x x_s} e^{jk_y y_s}, \end{aligned} \tag{3.36}$$

where

$$\begin{aligned} D &= 2jk_{z1}\cos(k_{z1}h) - 2k_{z2}\sin(k_{z1}h) = 2jT_e, \\ N &= \frac{(\varepsilon_{r2} - \varepsilon_{r1})k_x j \sin(k_{z1}h)}{\varepsilon_{r1} k_{z2} \cos(k_{z1}h) + j\varepsilon_{r2} k_{z1} \sin(k_{z1}h)} = \frac{(\varepsilon_{r2} - \varepsilon_{r1})k_x j \sin(k_{z1}h)}{T_m}, \end{aligned} \tag{3.37}$$

with

$$\begin{aligned} T_e &= k_{z1}\cos(k_{z1}h) + jk_{z2}\sin(k_{z1}h), \\ T_m &= \varepsilon_{r1} k_{z2} \cos(k_{z1}h) + j\varepsilon_{r2} k_{z1} \sin(k_{z1}h). \end{aligned} \tag{3.38}$$

The zeros of the T_e and T_m expressions can create TE and TM poles, respectively, in the Green's function and these can be interpreted as possible excitation of TE or TM surface wave modes [12].

Now Eq. (3.35) becomes

$$\begin{aligned}
\hat{G}_{1xx}(k_x, k_y, z, \vec{r}_s) &= \frac{\sin(k_{z1}z)}{T_e} e^{jk_x x_s} e^{jk_y y_s}, \\
\hat{G}_{1zx}(k_x, k_y, z, \vec{r}_s) &= \frac{k_x(\varepsilon_{r2} - \varepsilon_{r1}) \cos(k_{z1}z) \sin(k_{z1}h)}{T_e T_m} e^{jk_x x_s} e^{jk_y y_s}, \\
\hat{G}_{2xx}(k_x, k_y, z, \vec{r}_s) &= \frac{\sin(k_{z1}h) e^{jk_{z2}(h-z)}}{T_e} e^{jk_x x_s} e^{jk_y y_s}, \\
\hat{G}_{2zx}(k_x, k_y, z, \vec{r}_s) &= \frac{k_x(\varepsilon_{r2} - \varepsilon_{r1}) \cos(k_{z1}h) \sin(k_{z1}h) e^{jk_{z2}(h-z)}}{T_e T_m} e^{jk_x x_s} e^{jk_y y_s}. \qquad (3.39)
\end{aligned}$$

Electric field in the spectral domain

With the Green's function available in the spectral domain, we can write the solution of $\vec{E}(\vec{r})$ (Eq. (3.14)) in terms of the inverse Fourier transform of the spectral-domain Green's function as

$$\begin{aligned}
\vec{E}(\vec{r}) &= -\frac{j\omega\mu}{k^2}(k^2 + \nabla\nabla\cdot) \int_{V_0} \bar{\bar{G}}(\vec{r}, \vec{r}_0) \cdot \vec{J}(\vec{r}_0)\; dV_0 \\
&= -\frac{j\omega\mu}{k^2} \int_{V_0} \left[\frac{1}{4\pi^2} \int_{k_x} \int_{k_y} (k^2 + \hat{\nabla}\hat{\nabla}\cdot) \hat{\bar{\bar{G}}}(k_x, k_y, z, \vec{r}_0) e^{-jk_x x} e^{-jk_y y} dk_x dk_y \right] \cdot \vec{J}(\vec{r}_0)\; dV_0, \\
&\qquad (3.40)
\end{aligned}$$

where the gradient ($\hat{\nabla}$) is defined as

$$\hat{\nabla} = \begin{pmatrix} -jk_x \\ -jk_y \\ \partial_z \end{pmatrix}. \qquad (3.41)$$

By observing Eq. (3.39), $\hat{\bar{\bar{G}}}$ can be separated according to

$$\hat{\bar{\bar{G}}}(k_x, k_y, z, \vec{r}_0) = \hat{\bar{\bar{\Gamma}}}(k_x, k_y, z, z_0) e^{jk_x x_0} e^{jk_y y_0}. \qquad (3.42)$$

If the source height is a constant, i.e. $z_0 = h$, like in the case of a structure on top of the slab, we can use this in Eq. (3.42) and omit the dependence on z_0 from this point on, so we can write

$$\hat{\bar{\bar{\Gamma}}}(k_x, k_y, z, z_0) = \hat{\bar{\bar{\Gamma}}}(k_x, k_y, z). \qquad (3.43)$$

Furthermore we introduce

$$\hat{\bar{\bar{Q}}}(k_x, k_y, z) = (k^2 + \hat{\nabla}\hat{\nabla}\cdot)\hat{\bar{\bar{\Gamma}}}(k_x, k_y, z). \qquad (3.44)$$

Now we can write the solution of $\vec{E}(\vec{r})$ (Eq. (3.40)) as an inverse Fourier transform of the spectral-domain representation ($\hat{\vec{E}}(k_x, k_y, z)$), as

$$\begin{aligned}
\vec{E}(\vec{r}) &= -\frac{j\omega\mu}{4\pi^2 k^2} \int_{V_0} \left[\int_{k_x} \int_{k_y} (k^2 + \hat{\nabla}\hat{\nabla}\cdot) \left[\hat{\bar{\bar{\Gamma}}}(k_x, k_y, z) e^{jk_x x_0} e^{jk_y y_0} \right] e^{-jk_x x} e^{-jk_y y} dk_x dk_y \right] \cdot \vec{J}(\vec{r}_0)\; dV_0 \\
&= -\frac{j\omega\mu}{4\pi^2 k^2} \int_{k_x} \int_{k_y} \hat{\bar{\bar{Q}}}(k_x, k_y, z) e^{-jk_x x} e^{-jk_y y} \left[\int_{V_0} \vec{J}(\vec{r}_0) e^{jk_x x_0} e^{jk_y y_0}\; dV_0 \right] dk_x dk_y \\
&= -\frac{j\omega\mu}{4\pi^2 k^2} \int_{k_x} \int_{k_y} \hat{\bar{\bar{Q}}}(k_x, k_y, z) e^{-jk_x x} e^{-jk_y y} \left[\int_{x_0} \int_{y_0} \vec{\Upsilon}(x_0, y_0) e^{jk_x x_0} e^{jk_y y_0}\; dx_0 dy_0 \right] dk_x dk_y \\
&= -\frac{j\omega\mu}{4\pi^2 k^2} \int_{k_x} \int_{k_y} \hat{\bar{\bar{Q}}}(k_x, k_y, z) \cdot \hat{\vec{\Upsilon}}(k_x, k_y) e^{-jk_x x} e^{-jk_y y} dk_x dk_y \\
&= \frac{1}{4\pi^2} \int_{k_x} \int_{k_y} \hat{\vec{E}}(k_x, k_y, z) e^{-jk_x x} e^{-jk_y y} dk_x dk_y, \qquad (3.45)
\end{aligned}$$

with

$$\hat{\vec{E}}(k_x, k_y, z) = -\frac{j\omega\mu}{k^2}\hat{\bar{\bar{Q}}}(k_x, k_y, z) \cdot \hat{\vec{\Upsilon}}(k_x, k_y). \tag{3.46}$$

The elements of $\hat{\bar{\bar{Q}}}$ evaluate to

$$\begin{aligned}
\hat{\bar{\bar{Q}}}(k_x, k_y, z) &= (k^2 + \hat{\nabla}\hat{\nabla}\cdot)\hat{\bar{\bar{\Gamma}}}(k_x, k_y, z) \\
&= (k^2 + \hat{\nabla}\hat{\nabla}\cdot)\begin{pmatrix} \hat{\gamma}_{xx} & 0 & 0 \\ 0 & \hat{\gamma}_{yy} & 0 \\ \hat{\gamma}_{zx} & \hat{\gamma}_{zy} & 0 \end{pmatrix} \\
&= \begin{pmatrix} (k^2 - k_x^2)\hat{\gamma}_{xx} - jk_x\partial_z\hat{\gamma}_{zx} & -k_xk_y\hat{\gamma}_{yy} - jk_x\partial_z\hat{\gamma}_{zy} & 0 \\ -k_xk_y\hat{\gamma}_{xx} - jk_y\partial_z\hat{\gamma}_{zx} & (k^2 - k_y^2)\hat{\gamma}_{yy} - jk_y\partial_z\hat{\gamma}_{zy} & 0 \\ -jk_x\partial_z\hat{\gamma}_{xx} + (k^2 - \partial_z^2)\hat{\gamma}_{zx} & -jk_y\partial_z\hat{\gamma}_{yy} + (k^2 - \partial_z^2)\hat{\gamma}_{zy} & 0 \end{pmatrix} \\
&= \begin{pmatrix} \hat{q}_{xx} & \hat{q}_{xy} & \hat{q}_{xz} \\ \hat{q}_{yx} & \hat{q}_{yy} & \hat{q}_{yz} \\ \hat{q}_{zx} & \hat{q}_{zy} & \hat{q}_{zz} \end{pmatrix},
\end{aligned} \tag{3.47}$$

where the divergence $(\nabla\cdot)$ of the dyadic $\bar{\bar{\Gamma}}$ is evaluated for each column vector separately. The third column, representing z-directed current density, contains only zeros, because we assumed x or y directed current only. The elements of $\hat{\bar{\bar{Q}}}$ that are needed to compute the transverse fields in medium 2, due to a transverse current distribution at $z = h$, are

$$\begin{aligned}
\hat{q}_{2xx}(k_x, k_y, z) &= (\varepsilon_{r2}k_0^2 - k_x^2)\hat{\gamma}_{2xx} - jk_x\partial_z\hat{\gamma}_{2zx} \\
&= (\varepsilon_{r2}k_0^2 - k_x^2)\frac{\sin(k_{z1}h)e^{jk_{z2}(h-z)}}{T_e} - jk_x\partial_z\frac{k_x(\varepsilon_{r2} - \varepsilon_{r1})\cos(k_{z1}h)\sin(k_{z1}h)e^{jk_{z2}(h-z)}}{T_eT_m} \\
&= \frac{\sin(k_{z1}h)e^{jk_{z2}(h-z)}}{T_eT_m} \cdot \left[(\varepsilon_{r2}k_0^2 - k_x^2)T_m - k_{z2}k_x^2(\varepsilon_{r2} - \varepsilon_{r1})\cos(k_{z1}h)\right] \\
&= \frac{\varepsilon_{r2}\sin(k_{z1}h)e^{jk_{z2}(h-z)}}{T_eT_m} \cdot \left[(\varepsilon_{r1}k_0^2 - k_x^2)k_{z2}\cos(k_{z1}h) + j(\varepsilon_{r2}k_0^2 - k_x^2)k_{z1}\sin(k_{z1}h)\right] \\
&= \frac{\varepsilon_{r2}\sin(k_{z1}h)e^{jk_{z2}(h-z)}}{T_eT_m} \cdot \left[k_0^2T_m - k_x^2\left(k_{z2}\cos(k_{z1}h) + jk_{z1}\sin(k_{z1}h)\right)\right],
\end{aligned} \tag{3.48}$$

$$\hat{q}_{2yy}(k_x, k_y, z) = \frac{\varepsilon_{r2}\sin(k_{z1}h)e^{jk_{z2}(h-z)}}{T_eT_m} \cdot \left[k_0^2T_m - k_y^2\left(k_{z2}\cos(k_{z1}h) + jk_{z1}\sin(k_{z1}h)\right)\right], \tag{3.49}$$

$$\begin{aligned}
&\hat{q}_{2xy}(k_x, k_y, z) = \\
&\hat{q}_{2yx}(k_x, k_y, z) = -k_xk_y\hat{\gamma}_{2xx} - jk_y\partial_z\hat{\gamma}_{2zx} \\
&\quad = -k_xk_y\frac{\sin(k_{z1}h)e^{jk_{z2}(h-z)}}{T_e} - jk_y\partial_z\frac{k_x(\varepsilon_{r2} - \varepsilon_{r1})\cos(k_{z1}h)\sin(k_{z1}h)e^{jk_{z2}(h-z)}}{T_eT_m} \\
&\quad = -\frac{k_xk_y\sin(k_{z1}h)e^{jk_{z2}(h-z)}}{T_eT_m} \cdot \left[T_m + k_{z2}(\varepsilon_{r2} - \varepsilon_{r1})\cos(k_{z1}h)\right] \\
&\quad = -\frac{\varepsilon_{r2}k_xk_y\sin(k_{z1}h)e^{jk_{z2}(h-z)}}{T_eT_m} \cdot \left[k_{z2}\cos(k_{z1}h) + jk_{z1}\sin(k_{z1}h)\right].
\end{aligned} \tag{3.50}$$

Electric far field

The electric far field can be obtained from the closed-form expression

$$\begin{aligned}
\vec{E}(r, \theta, \phi) &= \frac{jk_0e^{-jk_0r}}{2\pi r}e^{jk_0h\cos\theta} \cdot \vec{u}_r \times \left[\hat{\vec{E}}(k_x, k_y, h) \times \vec{u}_r\right] \\
&= \frac{jk_0e^{-jk_0r}}{2\pi r}e^{jk_0h\cos\theta}\left\{\vec{u}_\phi\left[\hat{E}_y(k_x, k_y, h)\cos\theta\cos\phi - \hat{E}_x(k_x, k_y, h)\cos\theta\sin\phi\right]\right. \\
&\quad \left. + \vec{u}_\theta\left[\hat{E}_y(k_x, k_y, h)\sin\phi - \hat{E}_x(k_x, k_y, h)\cos\phi\right]\right\},
\end{aligned} \tag{3.51}$$

where $k_x = k_0 \sin\theta \cos\phi$ and $k_y = k_0 \sin\theta \sin\phi$ is used. The electric field in the spectral domain is evaluated in the upper medium, at $z = h$. It is given by (Eq. (3.46))

$$\begin{aligned} \hat{\vec{E}}(k_x, k_y, h) &= \hat{\vec{E}}_2(k_x, k_y, h) \\ &= \frac{-j\omega\mu}{k_2^2} \cdot \hat{\bar{\bar{Q}}}_2(k_x, k_y, h) \cdot \hat{\vec{\Upsilon}}(k_x, k_y). \end{aligned} \tag{3.52}$$

3.3.6 Numerical approach

To obtain the field solution in the spatial domain, the inverse Fourier transform integral of the spectral domain representation (Eq. (3.45)) has to be evaluated. In general, an analytical expression can not be obtained, so the evaluation has to be performed numerically. To this end, we introduce a coordinate transformation according to

$$\begin{aligned} k_x &= k_\rho \cos\psi, \\ k_y &= k_\rho \sin\psi, \\ x &= r\cos\phi, \\ y &= r\sin\phi, \end{aligned} \tag{3.53}$$

and therefore

$$\begin{aligned} k_x x + k_y y &= k_\rho \cos\psi \cdot r\cos\phi + k_\rho \sin\psi \cdot r \sin\phi \\ &= k_\rho r \cos(\psi - \phi), \\ dk_x dk_y &= k_\rho d\psi dk_\rho, \end{aligned}$$

so that Eq. (3.45) becomes

$$\vec{E}(\vec{r}) = \frac{1}{4\pi^2} \int\limits_0^\infty \int\limits_{2\pi} \hat{\vec{E}}(k_\rho, \psi, z) e^{-jk_\rho r \cos(\psi - \phi)}\, k_\rho d\psi dk_\rho, \tag{3.54}$$

where the evaluation of the inner integral is performed over one period of length 2π. To evaluate the outer integral of Eq. (3.54) with a certain sufficient precision, an upper bound (K_ρ) can be chosen. Furthermore, to avoid integration through singularities present at certain values of k_ρ, complex contour deformation can be applied. It is assumed that only the field solution above the slab is of interest. It turns out that the convergence behaviour of Eq. (3.54) only depends on the frequency (f) and the observation height above the slab (z). For the real part of the electric field, integration over $0 \leq k_\rho \leq \varepsilon_1 k_0$ suffices, because the real part of the integrand of Eq. (3.54) is equal to 0 for $k_\rho > \varepsilon_1 k_0$. The imaginary part of the integrand is finite for $0 \leq k_\rho < \infty$. Fig. 3.2 shows the convergence behaviour of the imaginary part of the x-component of the electric field above the slab for different f and z and Fig. 3.3 shows the same for the y-component of the electric field. From these figures it can be concluded, that for a frequency of 60 GHz and above and an observation height of 0.2 mm and above, integration up to $40k_0$ suffices. Note that this value depends on the mesh size. If, for example, the mesh size is decreased by a factor k, the value of K_ρ should be increased by the same factor in order to obtain results with equivalent precision.

3.3.7 Example

As an example, we evaluate the electric field of an x-directed point source on top of the slab, situated at $(x_s, y_s) = (0, 0)$. Then the transverse current distribution in the spectral domain $\hat{\Upsilon}(k_x, k_y)$ is equal to

$$\hat{\Upsilon}(k_x, k_y) = 1 \cdot \vec{u}_x. \tag{3.55}$$

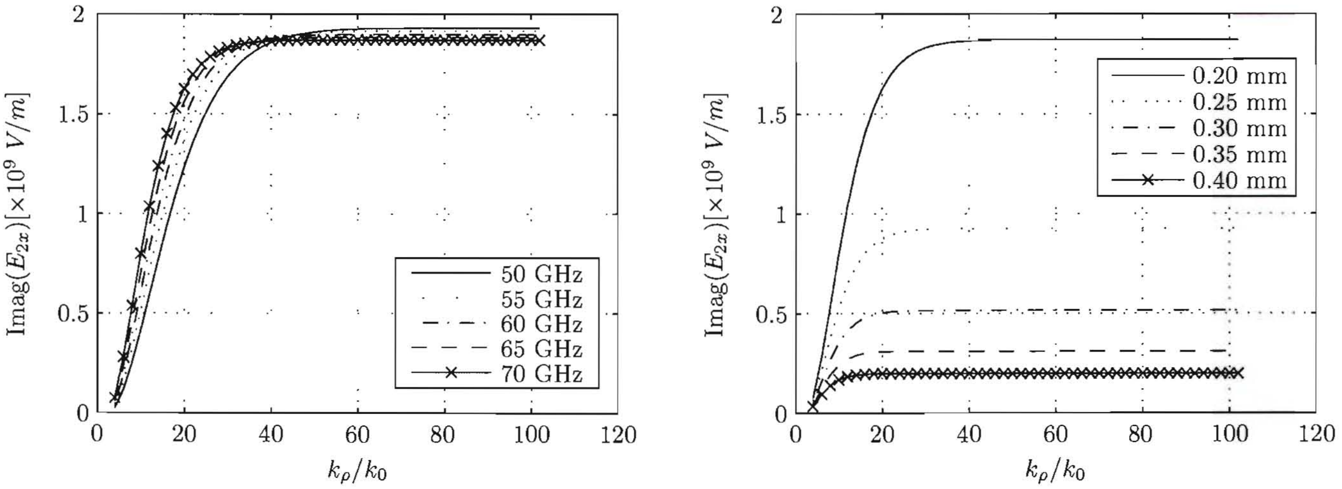

Figure 3.2: Evaluation of the imaginary part of E_{2x} as function of K_ρ; frequency (f) as parameter with $z = 0.2$ mm (left) and observation height above the slab (z) as parameter with $f = 60$ GHz (right)

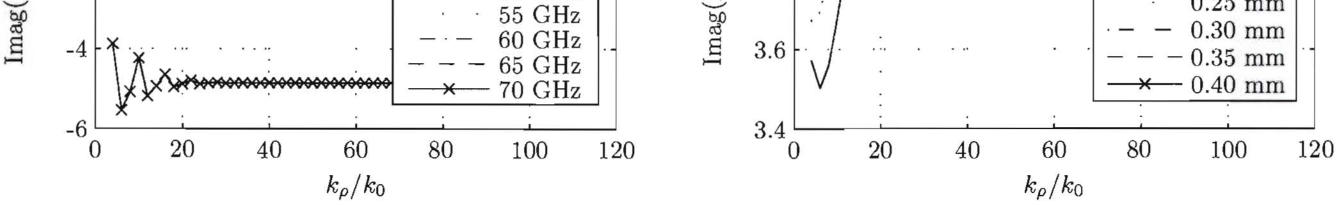

Figure 3.3: Evaluation of the imaginary part of E_{2y} as function of K_ρ; frequency (f) as parameter with $z = 0.2$ mm (left) and observation height above the slab (z) as parameter with $f = 60$ GHz (right)

Using this expression, the solution of $\vec{E}$ (Eq. (3.45)) in medium 2 becomes

$$\begin{aligned}\vec{E}_2(\vec{r}) &= -\frac{j\omega\mu}{4\pi^2k^2}\int_{k_x}\int_{k_y}\hat{\bar{\bar{Q}}}(k_x,k_y,z)\cdot\hat{\Upsilon}(k_x,k_y)e^{-jk_xx}e^{-jk_yy}dk_xdk_y\\ &= -\frac{j\omega\mu}{4\pi^2k^2}\int_{k_x}\int_{k_y}\left(\hat{q}_{2xx}u_x+\hat{q}_{2yx}u_y+\hat{q}_{2zx}u_z\right)e^{-jk_xx}e^{-jk_yy}dk_xdk_y. \qquad (3.56)\end{aligned}$$

Using Eq. (3.48) and (3.50) in the previous equation, E_{2x} and E_{2y} can be written as

$$\begin{aligned}E_{2x}(\vec{r}) &= -\frac{j\omega\mu}{4\pi^2k^2}\int_{k_x}\int_{k_y}\hat{q}_{2xx}e^{-jk_xx}e^{-jk_yy}dk_xdk_y\\ &= -\frac{j\omega\mu}{4\pi^2k_0^2}\int_{k_x}\int_{k_y}\frac{\sin(k_{z1}h)e^{jk_{z2}(h-z)}}{T_eT_m}\cdot\\ &\quad\left[k_0^2T_m-k_x^2\left(k_{z2}\cos(k_{z1}h)+jk_{z1}\sin(k_{z1}h)\right)\right]e^{-jk_xx}e^{-jk_yy}dk_xdk_y, \qquad (3.57)\end{aligned}$$

$$\begin{aligned}E_{2y}(\vec{r}) &= -\frac{j\omega\mu}{4\pi^2k^2}\int_{k_x}\int_{k_y}\hat{q}_{2xy}e^{-jk_xx}e^{-jk_yy}dk_xdk_y\\ &= \frac{j\omega\mu}{4\pi^2k_0^2}\int_{k_x}\int_{k_y}\frac{k_xk_y\sin(k_{z1}h)e^{jk_{z2}(h-z)}}{T_eT_m}\cdot\left[k_{z2}\cos(k_{z1}h)+jk_{z1}\sin(k_{z1}h)\right]e^{-jk_xx}e^{-jk_yy}dk_xdk_y.\end{aligned}$$

(3.58)

Using the coordinate transformation (Eq. (3.53)), Eq. (3.57) becomes

$$\begin{aligned}E_{2x}(r,\phi,z) &= \frac{-j\omega\mu_0}{4\pi^2k_0^2}\cdot\int_0^\infty\int_{2\pi}\frac{\sin(k_{z1}h)e^{jk_{z2}(h-z)}}{T_eT_m}\cdot\\ &\quad\left[k_0^2T_m-k_\rho^2\cos^2\psi\left(k_{z2}\cos(k_{z1}h)+jk_{z1}\sin(k_{z1}h)\right)\right]e^{-jk_\rho r\cos(\psi-\phi)}\,k_\rho d\psi dk_\rho\\ &= \frac{-j\omega\mu_0}{4\pi^2k_0^2}\cdot\int_0^\infty\frac{\sin(k_{z1}h)e^{jk_{z2}(h-z)}}{T_eT_m}\cdot\left(\left[\int_{2\pi}e^{-jk_\rho r\cos(\psi-\phi)}d\psi\right]\cdot k_0^2T_m-\right.\\ &\quad\left.\left[\int_{2\pi}e^{-jk_\rho r\cos(\psi-\phi)}\cos^2\psi d\psi\right]\cdot k_\rho^2\left[k_{z2}\cos(k_{z1}h)+jk_{z1}\sin(k_{z1}h)\right]\right)k_\rho dk_\rho\\ &= \frac{-j\omega\mu_0}{4\pi^2k_0^2}\cdot\int_0^\infty\frac{\sin(k_{z1}h)e^{jk_{z2}(h-z)}}{T_eT_m}\cdot\left(2\pi J_0(k_\rho r)\cdot k_0^2T_m-\right.\\ &\quad\left.\pi\left[J_0(k_\rho r)-J_2(k_\rho r)\cos(2\phi)\right]\cdot k_\rho^2\left[k_{z2}\cos(k_{z1}h)+jk_{z1}\sin(k_{z1}h)\right]\right)k_\rho dk_\rho, \qquad (3.59)\end{aligned}$$

and Eq. (3.58) becomes

$$\begin{aligned}E_{2y}(r,\phi,z) &= \frac{j\omega\mu_0}{4\pi^2k_0^2}\cdot\int_0^\infty\frac{\sin(k_{z1}h)e^{jk_{z2}(h-z)}}{T_eT_m}\cdot\int_{2\pi}\frac{1}{2}e^{-jk_\rho r\cos(\psi-\phi)}\sin(2\psi)d\psi\cdot\\ &\quad\left[k_{z2}\cos(k_{z1}h)+jk_{z1}\sin(k_{z1}h)\right]\,k_\rho^3dk_\rho\\ &= \frac{j\omega\mu_0}{4\pi^2k_0^2}\cdot\int_0^\infty\frac{\sin(k_{z1}h)e^{jk_{z2}(h-z)}}{T_eT_m}\cdot\pi J_2(k_\rho r)\sin(2\phi)\cdot\left[k_{z2}\cos(k_{z1}h)+jk_{z1}\sin(k_{z1}h)\right]\,k_\rho^3dk_\rho,\end{aligned}$$

(3.60)

where

$$k_xk_y = \frac{1}{2}k_\rho^2\sin(2\psi),$$

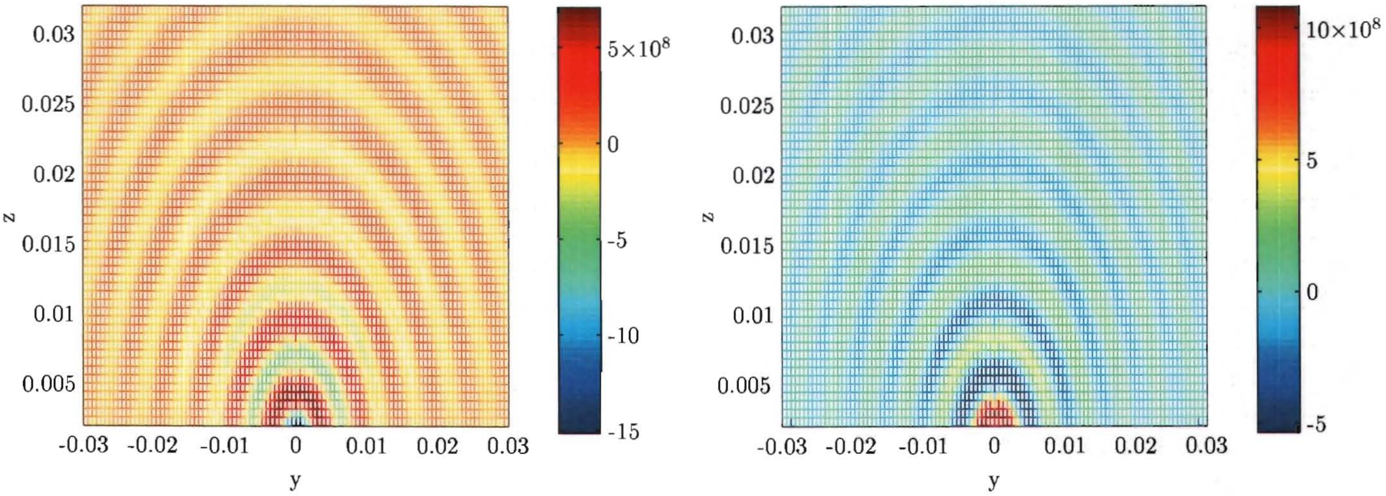

Figure 3.4: Electric field in the yz-plane (x-component); real part (left) and imaginary part (right)

$$\begin{aligned}\int_{2\pi} e^{-jk_\rho r\cos(\psi-\phi)}d\psi &= 2\pi J_0(k_\rho r),\\ \int_{2\pi} e^{-jk_\rho r\cos(\psi-\phi)}\cos^2\psi d\psi &= \pi\left[J_0(k_\rho r)-J_2(k_\rho r)\cos(2\phi)\right],\\ \int_{2\pi} e^{-jk_\rho r\cos(\psi-\phi)}\sin(2\psi)d\psi &= 2\pi J_2(k_\rho r)\sin(2\phi),\end{aligned} \tag{3.61}$$

is used. For the numerical evaluation of these integrals, $K_\rho = 40k_0$ is chosen. Fig. 3.4 and 3.5 show the electric field in the yz-plane, which corresponds to $\phi = \frac{1}{2}\pi$, for $0.002 \leq z \leq 0.032$ and $-0.03 \leq y \leq -0.03$. It is clear that the wavelength is approximately equal to 5 mm, which corresponds to a frequency of 60 GHz.

3.4 Generic structures using the Method of Moments

The modelling of a generic structure on top of the dielectric slab is considered. The fields, resulting from this structure, are calculated using the Method of Moments.

3.4.1 Formulation

The structure is excited by an excitation field $\vec{E}^{ex}$. The resulting field $\vec{E}^s$ is expressed in terms of the unknown current distribution on the structure, using the Green's function calculated in the previous section. The first step is to expand the unknown current distribution in a set of expansion functions, or *basis functions*, according to

$$\vec{J}(\vec{r}) = \sum_n I_n \vec{J}_n(\vec{r}). \tag{3.62}$$

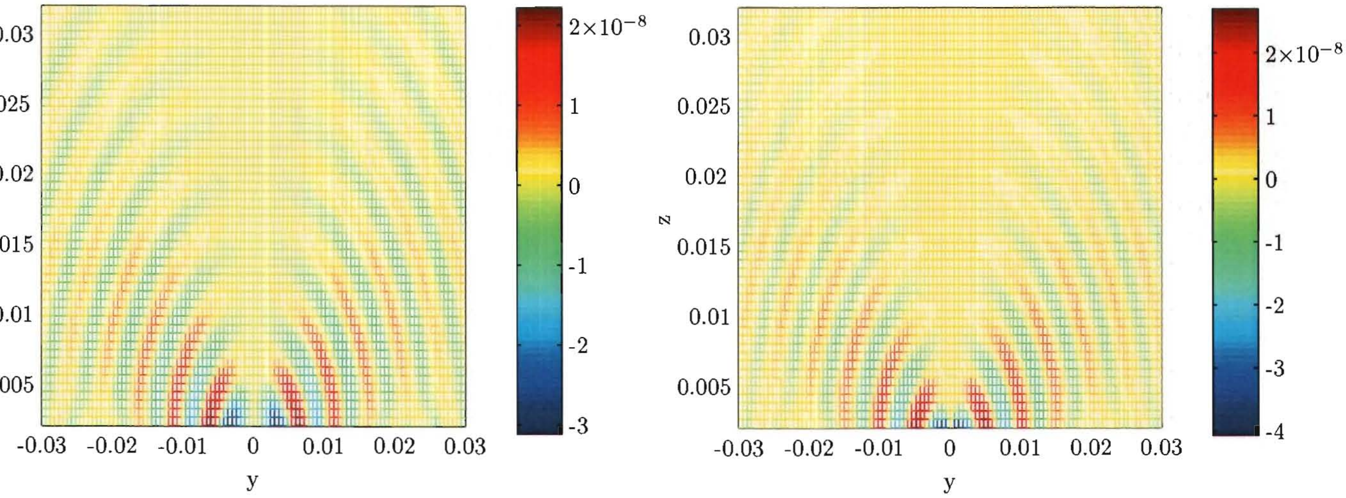

Figure 3.5: Electric field in the yz-plane (y-component); real part (left) and imaginary part (right)

Under the assumption that the current distribution only has transverse components, we can write the expansion functions as (Eq. (3.18))

$$\vec{J}_n(\vec{r}) = \vec{\Upsilon}_n(x,y)\delta(z-h) = \begin{pmatrix} v_{nx} \\ v_{ny} \\ 0 \end{pmatrix} \delta(z-h). \tag{3.63}$$

On the structure, the boundary condition

$$\vec{u}_z \times \left(\vec{E}^{ex}(\vec{r}) + \vec{E}^s(\vec{r})\right) = \vec{0} \tag{3.64}$$

holds, where $\vec{u}_z$ is the unit vector, perpendicular to the surface of the structure. We can also expand $\vec{E}^s$ into a complete set of expansion functions $\vec{E}^s_n$, $1 \leq n \leq N$. Using Eq. (3.45), this results in

$$\begin{aligned}
\vec{E}^s(\vec{r}) &= -\frac{j\omega\mu}{4\pi^2k^2}\int_{k_x}\int_{k_y} \hat{\hat{Q}}(k_x,k_y,z)\cdot\hat{\vec{\Upsilon}}(k_x,k_y)e^{-jk_x x}e^{-jk_y y}dk_x dk_y \\
&= -\frac{j\omega\mu}{4\pi^2k^2}\int_{k_x}\int_{k_y} \hat{\hat{Q}}(k_x,k_y,z)\cdot\left[\sum_n I_n\hat{\vec{\Upsilon}}_n(k_x,k_y)\right]e^{-jk_x x}e^{-jk_y y}dk_x dk_y \\
&= \sum_n I_n\left[-\frac{j\omega\mu}{4\pi^2k^2}\int_{k_x}\int_{k_y} \hat{\hat{Q}}(k_x,k_y,z)\cdot\hat{\vec{\Upsilon}}_n(k_x,k_y)e^{-jk_x x}e^{-jk_y y}dk_x dk_y\right] \\
&= \sum_n I_n\vec{E}^s_n(\vec{r}).
\end{aligned} \tag{3.65}$$

The number of expansion functions is limited to N_{max}. The more expansion functions are used, the longer it takes to compute, but the more accurate the solution will be. Eq. (3.64) now becomes

$$\vec{u}_z \times \left(\vec{E}^{ex}(\vec{r}) + \sum_{n=1}^{N_{max}} I_n\vec{E}^s_n(\vec{r})\right) = \vec{u}_z \times \vec{R}(\vec{r}), \tag{3.66}$$

where $\vec{R}(\vec{r})$ is called the *residue*, which is the deviation from the exact solution due to the limited number of expansion functions. This residue is *weighted to zero* with the use of so called *test* *functions* $\vec{J}_m$, $1 \leq m \leq M$, according to

$$\int_{V_0} \vec{R}(\vec{r}_0) \cdot \vec{J}_m(\vec{r}_0)\; dV_0 = 0. \tag{3.67}$$

By expanding $\vec{R}(\vec{r}_0)$ in this equation, we obtain the matrix equation

$$\begin{aligned}
\int_{V_0} \left[\vec{E}^{ex}(\vec{r}_0) + \sum_{n=1}^{N_{max}} I_n \vec{E}^s_n(\vec{r}_0) \right] \vec{J}_m(\vec{r}_0)\; dV_0 &= 0, \\
\int_{V_0} \vec{E}^{ex}(\vec{r}_0)\vec{J}_m(\vec{r}_0)\; dV_0 + \sum_{n=1}^{N_{max}} I_n \left[\int_{V_0} \vec{E}^s_n(\vec{r}_0)\vec{J}_m(\vec{r}_0)\; dV_0 \right] &= 0, \\
V_m + \sum_{n=1}^{N_{max}} I_n Z_{mn} &= 0, \\
[V] + [Z]\,[I] &= 0,
\end{aligned} \tag{3.68}$$

where $[V]$ is a column vector of length M, $[Z]$ an $M \times N$ matrix and $[I]$ a column vector of length N. When Galerkin's method is used, i.e. the expansion functions and test functions are identical, $M = N$ and the matrix $[Z]$ becomes square and symmetrical. In the spectral domain representation of MoM the test functions are evaluated in the spectral domain as well. This results in a spectral domain representation of $[V]$, according to

$$\begin{aligned}
V_m &= \int_{V_0} \vec{E}^{ex}(\vec{r}_0)\vec{J}_m(\vec{r}_0)\; dV_0 \\
&= \int_{V_0} \left[\frac{1}{4\pi^2} \int_{k_x} \int_{k_y} \hat{\vec{E}}^{ex}(k_x, k_y, z_0) e^{-jk_x x_0} e^{-jk_y y_0} dk_x dk_y \right] \vec{J}_m(\vec{r}_0)\; dV_0 \\
&= \frac{1}{4\pi^2} \int_{k_x} \int_{k_y} \left[\int_{V_0} \hat{\vec{E}}^{ex}(k_x, k_y, z_0) \vec{J}_m(\vec{r}_0) e^{-jk_x x_0} e^{-jk_y y_0}\; dV_0 \right]\; dk_x dk_y \\
&= \frac{1}{4\pi^2} \int_{k_x} \int_{k_y} \hat{\vec{E}}^{ex}(k_x, k_y, h) \hat{\vec{\Upsilon}}_m(-k_x, -k_y)\; dk_x dk_y \\
&= \frac{1}{4\pi^2} \int_{k_x} \int_{k_y} \hat{\vec{E}}^{ex}(k_x, k_y, h) \hat{\vec{\Upsilon}}^*_m(k_x, k_y)\; dk_x dk_y \\
&= \frac{1}{4\pi^2} \int_{k_x} \int_{k_y} \hat{E}^{ex}_x \hat{\upsilon}^*_{mx} + \hat{E}^{ex}_y \hat{\upsilon}^*_{my}\; dk_x dk_y,
\end{aligned} \tag{3.69}$$

where the relation $\hat{\mathcal{F}}(-k) = \hat{\mathcal{F}}^*(k)$ is used. The elements of $[Z]$ in the spectral domain representation are

$$\begin{aligned}
Z_{mn} &= \int_{V_0} \vec{E}^s_n(\vec{r}_0)\vec{J}_m(\vec{r}_0)\; dV_0 \\
&= \int_{V_0} \left[-\frac{j\omega\mu}{4\pi^2 k^2} \int_{k_x} \int_{k_y} \hat{\bar{\bar{Q}}}(k_x, k_y, z_0) \hat{\vec{\Upsilon}}_n(k_x, k_y) e^{-jk_x x_0} e^{-jk_y y_0} dk_x dk_y \right] \vec{J}_m(\vec{r}_0)\; dV_0 \\
&= -\frac{j\omega\mu}{4\pi^2 k^2} \int_{k_x} \int_{k_y} \left[\int_{V_0} \left[\hat{\bar{\bar{Q}}}(k_x, k_y, z_0) \hat{\vec{\Upsilon}}_n(k_x, k_y) \right] \vec{J}_m(\vec{r}_0) e^{-jk_x x_0} e^{-jk_y y_0}\; dV_0 \right]\; dk_x dk_y \\
&= -\frac{j\omega\mu}{4\pi^2 k^2} \int_{k_x} \int_{k_y} \left[\hat{\bar{\bar{Q}}}(k_x, k_y, h) \hat{\vec{\Upsilon}}_n(k_x, k_y) \right] \hat{\vec{\Upsilon}}_m(-k_x, -k_y)\; dk_x dk_y \\
&= -\frac{j\omega\mu}{4\pi^2 k^2} \int_{k_x} \int_{k_y} \left[\hat{\bar{\bar{Q}}}(k_x, k_y, h) \hat{\vec{\Upsilon}}_n(k_x, k_y) \right] \hat{\vec{\Upsilon}}^*_m(k_x, k_y)\; dk_x dk_y \\
&= -\frac{j\omega\mu}{4\pi^2 k^2} \int_{k_x} \int_{k_y} (\hat{q}_{xx}\hat{\upsilon}_{nx} + \hat{q}_{xy}\hat{\upsilon}_{ny})\hat{\upsilon}^*_{mx} + (\hat{q}_{yx}\hat{\upsilon}_{nx} + \hat{q}_{yy}\hat{\upsilon}_{ny})\hat{\upsilon}^*_{my}\; dk_x dk_y.
\end{aligned} \tag{3.70}$$

The elements of $\hat{\bar{\bar{Q}}}$ that are needed to compute Z_{mn} in medium 2 are given by Eq. (3.48), (3.49) and (3.50). Once the elements of the $[V]$ and $[Z]$ matrices are known, the unknown current vector $[I]$ can be obtained easily from

$$[I] = -[Z]^{-1}[V] \tag{3.71}$$

3.4.2 Basis Functions

The unknown current distribution is expanded into a number of *rooftop* basis functions [19]. In case of a generic structure, the rooftop functions can be x-directed or y-directed. They are composed of an x-component, which only depends on x, and a y-component, which only depends on y:

$$f(x, y) = g(x) \cdot h(y).$$

In our application, the rooftop functions are placed at discrete positions in space, equidistant from each other, i.e. on a grid. The position on this grid is denoted with the subscript pq.
For an x-directed rooftop function, the x-component is given by

$$g_{pq,x}(x) = \Lambda\left(\frac{x - p\Delta x}{\Delta x}\right), \tag{3.72}$$

where $\Lambda(\cdot)$ is called the *triangular* function and is defined as

$$\Lambda(x) = \begin{cases} 1 - |x|, & -1 \leq x \leq 1 \\ 0, & \text{otherwise} \end{cases}, \tag{3.73}$$

and the y-component is given by

$$h_{pq,x}(y) = \Pi\left(\frac{y - 2q\Delta y}{2\Delta y}\right), \tag{3.74}$$

where $\Pi(\cdot)$ is called the *rectangular* function and is defined as

$$\Pi(x) = \begin{cases} 1, & -1/2 \leq x \leq 1/2 \\ 0, & \text{otherwise} \end{cases}. \tag{3.75}$$

Rooftop functions have a size of $2\Delta x \times 2\Delta y$. For y-directed rooftop functions, the following applies:

$$\begin{aligned} g_{pq,y}(x) &= h_{pq,x}(x), \\ h_{pq,y}(y) &= g_{pq,x}(y). \end{aligned} \tag{3.76}$$

The spectral domain representation of the rooftop function is found by performing a spatial-to-spectral domain Fourier transform (App. A) and is given by

$$\begin{aligned} \hat{f}_{pq,x}(k_x, k_y) &= \hat{g}_{pq,x}(k_x)\hat{h}_{pq,x}(k_y) = \frac{8}{k_x^2 k_y \Delta x} \sin^2\left(k_x \frac{\Delta x}{2}\right) \sin(k_y \Delta y) e^{jpk_x\Delta x} e^{jqk_y\Delta y}, \\ \hat{f}_{pq,y}(k_x, k_y) &= \hat{g}_{pq,y}(k_x)\hat{h}_{pq,y}(k_y) = \frac{8}{k_x k_y^2 \Delta y} \sin(k_x \Delta x) \sin^2\left(k_y \frac{\Delta y}{2}\right) e^{jpk_x\Delta x} e^{jqk_y\Delta y}. \end{aligned} \tag{3.77}$$

If rooftop basis functions are used, they are usually positioned on a grid with a fixed distance between them. Along the direction in which the rooftops have a triangular shape, they have an overlap, as shown in Fig. 3.6. Along the other direction they are placed next to each other, so have no overlap.
Both the unknown x-directed current and y-directed current can be expressed in terms of a sum of x-directed and y-directed rooftop functions. If $\vec{\Upsilon}_i(x, y)$ is situated at position $p_i q_i$, the following relations apply:

$$\vec{\Upsilon}_i(x, y) = v_{ix}(x, y)\vec{u}_x + v_{iy}(x, y)\vec{u}_y$$

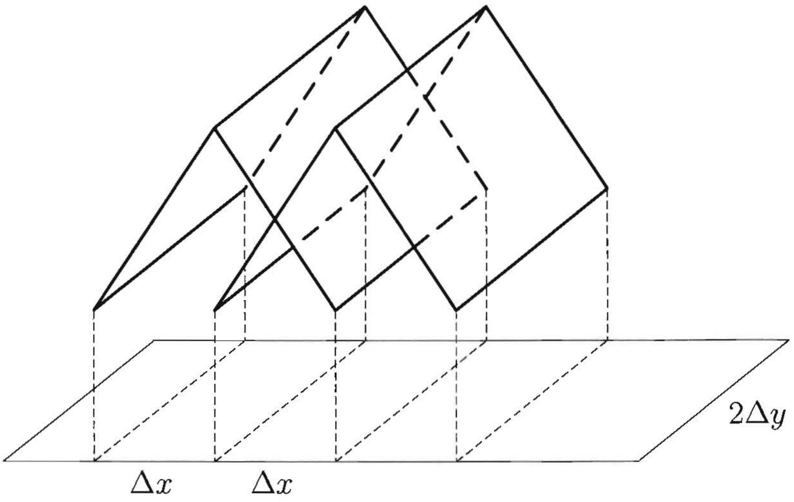

Figure 3.6: Layout of rooftop basis functions

$$\begin{aligned}
&= f^x_{p_iq_i}(x,y)\vec{u}_x + f^y_{p_iq_i}(x,y)\vec{u}_y \\
&= \left[f^x_{p_iq_i,x}(x,y) + f^x_{p_iq_i,y}(x,y)\right]\vec{u}_x + \left[f^y_{p_iq_i,x}(x,y) + f^y_{p_iq_i,y}(x,y)\right]\vec{u}_y \qquad (3.78) \\
\hat{\vec{\Upsilon}}_i(k_x,k_y) &= \left[\hat{f}^x_{p_iq_i,x}(k_x,k_y) + \hat{f}^x_{p_iq_i,y}(k_x,k_y)\right]\vec{u}_x + \left[\hat{f}^y_{p_iq_i,x}(k_x,k_y) + \hat{f}^y_{p_iq_i,y}(k_x,k_y)\right]\vec{u}_y \qquad (3.79)
\end{aligned}$$

where $\hat{f}^x_{p_iq_i,x}(k_x,k_y)$, $\hat{f}^x_{p_iq_i,y}(k_x,k_y)$, $\hat{f}^y_{p_iq_i,x}(k_x,k_y)$ and $\hat{f}^y_{p_iq_i,y}(k_x,k_y)$ are given by Eq. (3.77). The superscript of $\hat{f}$ denotes to which component of the current it contributes, but does not affect its form.

3.4.3 Input impedance

Once the current coefficients are known, it is possible to calculate the input impedance of the structure. To this end, we take a closer look at the modelling of the source. We first take a look at the source model in circuit theory, and then translate this model to the electromagnetic domain. Fig. 3.7 shows an example of a structure with a source located in the centre. It shows the source voltage (V_s), the source current (I_s), the circuit voltage (V_c) and the circuit current (I_c). Note that the source current is defined in the opposite direction of the circuit current. The input impedance of a circuit is calculated by dividing the voltage drop across the circuit by the current through the circuit. This results in

$$Z_{in} = \frac{V_c}{I_c} = -\frac{V_s}{I_s} = -\frac{V_s I_s^*}{I_s I_s^*} = -\frac{2P_s}{|I_s|^2}, \qquad (3.80)$$

where $P_s = \frac{1}{2}V_s I_s^*$ is defined as the complex harmonic power, delivered by the source. In the electromagnetic domain, the source is modelled according to Fig 3.8. It shows the source electric field ($\vec{E}^{ex}$), the source current density ($\vec{J}^{ex}$), the (electromagnetic circuit) electric field ($\vec{E}$) and the (electromagnetic circuit) current density ($\vec{J}$). Note that the source current density is again defined in the opposite direction of the circuit current density. The input impedance of an electromagnetic system is defined analogous to Eq. (3.80) as

$$Z_{in} = -\frac{2P^{ex}}{|I^{ex}|^2} = -\frac{1}{|I^{ex}|^2}\int_{V_0} \vec{E}^{ex} \cdot \vec{J}^{ex*}\, dV_0,$$

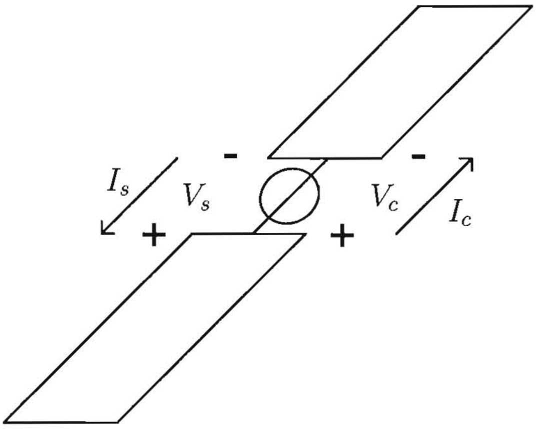

Figure 3.7: Source model in the circuit domain

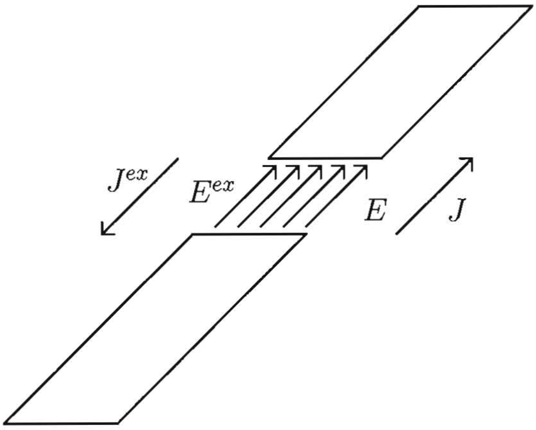

Figure 3.8: Source model in the electromagnetic domain

where I^{ex} is the total excitation current, i.e

$$I^{ex} = \int_{V_0} \vec{J}^{ex}\, dV_0,$$

and where

$$P^{ex} = \frac{1}{2}\int_{V_0} \vec{E}^{ex} \cdot \vec{J}^{ex*}\, dV_0.$$

Furthermore, we define

$$I = \int_{V_0} \vec{J}\, dV_0.$$

Using $\vec{J} = -\vec{J}^{ex}$, $\vec{I} = -\vec{I}^{ex}$, Eq. (3.62), (3.69) and (3.71), we can write this as

$$\begin{aligned} Z_{in} &= \frac{1}{|I|^2}\int_{V_0} \vec{E}^{ex} \cdot \vec{J}^{*}\, dV_0 \\ &= \frac{1}{|I|^2}\int_{V_0} \vec{E}^{ex} \cdot \sum_n I_n^* \vec{J}_n^*\, dV_0 \\ &= \frac{1}{|I|^2}\sum_n I_n^* \int_{V_0} \vec{E}^{ex} \cdot \vec{J}_n^*\, dV_0 \\ &= \frac{1}{|I|^2}\sum_n I_n^* V_n \\ &= \frac{1}{|I|^2}[V]^T [I]^* \\ &= -\frac{1}{|I|^2}[V]^T \left([Z]^{-1}\right)^* [V]^*. \end{aligned} \tag{3.81}$$

3.5 Example problem: microstrip dipole

As an example, a microstrip dipole antenna, oriented in the x-direction, is considered. The source is modelled as an infinitely narrow voltage gap (a *delta gap*) in the x-direction along the width w of the microstrip dipole with amplitude equal to unity. The centre of the dipole is located at (x_s, y_s, h). It can be written as

$$\vec{E}^{ex}(x_0, y_0, z_0) = \Pi\left(\frac{y_0 - y_s}{w}\right)\delta(x_0 - x_s, z_0 - h) \cdot \vec{u}_x. \tag{3.82}$$

The spectral domain representation is:

$$\vec{E}^{ex}(k_x, k_y) = \frac{2}{k_y} \sin\left(k_y \frac{w}{2}\right) e^{jk_x x_s} e^{jk_y y_s} \cdot \vec{u}_x. \tag{3.83}$$

The source coordinates are on the same grid as the basis functions of our MoM formulation, so $x_s = a\Delta x,\ y_s = b\Delta y$, where a and b are integers. If we assume that the resulting unknown current distribution only has an x-component, which is modelled with x-directed rooftop basis functions only, we have

$$\hat{\vec{\Upsilon}}^*_m(k_x, k_y) = \hat{v}^*_{mx}\vec{u}_x = \hat{f}^{x*}_{p_m q_m, x}(k_x, k_y)\vec{u}_x. \tag{3.84}$$

Therefore, the components of the V-matrix (Eq. (3.69)) evaluate to

$$\begin{aligned}
V_m &= \frac{1}{4\pi^2}\int_{k_x}\int_{k_y} \hat{E}^{ex}_x(k_x, k_y) \cdot \hat{f}^{x*}_{p_m q_m, x}(k_x, k_y)\ dk_x dk_y \\
&= \frac{1}{4\pi^2}\int_{k_x}\int_{k_y} \frac{2}{k_y}\sin\left(k_y\frac{w}{2}\right) e^{jk_x a\Delta x} e^{jk_y b\Delta y}\ . \\
&\qquad \frac{8}{k_x^2 k_y \Delta x}\sin^2\left(\frac{k_x}{2}\Delta x\right)\sin(k_y\Delta y) e^{-jp_m k_x \Delta x} e^{-jq_m k_y \Delta y}\ dk_x dk_y \\
&= \frac{1}{4\pi^2}\int_{k_x}\int_{k_y} \frac{16}{k_x^2 k_y^2 \Delta x}\sin^2\left(\frac{k_x}{2}\Delta x\right)\sin(k_y\Delta y)\sin\left(k_y\frac{w}{2}\right)\ e^{jk_x(a-p_m)\Delta x} e^{jk_y(b-q_m)\Delta y}\ dk_x dk_y \\
&= \begin{cases} \min(2\Delta y, w), & p_m = a \wedge q_m = b \\ 0, & \text{otherwise} \end{cases}\ ,
\end{aligned} \tag{3.85}$$

where $\min(\cdot)$ is the function that takes the minimum value of its arguments. If we choose $\Delta y = w/2$, which is a convenient choice, Eq. (3.85) reduces to

$$V_m = \begin{cases} w, & p_m = a \wedge q_m = b \\ 0, & \text{otherwise} \end{cases}\ . \tag{3.86}$$

Under the assumption of Eq. (3.84), the components of the Z-matrix (Eq. (3.70)) evaluate to

$$\begin{aligned}
Z_{mn} &= -\frac{j\omega\mu}{4\pi^2 k^2}\int_{k_x}\int_{k_y} \hat{q}_{xx}\hat{v}_{nx}\hat{v}^*_{mx}\ dk_x dk_y \\
&= -\frac{j\omega\mu}{4\pi^2 k^2}\int_{k_x}\int_{k_y} \hat{q}_{xx}\hat{f}^{x}_{p_n q_n, x}(k_x, k_y)\hat{f}^{x*}_{p_m q_m, x}(k_x, k_y)\ dk_x dk_y \\
&= -\frac{j\omega\mu}{4\pi^2 k^2}\int_{k_x}\int_{k_y} \hat{q}_{xx}\hat{f}^{x}_{p_n q_n, x}(k_x, k_y)\hat{f}^{x}_{p_m q_m, x}(-k_x, -k_y)\ dk_x dk_y \\
&= -\frac{j\omega\mu}{4\pi^2 k^2}\int_{k_x}\int_{k_y} \hat{q}_{xx}\left[\frac{8}{k_x^2 k_y \Delta x}\sin^2\left(\frac{k_x}{2}\Delta x\right)\sin(k_y\Delta y)\right]^2 e^{j(p_n-p_m)k_x\Delta x} e^{j(q_n-q_m)k_y\Delta y}\ dk_x dk_y.
\end{aligned} \tag{3.87}$$

We evaluate this integral in medium 2 with $z = h$, so $\hat{q}_{xx} = \hat{q}_{2xx}$, which is given by Eq. (3.48). The previous equation then evaluates to

$$\begin{aligned}
Z_{mn} &= -\frac{j\omega\mu}{4\pi^2 k_2^2}\int_{k_x}\int_{k_y} \hat{q}_{2xx}\frac{64}{k_x^4 k_y^2 (\Delta x)^2}\sin^4\left(\frac{k_x}{2}\Delta x\right)\sin^2(k_y\Delta y) e^{j(p_n-p_m)k_x\Delta x} e^{j(q_n-q_m)k_y\Delta y}\ dk_x dk_y \\
&= -\frac{j\omega\mu}{4\pi^2 k_0^2}\int_{k_x}\int_{k_y} \frac{\sin(k_{z1}h)}{T_e T_m}\left[k_0^2 T_m - k_x^2\left(k_{z2}\cos(k_{z1}h) + jk_{z1}\sin(k_{z1}h)\right)\right] \cdot \\
&\qquad \frac{64}{k_x^4 k_y^2 (\Delta x)^2}\sin^4\left(\frac{k_x}{2}\Delta x\right)\sin^2(k_y\Delta y) e^{j(p_n-p_m)k_x\Delta x} e^{j(q_n-q_m)k_y\Delta y}\ dk_x dk_y.
\end{aligned} \tag{3.88}$$

The parameters in this example problem are the number of rooftop basis functions (M), the length of the dipole (l), the width of the dipole (w), the height of the substrate (h), the permittivity of the dielectric (ε_{r1}) and the permittivity of the medium above the dielectric (ε_{r2}). They are chosen according to

$$\begin{aligned} M &= 7, \\ l &= 0.5\lambda_{eff}, \\ w &= 0.05\lambda_{eff}, \\ h &= 1 \text{ mm}, \\ \varepsilon_{r1} &= 2, \\ \varepsilon_{r2} &= 1, \end{aligned}$$

where $\lambda_{eff} = \lambda_0/\sqrt{\varepsilon_{r1}}$, the wavelength in the dielectric. To obtain an initial approximation of the solution, a number of 7 rooftop basis functions is sufficient. The dipole is designed for a nominal frequency of 60 GHz, so $\lambda_0 \approx 5$ mm. The width of the rooftop functions is chosen equal to the width of the dipole, so $\Delta y = w/2$. In order to cover the entire dipole, the length of the rooftops must be equal to $2l/(M+1)$. Because $M = 7$, $\Delta x = l/8$.

Input impedance simplified

With $[V]$, $[Z]$ and $[I]$ available, the input impedance can be calculated using Eq. (3.81). However, a simpler expression is obtained if we evaluate Eq. (3.81) directly. In the source region, we have

$$\begin{aligned} \vec{E}^{ex}(x_0, y_0, z_0) &= \Pi\left(\frac{y_0 - y_s}{w}\right)\delta(x_0 - x_s, z_0 - h) \cdot \vec{u}_x, \\ \vec{J}^{ex}(x_0, y_0, z_0) &= -I_{n_s}\Lambda\left(\frac{x_0 - x_s}{l/8}\right)\Pi\left(\frac{y_0 - y_s}{w}\right) \cdot \vec{u}_x, \\ I^{ex} &= \int_{V_0} \vec{J}^{ex}\, dV_0, \\ &= \int_{V_0} -I_{n_s}\Lambda\left(\frac{x_0 - x_s}{l/8}\right)\Pi\left(\frac{y_0 - y_s}{w}\right) \cdot \vec{u}_x\, dV_0, \\ &= -I_{n_s} w \cdot \vec{u}_x, \end{aligned} \tag{3.89}$$

where n_s is the index of the rooftop basis function that is located at (x_0, y_0, h). Combining Eq. (3.81) with Eq. (3.89) results in

$$\begin{aligned} Z_{in} &= -\frac{1}{|I^{ex}|^2}\int_{V_0} \vec{E}^{ex} \cdot \vec{J}^{ex*}\, dV_0 \\ &= -\frac{1}{|I_{n_s} w|^2}\int_{V_0} \Pi\left(\frac{y_0 - y_s}{w}\right)\delta(x_0 - x_s, z_0 - h) \cdot -I_{n_s}^*\Lambda\left(\frac{x_0 - x_s}{l/8}\right)\Pi\left(\frac{y_0 - y_s}{w}\right) dV_0 \\ &= \frac{I_{n_s}^*}{|I_{n_s} w|^2}\int_{y_0} \Pi^2\left(\frac{y_0 - y_s}{w}\right) dy_0 \\ &= \frac{I_{n_s}^* w}{|I_{n_s} w|^2} \\ &= \frac{1}{I_{n_s} w}. \end{aligned} \tag{3.90}$$

Results

The elements of the Z-matrix (Eq. (3.88)) are evaluated using the numerical approach of Section 3.3.6, with $K_\rho = 100k_0$. For the nominal frequency of 60 GHz, the resulting current distribution is plotted in Fig. 3.9. The directivity of the structure is calculated using Eq. (B.1), (B.6)

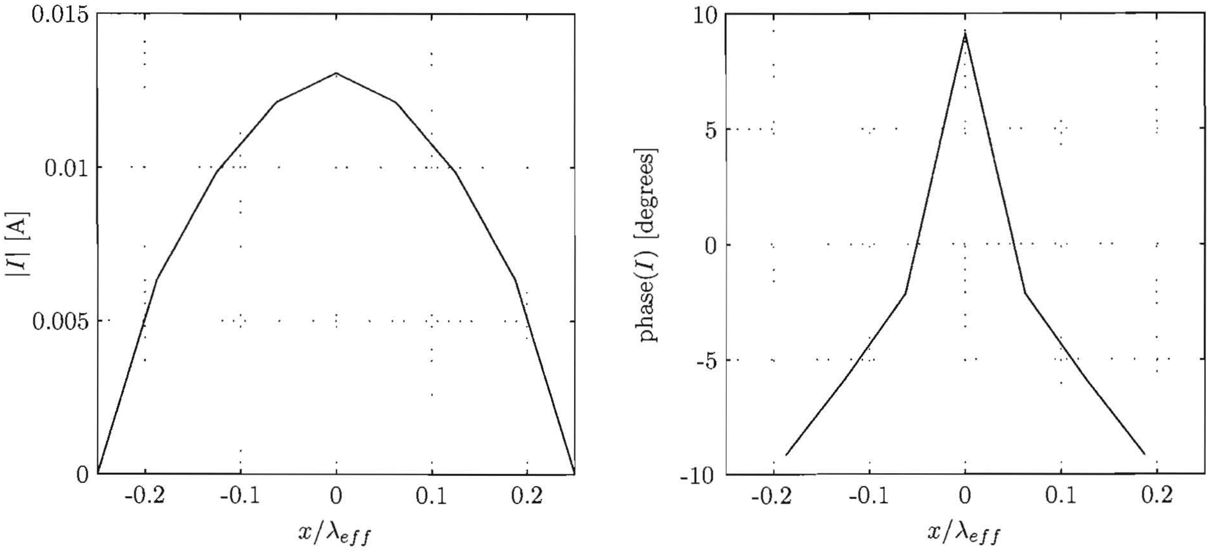

Figure 3.9: Current distribution the dipole; magnitude (left) and angle (right)

and (3.51). The result is shown in Fig. 3.10. The radiation efficiency is calculated using Eq. (B.9) and is equal to 0.84. The input impedance of the structure is calculated using Eq. (3.81) for the frequency band of 40 GHz - 80 GHz. The result is shown in Fig. 3.11. For 60 GHz, the input impedance is equal to $75.6 - j12.1\ \Omega$.

3.6 Conclusion

To model a simplified alternative for the final deflector element, the modelling and analysis of generic planar structures on top of a grounded dielectric slab has been performed. To this end, the field solution of a system containing only isotropic, homogeneous, linear, time-invariant materials have been given. The vector potential and Green's function have been introduced. The field solution of the grounded dielectric slab has been given, using the Green's function, found by applying the proper boundary conditions. A generic structure on top of the slab has been modelled, using the Method of Moments. To illustrate this, a microstrip dipole antenna has been given as an example.

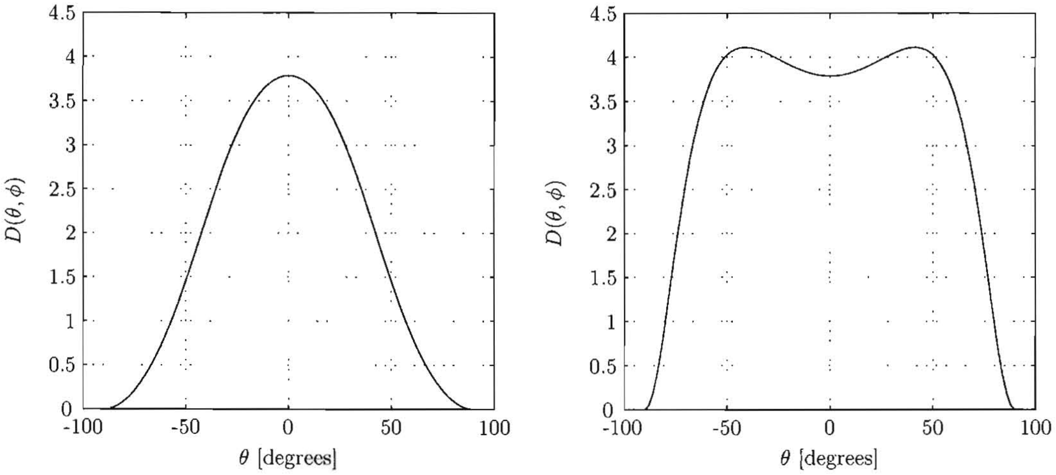

Figure 3.10: Directivity of the dipole; θ-cut; $\phi = 0°$ (left) and $\phi = 90°$ (right)

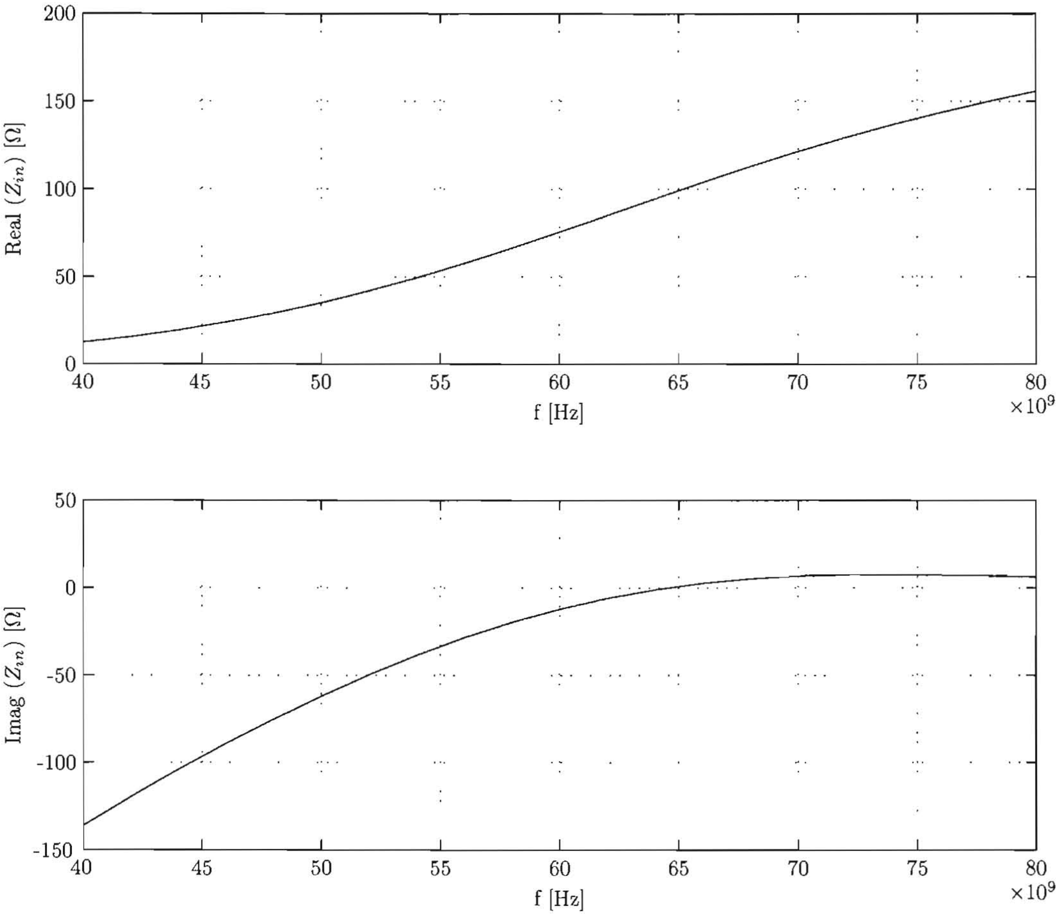

Figure 3.11: Input impedance of the dipole; real part (above) and imaginary part (below)

Chapter 4

Optimization of antenna structures

4.1 Introduction

To obtain an optimized design for the deflector element, an optimization method is presented. The design is optimized by maximising or minimising a certain *cost function*, that itself is a function of a predefined parameter vector. This parameter vector consists of several antenna parameters, that can be adjusted to optimize the antenna structure. One challenge in optimizing an antenna structure is to find a global optimum (within a predefined domain), rather than a local optimum. In Section 4.2, an optimization approach is introduced. The cost function and a convenient form of it is given in Section 4.3. In Section 4.4, the method is applied to the example of the microstrip dipole, given in Chapter 3, and results are given.

4.2 Approach

In general, the cost function is not available in closed form. The global optimum is obtained by finding a closed-form approximation of the cost function by means of a Taylor expansion (App. C). We assume that the Taylor expansion converges on the domain of interest. Once this closed-form approximation is available, finding a global optimum is straightforward, if one optimization parameter is considered. Other (iterative) methods often yield a local optimum, which is not necessarily global.

4.3 Cost function

4.3.1 Definition

The cost function is defined as a real valued function that maps a parameter vector to a cost value. This can be written as

$$\Gamma : \vec{p} \to \gamma. \tag{4.1}$$

The particular choice of $\vec{p}$ that results in a global optimum γ^* is denoted by $\vec{p}^{\,*}$. In general, the cost function is both a direct and an implicit function of the parameters. This will be clarified by an example in Section 4.4. We express this relation as

$$\Gamma(\vec{p}) = \Gamma(\vec{p}, \zeta(\vec{p})), \tag{4.2}$$

where $\Gamma(\vec{p}, \cdot)$ denotes the direct dependence of Γ on $\vec{p}$ and $\Gamma(\cdot, \zeta(\vec{p}))$ the implicit dependence on $\vec{p}$.

4.3.2 Least squares cost function

The purpose of optimization is often to make a certain characteristic of the structure approach an optimal value as close as possible. This can be done by choosing a *least squares cost* function, which has the form

$$\Gamma(\vec{p}, \zeta(\vec{p})) = |f(\vec{p}, \zeta(\vec{p})) - f_{opt}|^2, \tag{4.3}$$

where $|\cdot|$ is the modulus and f_{opt} denotes an optimal value.

4.3.3 Derivatives

In order to find a Taylor expansion of the cost function, the derivatives need to be calculated. The derivatives of the least squares cost function (Eq. (4.3)) can be expressed in terms of the *complex element-wise product* (App. F). Therefore, we express the cost function as (Eq. (F.11))

$$\begin{aligned}\Gamma(\vec{p}, \zeta(\vec{p})) &= |f(\vec{p}, \zeta(\vec{p})) - f_{opt}|^2 \\ &= \{(f(\vec{p}, \zeta(\vec{p})) - f_{opt}) \circledast (f(\vec{p}, \zeta(\vec{p})) - f_{opt})\} \\ &= \{f(\vec{p}, \zeta(\vec{p})) \circledast f(\vec{p}, \zeta(\vec{p})) - 2f(\vec{p}, \zeta(\vec{p})) \circledast f_{opt} + f_{opt} \circledast f_{opt}\}.\end{aligned} \tag{4.4}$$

Taking the n^{th} order derivative with respect to $\vec{p}$ of $\Gamma(\vec{p}, \zeta(\vec{p}))$ results in (Eq. (F.9))

$$\begin{aligned}\nabla^n_{\vec{p}}\Gamma(\vec{p}, \zeta(\vec{p})) &= \nabla^n_{\vec{p}}\{f(\vec{p}, \zeta(\vec{p})) \circledast f(\vec{p}, \zeta(\vec{p})) - 2f(\vec{p}, \zeta(\vec{p})) \circledast f_{opt} + f_{opt} \circledast f_{opt}\} \\ &= \left\{\nabla^n_{\vec{p}}\left[f(\vec{p}, \zeta(\vec{p})) \circledast f(\vec{p}, \zeta(\vec{p}))\right] - 2\nabla^n_{\vec{p}}\left[f(\vec{p}, \zeta(\vec{p})) \circledast f_{opt}\right] + \nabla^n_{\vec{p}}\left[f_{opt} \circledast f_{opt}\right]\right\}.\end{aligned} \tag{4.5}$$

Each of the terms in the equation above can be evaluated using the complex element-wise product-modified Leibniz rule (Eq. (F.8)), which results in an equation involving terms, either of the form

$$\nabla^k_{\vec{p}} f(\vec{p}, \zeta(\vec{p})), \quad \text{or} \tag{4.6}$$

$$\nabla^k_{\vec{p}} f_{opt}, \tag{4.7}$$

with $0 \leq k \leq n$. This can easily be verified by inspecting Eq. (F.8). Evaluation of Eq. (4.7) is straightforward, according to

$$\nabla^k_{\vec{p}} f_{opt} = \begin{cases} f_{opt}, & k = 0 \\ 0, & \text{otherwise} \end{cases}. \tag{4.8}$$

Evaluation of $\nabla^k_{\vec{p}} f(\vec{p}, \zeta(\vec{p}))$ is a little more involved. For clarity, we denote the direct dependence of f on $\vec{p}$ by $\vec{p_d}$ and the implicit dependence of f on $\vec{p}$ by $\vec{p_i}$, according to

$$f(\vec{p}, \zeta(\vec{p})) = f(\vec{p_d}, \zeta(\vec{p_i})). \tag{4.9}$$

The derivative of Eq. (4.9) is

$$\nabla_{\vec{p}} f(\vec{p_d}, \zeta(\vec{p_i})) = \nabla_{\vec{p_d}} f(\vec{p_d}, \zeta(\vec{p_i})) + \nabla_{\vec{p_i}} f(\vec{p_d}, \zeta(\vec{p_i})), \tag{4.10}$$

so that Eq. (4.6) becomes

$$\begin{aligned}\nabla^k_{\vec{p}} f(\vec{p}, \zeta(\vec{p})) &= \nabla^k_{\vec{p}} f(\vec{p_d}, \zeta(\vec{p_i})) \\ &= \sum_{j=0}^{k} \binom{k}{j} \nabla^j_{\vec{p_d}} \nabla^{k-j}_{\vec{p_i}} f(\vec{p_d}, \zeta(\vec{p_i})).\end{aligned} \tag{4.11}$$

The derivatives to $\vec{p_d}$ and $\vec{p_i}$ are evaluated independently of each other. For a well-defined cost function, it is straightforward to find the derivatives to $\vec{p_d}$ analytically. To evaluate the derivatives to $\vec{p_i}$, we use the multi-variable version of the formula of Faà di Bruno [42], which generalises the chain rule to higher order derivatives of multiple variables:

$$\frac{\partial^n}{\partial x_1 \partial x_2 \cdots \partial x_n} f(g(\vec{x})) = \sum_{q \in Q} \frac{\partial^{|q|} f}{\partial g^{|q|}} \cdot \prod_{B \in q} \frac{\partial^{|B|} g}{\prod_{j \in B} \partial x_j}, \tag{4.12}$$

where

- $q \in Q$ means that q runs through the set Q of all partitions of the set $\{1, \ldots, n\}$,
- $B \in q$ means that the variable B runs through the list of all of the 'blocks' of the partition q, and
- $|A|$ denotes the cardinality of the set A, so that $|q|$ is the number of blocks in the partition q and $|B|$ is the size of the block B.

For an example of this formula, see Section 4.4. The formula holds regardless of whether the variables $x_1 \ldots x_n$ are all distinct, all identical, or partitioned into several distinguishable classes of indistinguishable variables. So the n^{th} order derivative to just one parameter x_ν is found by taking all $x_1 \ldots x_n$ equal to x_ν. It is applied to Eq. (4.11) by taking g equal to ζ and by assigning elements of $\vec{p_i}$ to $\vec{x}$, depending on which derivative is needed.

4.4 Example: microstrip dipole

As an example, the microstrip dipole of Section 3.5 is optimized to match a desired input impedance (Z_{in}) of 50Ω at 60GHz, by varying its length l. The fixed parameters are, like in Section 3.5,

$$\begin{aligned} M &= 7, \\ w &= 0.05\lambda_{eff}, \\ h &= 1 \text{ mm}, \\ \varepsilon_{r1} &= 2, \\ \varepsilon_{r2} &= 1, \\ \Delta y &= w/2 \end{aligned} \tag{4.13}$$

where $\lambda_{eff} = \lambda_0/\sqrt{\varepsilon_{r1}}$ and $\lambda_0 \approx 5$ mm. Because $M = 7$, $\Delta x = l/8$.

4.4.1 Cost function

The cost function is given by Eq. (4.3). Because we want to optimize the input impedance, we use

$$\begin{aligned} f(\vec{p}, \zeta(\vec{p})) &= Z_{in}(w, I_{n_s}(w, l)) \\ &= \frac{1}{[Z^{-1}(l)V(w)]_{n_s} \cdot w} \\ &= \frac{1}{[Z^{-1}]_{44}(l) \cdot w^2} \\ &= f(w, \zeta(l)), \end{aligned} \tag{4.14}$$

where $n_s = 4$, $V(4) = w$ is the only non-zero component of V and $\zeta(l) = [Z^{-1}]_{44}(l)$. Further, we use

$$f_{opt} = 50, \tag{4.15}$$

so

$$\Gamma(\vec{p}, \zeta(\vec{p})) = \left| \frac{1}{[Z^{-1}]_{44}(l) \cdot w^2} - 50 \right|^2, \tag{4.16}$$

where w is the width of the microstrip dipole and l is the length of the dipole. To optimize the input impedance of the structure, the cost function (Eq. (4.16)) has to be minimised.

4.4.2 Taylor approximation

A global minimum is found by calculating the Taylor approximation with respect to the length of the structure l, about $l_0 = 0.5\lambda_{eff} = 1.768 \cdot 10^{-3}$ m. The domain on which we perform the optimization (D_{opt}, see App. C) is

$$D_{opt} = \left\{ l \in \mathbb{R} \;\middle|\; 1.6 \cdot 10^{-3} \leq l \leq 1.9 \cdot 10^{-3} \right\}. \tag{4.17}$$

Therefore, the validation points are

$$V = \left\{ l_V \in \partial D_{opt} \;\middle|\; l_V = \{1.6 \cdot 10^{-3}, 1.9 \cdot 10^{-3}\} \right\}. \tag{4.18}$$

The approximation is considered acceptable for $\varepsilon_a = 0.01$.

Derivatives

Calculating the Taylor expansion involves n^{th} order derivatives of $f(w, \zeta(l))$ to l, which are given by (see Eq. (4.11) and Eq. (4.12))

$$\frac{\partial^n}{\partial l^n} f(w, \zeta(l)) = \sum_{q \in Q} \frac{\partial^{|q|} f}{\partial \zeta^{|q|}} \cdot \prod_{B \in q} \frac{\partial^{|B|} \zeta}{\prod_{j \in B} \partial l}. \tag{4.19}$$

To illustrate the use of this formula, the first and second derivative are given as an example. For the first derivative, $n = 1$ and $Q = \{\{1\}\}$, so the sum consists of only one term, with $q = \{1\}$. In this single term, $B = \{1\}$. The first derivative is given by

$$\frac{\partial}{\partial l} f(\zeta(l)) = \frac{\partial f}{\partial \zeta} \cdot \frac{\partial \zeta}{\partial l}, \tag{4.20}$$

which is the same result we would get by using the ordinary chain rule. For the second derivative, $n = 2$ and $Q = \{\{12\}, \{1, 2\}\}$, so the sum consists of two terms, with $q = \{12\}$ being the first partition and $q = \{1, 2\}$ the second one. For the first term, $B = \{12\}$ and for the second term, $B = \{1\}$ and $B = \{2\}$. So the second derivative is given by

$$\frac{\partial^2}{\partial l^2} f(\zeta(l)) = \frac{\partial f}{\partial \zeta} \cdot \frac{\partial^2 \zeta}{\partial l^2} + \frac{\partial^2 f}{\partial \zeta^2} \cdot \left(\frac{\partial \zeta}{\partial l} \right)^2, \tag{4.21}$$

The n^{th} order derivative of f to ζ is evaluated as

$$\begin{aligned} \frac{\partial^n}{\partial \zeta^n} f(\zeta) &= \frac{\partial^n}{(\partial \left[Z^{-1}\right]_{44})^n} f(\left[Z^{-1}\right]_{44}) \\ &= \frac{\partial^n}{(\partial \left[Z^{-1}\right]_{44})^n} \left(\frac{1}{\left[Z^{-1}\right]_{44} w^2} \right) \\ &= \frac{(-1)^n n!}{(\left[Z^{-1}\right]_{44})^{n+1} w^2}, \end{aligned} \tag{4.22}$$

and the n^{th} order derivative of ζ to l is evaluated as

$$\begin{aligned} \frac{\partial^n}{\partial l^n} \zeta(l) &= \frac{\partial^n}{\partial l^n} \left[Z^{-1}\right]_{44}(l) \\ &= \frac{\partial^{n-1}}{\partial l^{n-1}} \left(\frac{\partial}{\partial l} \left[Z^{-1}\right]_{44}(l) \right) \\ &= \frac{\partial^{n-1}}{\partial l^{n-1}} \left(\left[\frac{\partial Z^{-1}(l)}{\partial l} \right]_{44} \right) \\ &= \frac{\partial^{n-1}}{\partial l^{n-1}} \left(\left[-Z^{-1}(l) \frac{\partial Z(l)}{\partial l} Z^{-1}(l) \right]_{44} \right) \end{aligned}$$

$$= \left(\frac{\partial^{n-1}}{\partial l^{n-1}} \left[-Z^{-1}(l) \frac{\partial Z(l)}{\partial l} Z^{-1}(l) \right] \right)_{44}, \tag{4.23}$$

where, for the fourth equality, we used the identity

$$\frac{\partial A^{-1}}{\partial p} = -A^{-1} \frac{\partial A}{\partial p} A^{-1}, \tag{4.24}$$

where A is a matrix, whose elements are a function of parameter p.
Eq. (4.23) is further evaluated by the rule of Leibniz for higher order derivatives of products of functions, which, eventually, yields an expression containing only the inverse of $Z(l)$ and k^{th} order derivatives of $Z(l)$, $1 \leq k \leq n$. The latter is evaluated in an element-wise fashion. The k^{th} order derivative of Z_{mn} (Eq. (3.70)) is

$$\begin{aligned} \frac{\partial^k}{\partial l^k} Z_{mn} &= \frac{\partial^k}{\partial l^k} \int_{V_0} \vec{E}^s_n(\vec{r}_0, l) \vec{J}_m(\vec{r}_0, l) \; dV_0 \\ &= \int_{V_0} \frac{\partial^k}{\partial l^k} \left(\vec{E}^s_n(\vec{r}_0, l) \vec{J}_m(\vec{r}_0, l) \right) dV_0. \end{aligned} \tag{4.25}$$

The exact result depends on the form of the Green's function and the basis functions used in the MoM approach.

4.4.3 Results

Fig. 4.1 shows the result of the Taylor approximation. It turns out that three orders are sufficient to obtain an acceptable approximation. Note how closely the approximation function matches the original one on D_{opt}. The closed-form approximation is used to find the optimum of the cost function. Setting the first derivative to zero yields an optimum length of $l = 1.739 \cdot 10^{-3}$. This value is found using a numerical polynomial root-finding algorithm. With this length, the input impedance of the microstrip dipole at 60GHz is equal to $71.5 - j17.2\ \Omega$, which is the best match possible, given the other parameter values. By comparison of the absolute values, it is indeed closer to $50\ \Omega$ than the original input impedance of $75.6 - j12.1\ \Omega$.

4.5 Conclusion

In order to optimize the design of the deflector element, an optimization method has been presented. The characteristics of the design, which are of interest, are represented by a cost function. A global optimum is found by approximating the cost function by means of a Taylor expansion. Once the closed-form approximation is available, finding a global optimum is straightforward, if one optimization parameter is considered. The general form of the cost function has been introduced and expressions for its higher order derivatives, used by the Taylor expansion, have been given. As an example of the method, the length of a microstrip dipole has been optimized to match a desired input impedance.

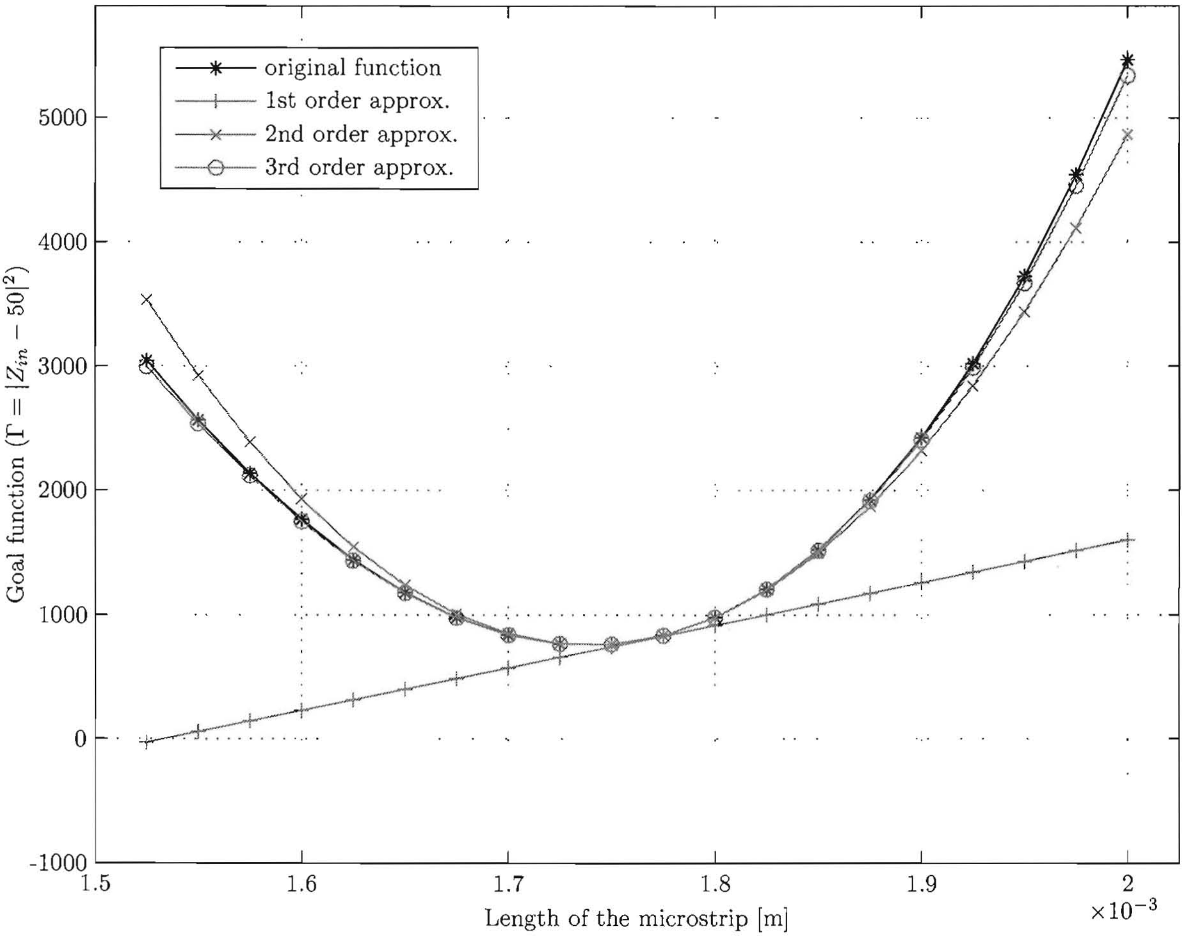

Figure 4.1: Original cost function and Taylor approximation of several orders

Chapter 5

Analysis of a canonical element

5.1 Introduction

The deflector element is studied by considering a canonical element, which is a simplified alternative for the final deflector element, presented in Chapter 6. The configuration of this canonical element is given in Section 5.2. The field solution is found in Section 5.3 and 5.4. Transmission of power is calculated for a typical element and results are given in Section 5.5. Because the amount of transmission is an important aspect of the deflector element, the element is optimised for maximum transmission of power at a frequency of 60 GHz in Section 5.6.

5.2 Configuration

Fig. 5.1 and Fig. 5.2 show the structure of the canonical element under analysis. It is based on the design described in [2], where an antenna consisting of a patch, two coupling slots and a reflector is discussed. This structure is chosen because the modelling can be performed with relative ease, yet it is able to act as a basic deflector element, i.e. to receive and emit power. The power is received on one side and coupled through the slots to the other side, where it is emitted. The received power is modelled as an incident plane wave at one side of the element. The element is a double back-to-back patch-on-grounded-dielectric-slab configuration, having a single ground plane at $z = 0$, which contains two slots. The width of an object is defined as its size in the y-direction and the length is defined as its size in the x-direction. The width of the patches is denoted by W_p and their length by L_p. The width of the slots is denoted by W_s, their length by L_s and the distance in the y-direction between the centre of the slots is denoted by D_s. The top patch at $z = h$ carries current density $\vec{J}_{p1}$ and the bottom patch at $z = -h$ carries current density $\vec{J}_{p2}$, which are both assumed to be y-directed. The electric field in the slots $\vec{E}_s$ is also assumed to be y-directed. The upper and lower dielectric slab, with permittivity ε_1, is assumed to extend to infinity in both the x and y-direction.

5.2.1 Source

The source field is a plane wave with y-polarised electric field, incident on top of the element. The plane wave is normal incident at $z = h$. The source field is described by

$$\begin{aligned} \vec{E}^{ex}(z) &= e^{jk_2(z-h)}\vec{u}_y, \\ \vec{H}^{ex}(z) &= \frac{1}{Z_2}e^{jk_2(z-h)}\vec{u}_x. \end{aligned} \tag{5.1}$$

As shown in App. D, the incident plane wave in medium 2 can be described by Eq. (D.1) and (D.2), with

$$E(z) = E_2(z)$$

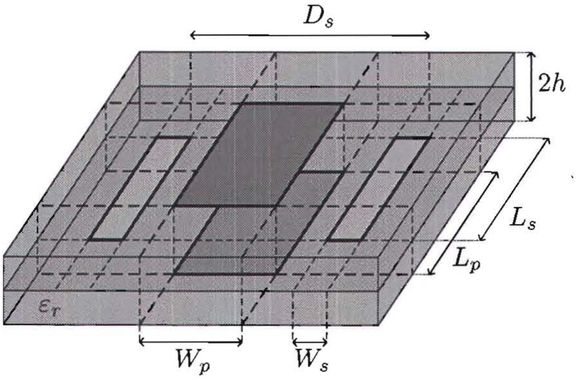

Figure 5.1: Configuration of the canonical element in 3D

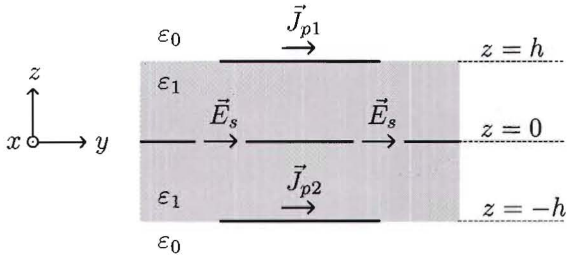

Figure 5.2: Front view of the canonical element

$$\begin{aligned} &= E_2^+(z) + E_2^-(z) \\ &= E_2^+ e^{-jk_2 z} + E_2^- e^{jk_2 z} \end{aligned} \tag{5.2}$$

and choosing

$$\begin{aligned} E_2^+ &= 0, \\ E_2^- &= e^{-jk_2 h}, \end{aligned} \tag{5.3}$$

which implies that $E_2(h) = E_2^-(h) = 1$.

5.3 Field analysis

The field solution is found by solving a similar problem, which is obtained from application of the *extinction theorem* [36]. This theorem is used to decompose all space into multiple regions, in which the fields can be described independently. These separate field descriptions are combined to the total field description by applying boundary conditions at the boundary between the separate regions. The final field solution is found by solving the boundary conditions using a Method of Moments approach.

5.3.1 Extinction theorem

Consider an imaginary closed surface S dividing all space in two regions V_0 and V_1, as shown in Fig. 5.3. Region V_0 contains electric and magnetic current sources $\vec{J}_0$ and $\vec{M}_0$, which produce fields $\vec{E}$ and $\vec{H}$ in both regions V_0 and V_1. By placing additional surface currents $\vec{J}_s = \vec{n}_0 \times \vec{H}$ and $\vec{M}_s = -\vec{n}_0 \times \vec{E}$ on the surface S, the fields inside region V_1 become $\vec{0}$. This is known as the extinction theorem.

5.3.2 Similar problem

To model the canonical deflector element in a convenient way, a similar problem is considered. In the similar problem, the slot layer is modelled with a finite thickness t_s. The reason for this choice will become clear shortly. The extinction theorem is applied to decompose all space in three regions V_1, V_2 and V_s, for which the fields can be described separately. This is depicted in Fig. 5.4, which shows a close-up of one of the slots. The field solution of the original problem is found by considering the solution of the similar problem in the limiting case that the slot thickness $t_s \to 0$ and by applying appropriate boundary conditions. Region V_1 is defined as all space above the slot layer, i.e. $z > t_s/2$, V_2 as all space below the slot layer, i.e. $z < -t_s/2$ and V_s as all space in the slot, for which $-t_s/2 < z < t_s/2$. At the boundary of V_1, surface currents $\vec{J}_{s1} = \vec{n}_1 \times \vec{H}$

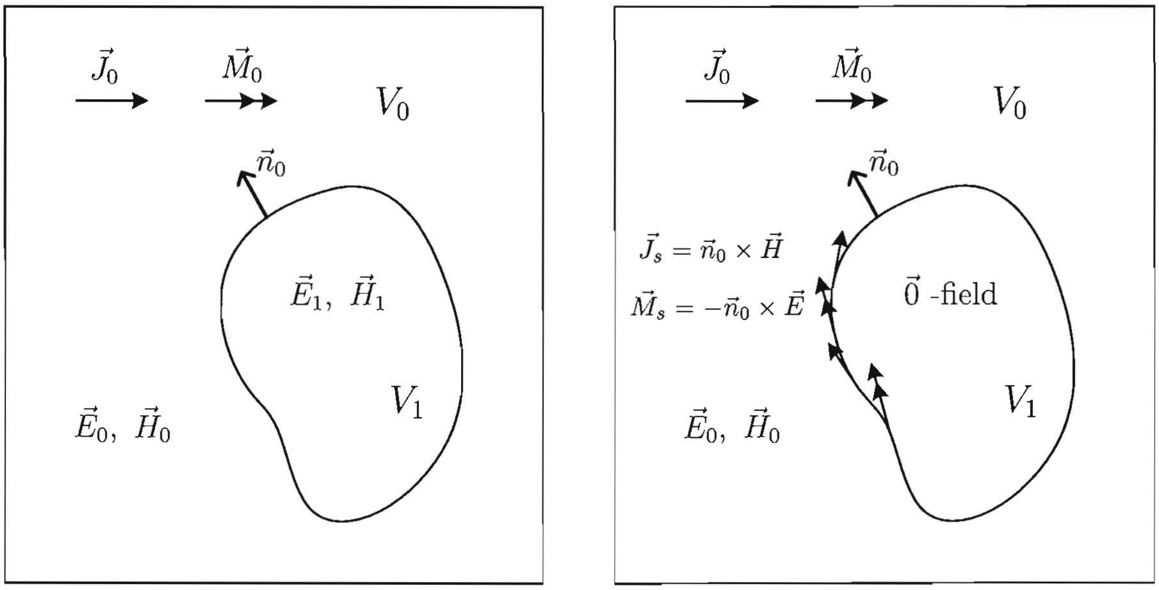

Figure 5.3: Extinction theorem; initial situation (left); $\vec{0}$-field in V_1 due to added surface currents (right)

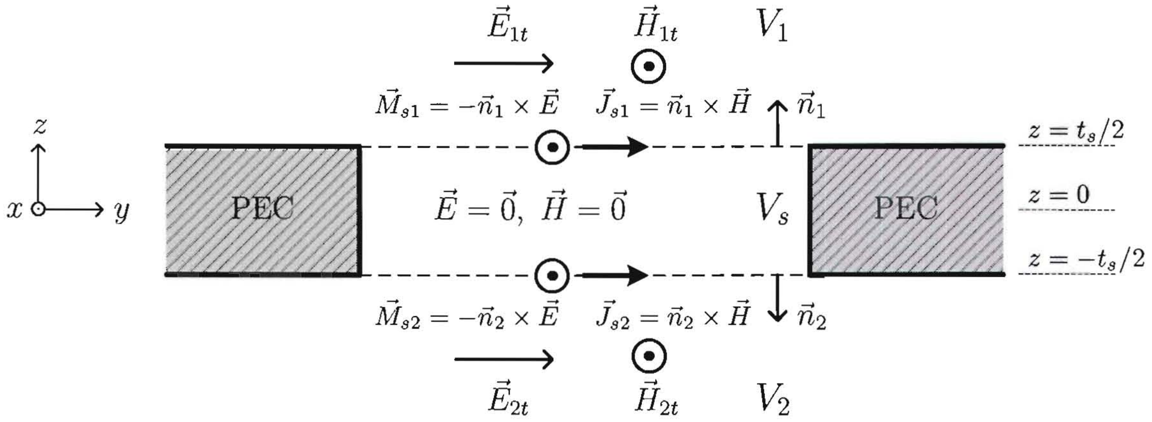

Figure 5.4: Space decomposition of the similar problem

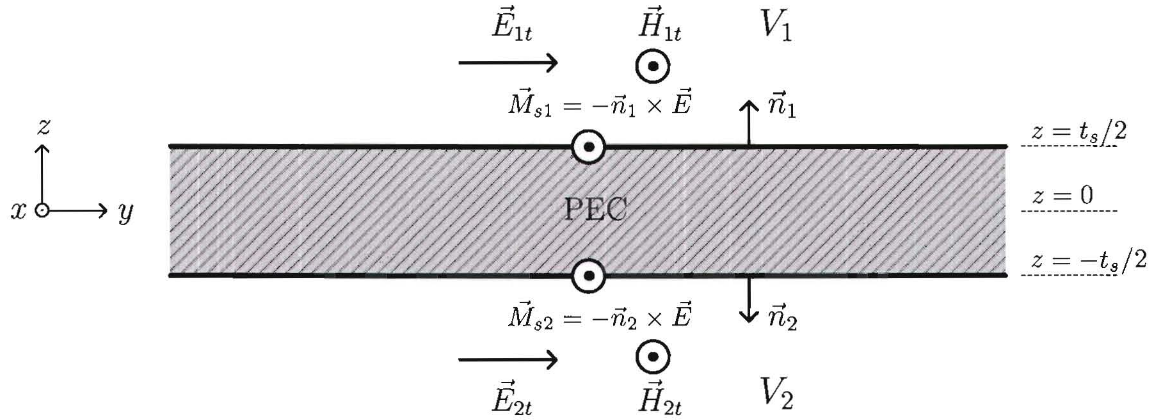

Figure 5.5: Similar problem configuration after replacing V_s with PEC and removing the non-radiating electric surface currents

and $\vec{M}_{s1} = -\vec{n}_1 \times \vec{E}$ are placed to null out the fields in V_s and V_2, but leaving fields inside V_1 intact. The same is done at the boundary of V_2, where surface currents $\vec{J}_{s2} = \vec{n}_2 \times \vec{H}$ and $\vec{M}_{s2} = -\vec{n}_2 \times \vec{E}$ are placed, to null out the fields in V_s and V_1, but leaving the fields in V_2 intact. By the superposition principle, adding these surface currents to both the boundaries of V_1 and V_2, the fields in V_1 and V_2 remain unchanged, while the fields in V_s become null.

The null field inside V_s allows us to replace V_s with PEC. This in turn allows for removing the non-radiating electric surface currents. The resulting configuration is shown in Fig. 5.5. In this configuration the fields in both V_1 and V_2 can be described separately, They are given by the field solution of the grounded dielectric slab. The original problem is obtained from the similar problem by considering the limiting case that the thickness of the slot layer goes to zero and V_s vanishes, so that the boundaries of V_1 and V_2 collide, and by applying the boundary conditions

$$\begin{aligned} \vec{E}_{1t} &= \vec{E}_{2t}, \\ \vec{H}_{1t} &= \vec{H}_{2t}, \end{aligned} \tag{5.4}$$

where $\vec{E}_{1t}$, $\vec{H}_{1t}$ denote the tangential fields at the boundary of V_1, just above the surface current sources, and $\vec{E}_{2t}$, $\vec{H}_{2t}$ the tangential fields at the boundary of V_2, just below the surface current sources. The final field solution is found by solving the boundary conditions for the slots (Eq. (5.4)) and the boundary conditions on the patches

$$\begin{aligned} \vec{n}_1 \times \vec{E} = 0 &\qquad \text{on patch 1,} \\ \vec{n}_2 \times \vec{E} = 0 &\qquad \text{on patch 2.} \end{aligned} \tag{5.5}$$

To solve these boundary conditions, the source fields must be taken into account. Specifically, the source magnetic field at $z = 0$ is required for the second boundary condition of Eq. (5.4) and the source electric field at $z = h$ is required for the boundary conditions of Eq. (5.5). Because in the similar problem, the condition $\vec{u}_z \times \vec{E}$ is satisfied in the entire $z = 0$ plane, the analysis in App. D is valid for region V_1. Therefore, the source electric field at $z = h$ and the source magnetic field at $z = 0$ in region V_1 are given by (Eq. (D.9) and (D.10), using $E_2^-(h) = 1$)

$$\begin{aligned} \vec{E}^{ex}(h) &= \frac{\tau_2(1 - e^{-2jk_1h})}{1 + \rho_1 e^{-2jk_1h}} \vec{u}_y, \\ \vec{H}^{ex}(0) &= \frac{-2\tau_2 e^{-jk_1h}}{Z_1(1 + \rho_1 e^{-2jk_1h})} \vec{u}_x, \end{aligned} \tag{5.6}$$

with the transmission and reflection coefficients (τ and ρ) given in App. D. The final field solution is found by solving the boundary conditions using a MoM approach. This solution is valid everywhere inside $V_1 \cup V_2$, the boundary excluded.

5.4 MoM approach

In order to find the field solution using MoM, the currents on the patch and in the slots should be modelled. The electric current on the patches is modelled using one entire domain basis function (an educated guess) $\vec{J}_p^{\,b}$, with transverse component $\vec{\Upsilon}_p^b(x,y)$, according to

$$\begin{aligned} \vec{J}_{p1}(\vec{r}) &= I_{e1}^b \vec{J}_p^{\,b}(\vec{r}) = I_{e1}^b \vec{\Upsilon}_p^b(x,y)\delta(z-h), \\ \vec{J}_{p2}(\vec{r}) &= I_{e2}^b \vec{J}_p^{\,b}(\vec{r}) = I_{e2}^b \vec{\Upsilon}_p^b(x,y)\delta(z+h). \end{aligned} \tag{5.7}$$

The magnetic current on the boundary of region V_1 and V_2 is modelled in a similar way, using basis function $\vec{M}_s^b$, with transverse component $\vec{\Psi}_s^b(x,y)$, according to

$$\begin{aligned} \vec{M}_{s1}(\vec{r}) &= I_{m1}^b \vec{M}_s^b(\vec{r}) = I_{m1}^b \vec{\Psi}_s^b(x,y)\delta(z), \\ \vec{M}_{s2}(\vec{r}) &= I_{m2}^b \vec{M}_s^b(\vec{r}) = I_{m2}^b \vec{\Psi}_s^b(x,y)\delta(z). \end{aligned} \tag{5.8}$$

The transverse components of the basis functions can be written as

$$\begin{aligned} \vec{\Upsilon}_p^b(x,y) &= \Pi(x/L_p)\Pi(y/W_p)\cos(\pi y/W_p)\vec{u}_y, \\ \vec{\Psi}_s^b(x,y) &= \Pi(y/W_s)\Pi(x/L_s)\cos(\pi x/L_s) * \left[\delta(y+D_s/2)+\delta(y-D_s/2)\right]\vec{u}_x, \end{aligned} \tag{5.9}$$

where '$*$' denotes convolution. In the spectral domain, this results in

$$\begin{aligned} \hat{\vec{\Upsilon}}_p^b(k_x,k_y) &= \frac{2\sin(k_x L_p/2)}{k_x}\frac{2\pi/W_p}{(\pi/W_p)^2-k_y^2}\cos(k_y W_p/2)\vec{u}_y, \\ \hat{\vec{\Psi}}_s^b(k_x,k_y) &= \frac{2\sin(k_y W_s/2)}{k_y}2\cos(k_y D_s/2)\frac{2\pi/L_s}{(\pi/L_s)^2-k_x^2}\cos(k_x L_s/2)\vec{u}_x. \end{aligned} \tag{5.10}$$

The first boundary condition of (5.4) can be solved by forcing

$$\vec{M}_{s2}(\vec{r}) = -\vec{M}_{s1}(\vec{r}) = \vec{M}_s(\vec{r}) = I_m^b \vec{M}_s^b(\vec{r}). \tag{5.11}$$

Using the spectral domain expressions for the scattered fields (Eq. (3.45), the equivalent expressions for a magnetic source current distribution, (Eq. (E.8)) and the spectral domain expressions for the source fields, i.e.

$$\begin{aligned} \hat{\vec{E}}^{ex}(k_x,k_y,h) &= \frac{\tau_2(1-e^{-2jk_1h})}{1+\rho_1 e^{-2jk_1h}}\vec{u}_y, \\ \hat{\vec{H}}^{ex}(k_x,k_y,0) &= \frac{-2\tau_2 e^{-jk_1h}}{Z_1(1+\rho_1 e^{-2jk_1h})}\vec{u}_x, \end{aligned} \tag{5.12}$$

in the remaining boundary conditions of (5.4) and (5.5) yield the spectral domain residues

$$\begin{aligned} \hat{\vec{R}}_{p1}(k_x,k_y,h) &= \hat{\vec{E}}^{ex}(k_x,k_y,h) + \\ &\quad I_{e1}^b \hat{\bar{\bar{Q}}}_{EJ}(k_x,k_y,h)\hat{\vec{\Upsilon}}_p^b(k_x,k_y) + I_m^b \hat{\bar{\bar{Q}}}_{EM}(k_x,k_y,h)\hat{\vec{\Psi}}_s^b(k_x,k_y), \\ \hat{\vec{R}}_{p2}(k_x,k_y,-h) &= I_{e2}^b \hat{\bar{\bar{Q}}}_{EJ}(k_x,k_y,h)\hat{\vec{\Upsilon}}_p^b(k_x,k_y) + I_m^b \hat{\bar{\bar{Q}}}_{EM}(k_x,k_y,h)\hat{\vec{\Psi}}_s^b(k_x,k_y), \\ \hat{\vec{R}}_s(k_x,k_y,0) &= \hat{\vec{H}}^{ex}(k_x,k_y,0) + I_{e1}^b \hat{\bar{\bar{Q}}}_{HJ}(k_x,k_y,0)\hat{\vec{\Upsilon}}_p^b(k_x,k_y) + \\ &\quad 2I_m^b \hat{\bar{\bar{Q}}}_{HM}(k_x,k_y,0)\hat{\vec{\Psi}}_s^b(k_x,k_y) + I_{e2}^b \hat{\bar{\bar{Q}}}_{HJ}(k_x,k_y,0)\hat{\vec{\Upsilon}}_p^b(k_x,k_y), \end{aligned} \tag{5.13}$$

where the required components of the Green's functions $\hat{\bar{\bar{Q}}}_{EJ}(k_x,k_y,h)$, $\hat{\bar{\bar{Q}}}_{EM}(k_x,k_y,h)$, $\hat{\bar{\bar{Q}}}_{HJ}(k_x,k_y,0)$ and $\hat{\bar{\bar{Q}}}_{HJ}(k_x,k_y,0)$ are given in App. E. Weighing the residues to zero with basis functions $\vec{J}_p^{\,b}$ and $\vec{M}_s^b$ in the spatial domain, which means evaluating integrals of the form

$$\int_{V_0} \vec{R}_{p1}(\vec{r}_0)\vec{J}_{p1}(\vec{r}_0)\, dV_0 = 0, \tag{5.14}$$

results in the MoM spatial domain matrix equation

$$[V] + [Z][I] = 0, \tag{5.15}$$

with

$$[I] = [I^b_{e1} \quad I^b_{e2} \quad I^b_m]^T, \tag{5.16}$$

and $[V]$ and $[Z]$ in the spectral domain having the form

$$\begin{aligned} [\hat{V}] &= \begin{bmatrix} \hat{\Upsilon}^{b*}_{p,y}\hat{E}^{ex}_y & 0 & \hat{\Psi}^{b*}_{s,x}\hat{H}^{ex}_x \end{bmatrix}^T, & (5.17) \\ [\hat{Z}] &= \begin{bmatrix} \hat{\Upsilon}^{b*}_{p,y}\hat{Q}_{EJyy}\hat{\Upsilon}^b_{p,y} & 0 & \hat{\Upsilon}^{b*}_{p,y}\hat{Q}_{EMyx}\hat{\Psi}^b_{s,x} \\ 0 & \hat{\Upsilon}^{b*}_{p,y}\hat{Q}_{EJyy}\hat{\Upsilon}^b_{p,y} & \hat{\Upsilon}^{b*}_{p,y}\hat{Q}_{EMyx}\hat{\Psi}^b_{s,x} \\ \hat{\Psi}^{b*}_{s,x}\hat{Q}_{HJxy}\hat{\Upsilon}^b_{p,y} & \hat{\Psi}^{b*}_{s,x}\hat{Q}_{HJxy}\hat{\Upsilon}^b_{p,y} & 2\hat{\Psi}^{b*}_{p,x}\hat{Q}_{HMxx}\hat{\Psi}^b_{p,x} \end{bmatrix}, & (5.18) \end{aligned}$$

where the subscript 'x' or 'y' denotes the respective cartesian component and the superscript '$*$' denotes the complex conjugate. To solve Eq. (5.15) for the unknown current coefficient vector $[I]$, the elements of $[V]$ and $[Z]$ have to be evaluated in the spatial domain, by performing the inverse Fourier transform on each element. For example, for Z_{11} this becomes:

$$Z_{11} = \frac{1}{4\pi^2}\int_{k_x}\int_{k_y} \hat{\Upsilon}^{b*}_{p,y}(k_x, k_y)\hat{Q}_{EJyy}(k_x, k_y, h)\hat{\Upsilon}^b_{p,y}(k_x, k_y)\; dk_x dk_y, \tag{5.19}$$

which is evaluated, as explained in Section 3.3.6, by a coordinate transformation from (k_x, k_y) to (k_ρ, ψ). The resulting integral is solved numerically, where the integration over k_ρ is performed up to a certain finite K_ρ.

5.5 Transmitted power for a typical element

As a measure for the transmitted power, the time average radiated power towards the broadside direction at the downside of the element is used. For convenience, we define a new coordinate system, with cartesian coordinates $(x', y', z') = (-x, -y, -z)$ and spherical coordinates $(r', \theta', \phi') = (r, \theta + \pi, \phi + \pi)$, in which the broadside direction at the downside of the element can be expressed as the direction $(\theta' = 0, \phi' = 0)$. The time average radiated power P_{rad} towards direction (θ', ϕ') is given by (Eq. (B.1))

$$P_{rad}(\theta', \phi') = \frac{|\vec{E}(r', \theta', \phi')|^2 r'^2}{2Z_0}. \tag{5.20}$$

in which $\vec{E}(r', \theta', \phi')$ can be expressed in terms of its spectral domain representation, according to Eq. (3.51) as

$$\vec{E}(r', \theta', \phi') = \frac{jk_0 e^{-jk_0 r'}}{2\pi r'} e^{jk_0 h\cos\theta'} \vec{u}_{r'} \times \left(\hat{\vec{E}}(k_{x'}, k_{y'}, h) \times \vec{u}_{r'}\right), \tag{5.21}$$

with $k_{x'} = k_0 \sin(\theta')\cos(\phi')$ and $k_{y'} = k_0 \sin(\theta')\sin(\phi')$. Combining Eq. (5.20) and Eq. (5.21) and using $\hat{E}_{x'} = 0$, we obtain for broadside direction

$$P_{rad}(0, 0) = \frac{k_0^2}{8\pi^2 Z_0}\left|\hat{E}_{y'}(0, 0, h)\right|^2, \tag{5.22}$$

which, in the original coordinate system, becomes

$$P_{rad}(\pi, 0) = \frac{k_0^2}{8\pi^2 Z_0}\left|\hat{E}_y(0, 0, -h)\right|^2, \tag{5.23}$$

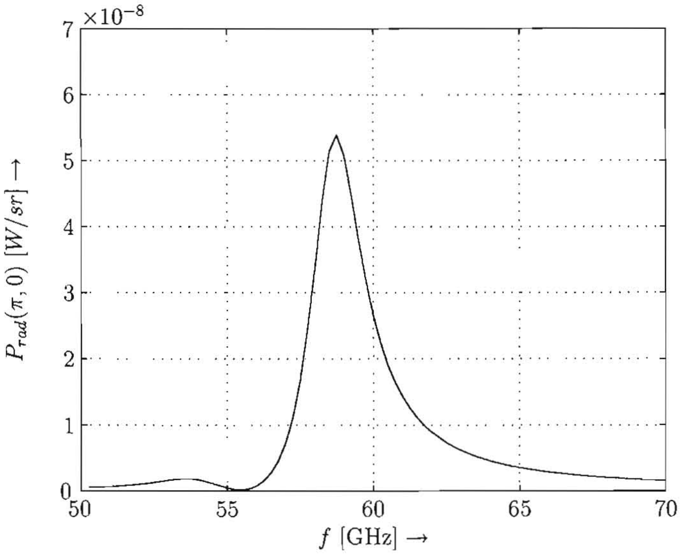

Figure 5.6: Transmitted power for the typical deflector element

where $\hat{E}_{y'} = -\hat{E}_y$ is used. The electric field in the spectral domain is evaluated in region V_2, at $z = -h$. It is given by

$$\hat{E}_y(k_x, k_y, -h) = I^b_{e2}\hat{Q}^{EJ}_{yy}(k_x, k_y, h)\hat{\Upsilon}^b_{p,y}(k_x, k_y) + I^b_m\hat{Q}^{EM}_{yx}(k_x, k_y, h)\hat{\Psi}^b_{s,x}(k_x, k_y). \tag{5.24}$$

Transmitted power is calculated in the frequency range from 50 to 70 GHz for a typical element, with parameters

$$\begin{aligned} W_p &= 1.7 \text{ mm} & D_s &= 2.5 \text{ mm}, \\ L_p &= 1.7 \text{ mm} & h &= 0.254 \text{ mm}, \\ W_s &= 0.23 \text{ mm} & \varepsilon_{r1} &= 2.17, \\ L_s &= 1.7 \text{ mm} & \varepsilon_{r2} &= 1. \end{aligned} \tag{5.25}$$

The result is shown in Fig. 5.6. Simulations show that good performance is obtained if the width of the patch (W_p) and the length of the slots (L_s) are equal to half a wavelength in the substrate at $f = 60$ GHz. The length of the patch (L_p) and the width of the slots (W_s) are not so critical.

5.6 Optimisation

The element from Section 5.5 is optimised for maximum transmission of RF power at $f = 60$ GHz, by varying the slot spacing D_s, using the method described in Chapter 4.

5.6.1 Cost function and derivatives

To maximise the transmitted power, given by Eq. (5.23), we define the cost function

$$\Gamma(D_s) = \frac{k_0^2}{8\pi^2 Z_0} |f(D_s)|^2, \tag{5.26}$$

with

$$f(D_s) = \hat{E}_y(0, 0, -h, D_s), \tag{5.27}$$

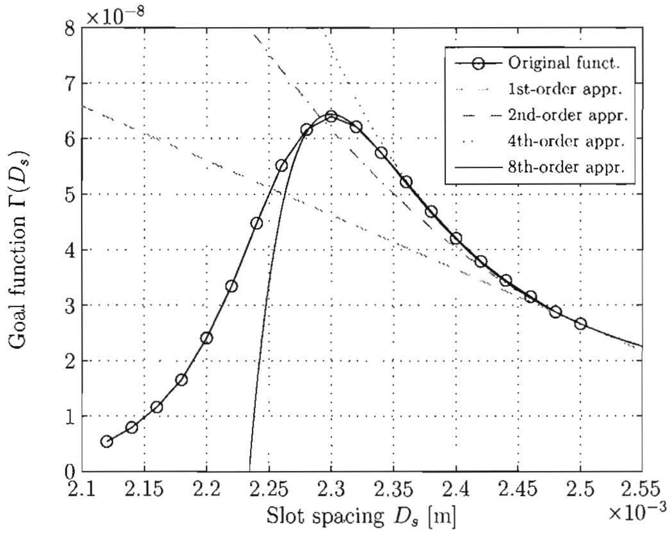

Figure 5.7: Taylor approximation of the cost function; cost function (-⊖-), 1^{st}-order approximation (−−), 2^{nd}-order approximation (− ·), 4^{th}-order approximation (· ·) and 8^{th}-order approximation (−)

where the dependence of $\hat{E}_y$ on D_s is written explicitly. The n^{th}-order derivative of f to D_s is given by

$$\nabla^n f(D_s) = \nabla^n \hat{E}_y(0,0,-h,D_s), \tag{5.28}$$

which, using the product rule, can be written as an expression involving the terms $\nabla^k[I]$, $\nabla^k \hat{Q}^{EJ}_{yy}$, $\nabla^k \hat{\Upsilon}^b_{p,y}$, $\nabla^k \hat{Q}^{EM}_{yx}$ and $\nabla^k \hat{\Psi}^b_{s,x}$, with $k = 0, \ldots, n$. These terms can all be evaluated in a straightforward manner, except for $\nabla^k[I]$, which is evaluated according to

$$\begin{aligned}\nabla^k[I] &= \nabla^{k-1}\left[\nabla\left\{-[Z]^{-1}[V]\right\}\right]\\ &= \nabla^{k-1}\left[-[Z]^{-1}(\nabla[V]) + [Z]^{-1}(\nabla[Z])[Z]^{-1}[V]\right],\end{aligned} \tag{5.29}$$

where $\nabla([Z]^{-1}) = -[Z]^{-1}(\nabla[Z])[Z]^{-1}$ is used. The evaluation of (5.29) continues in a similar manner, by using the product rule. The resulting expression consists of $[Z]^{-1}$ and $\nabla^k[Z]$ terms, which are evaluated in an element-wise manner.

5.6.2 Results

As mentioned, the optimisation method is applied to the typical deflector element from Section 5.5, with the same initial parameters. The cost function is approximated by a Taylor expansion around $D_s = 2.5$ mm, which results in Fig. 5.7. The 8^{th}-order approximation is sufficient to find the optimal slot spacing, which is $D_s = 2.3$ mm. Fig. 5.8 shows the transmitted power in the frequency range from 50 to 70 GHz for the optimised element. It is clear that this design is optimised for maximum transmission at $f = 60$ GHz.

5.7 Conclusion

The modelling of a canonical element has been considered. The structure of the element has been given and the source field has been modelled as a plane wave. The field solution has been found in a number of a steps. First, the problem has been simplified by decomposing the solution domain

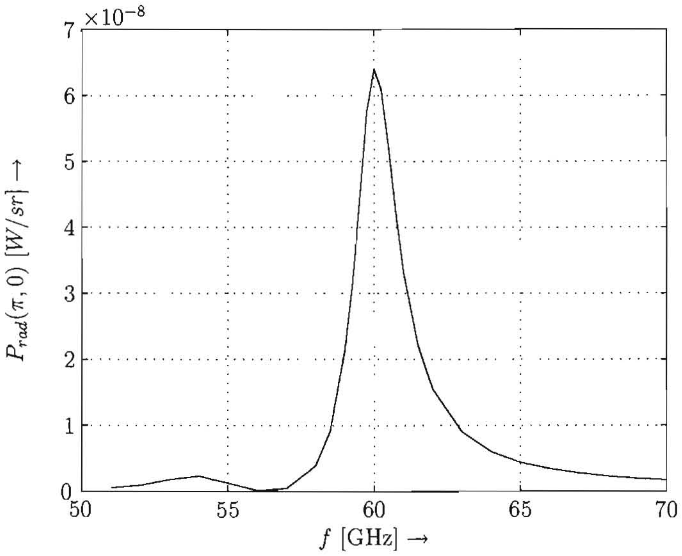

Figure 5.8: Transmitted power for the optimised deflector element

into multiple sub domains, using the extinction theorem. Next, the field description in both sub domains has been found to be equivalent to the closed-form field solution of the grounded dielectric slab, as presented in Chapter 3. The total field description has been obtained by applying proper boundary conditions at the interface between the sub domains. The final field solution has been obtained by solving the boundary conditions using a Method of Moments approach. Using this field solution, transmitted power for a typical element has been calculated in the frequency range of 50 - 70 GHz. Finally, the canonical element has been optimised for maximum transmitted power at 60 GHz, using the optimisation method presented in Chapter 4.

Chapter 6

Realisation of a deflector

6.1 Introduction

A deflector is designed which deflects an EM wave by an angle of about 30 degrees. As mentioned before, the deflector consists of elements, which apply a varying phase shift. The phase shifting property of the element can be realised in a number of ways. This is explained in Section 6.2. The design of a 9x5-element deflector is given in Section 6.3. The simulation results are given in Section 6.4.

6.2 Phase-shifting deflector element

The canonical deflector element, optimised for transmission in Section 5.6, is used as starting point for the design of the phase-shifting deflector element. An important design criterion is that a phase shift in the full range of 0 to 360 degrees can be applied, while retaining good transmission properties. The phase shifting property of the element can be realised by varying the size of the patches, as explained in Section 6.2.1. Alternatively, it can be realised by adding transmission lines with varying length. This is explained in Section 6.2.2.

6.2.1 Variable patch size

A variable phase shift of the transmitted wave can be realised by varying the size of the patches. This idea is based on the design described in [41], where it is successfully applied in a reflectarray [7]. In this design, the presence of a ground plane ensures full reflection of the incident wave. This is not the case with the deflector element, where the wave is coupled through slots in the ground plane to the other side of the element. The transmission coefficient varies considerably with the size of the patches, not allowing for a practical design. In [14], multiple patches are used to obtain more degrees of freedom in the design. Applying this idea to the design of the deflector element yields a patch-patch-slot-patch configuration, which is shown in Fig. 6.1. With this configuration it is possible to obtain better transmission properties than in the patch-slot-patch configuration of the canonical element. Still, it is hard to obtain a design where phase shift over the full range is possible, while retaining good transmission properties over a sufficiently large frequency band. A major problem of using variable size patches to obtain an appropriate phase shift, is that the phase shift and the transmission coefficient of an element can not be controlled independently. A consequence of this dependence is that the magnitude of the transmission coefficient decreases near the edges of the phase shift range. The modulus of the transmission coefficient of the element after optimisation is shown in Fig. 6.2, for varying phase shift and frequency. Reasonable transmission properties over the full phase range are only obtained for frequencies between 58 GHz and 61 GHz, so the principle of varying patch size can not be applied successfully in the design of the deflector element.

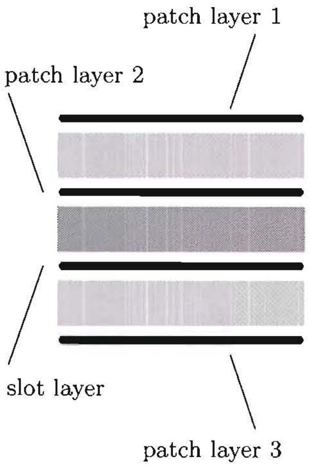

Figure 6.1: Patch-patch-slot-patch configuration

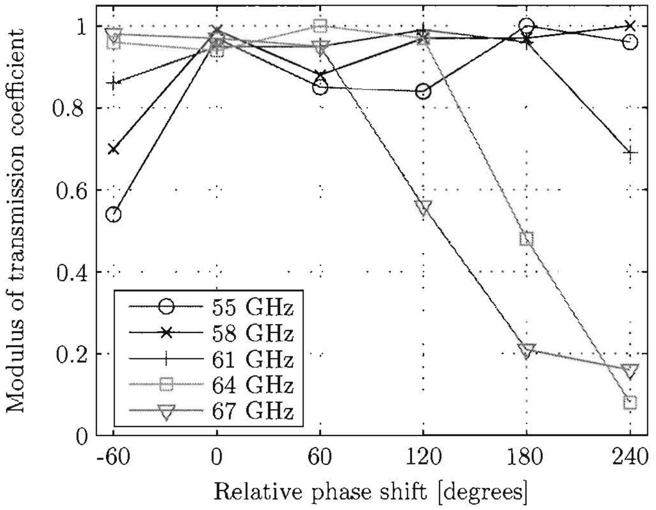

Figure 6.2: Transmission properties of the patch-patch-slot-patch configuration

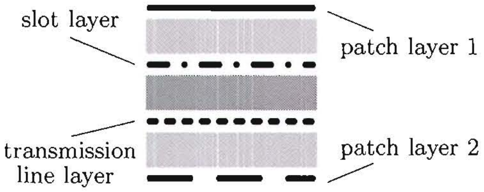

Figure 6.3: Stack of the deflector element

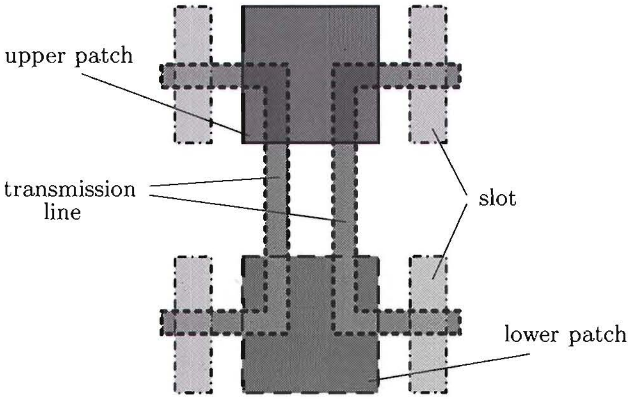

Figure 6.4: Initial design of the deflector element

6.2.2 Transmission lines

Independent control over transmission and phase shift can be obtained by using transmission lines of varying length to provide the phase shifting property. In the canonical element, power from the downside is coupled directly to the upside through a pair of slots. In this design, power from the downside is coupled to a pair of transmission lines, which carry the power to a second pair of slots. These slots couple the power to the upside of the element. The transmission lines introduce a time delay, which is independent of frequency. The amount of delay is determined by the length of the transmission lines. The design can be realised in a stack with four metal layers, as shown in Fig. 6.3. The initial design, clearly showing the principle described above, is shown in Fig. 6.4. To obtain a compact design, the patch and slots on the downside can be rotated by 90 degrees and placed underneath the patch on the upside. This is shown in Fig. 6.5. A problem in the design of Fig. 6.5 is that both pairs of slots emit undesired spurious radiation, towards both the receiving and emitting side of the element. This problem can be solved by extending the length of both patches, so that they shield off the spurious radiation. This does not influence the transmission properties. The final design is shown in Fig. 6.6. The initial element parameters have been found by the optimisation method described in Section 5.6. The complete

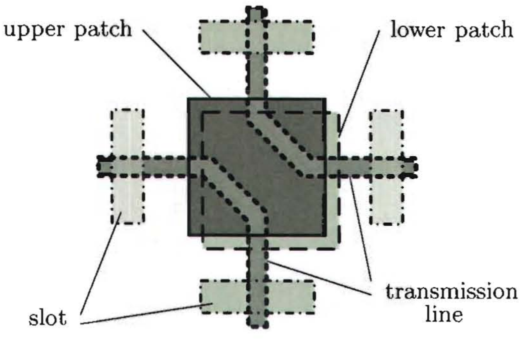

Figure 6.5: Compact design of the deflector element

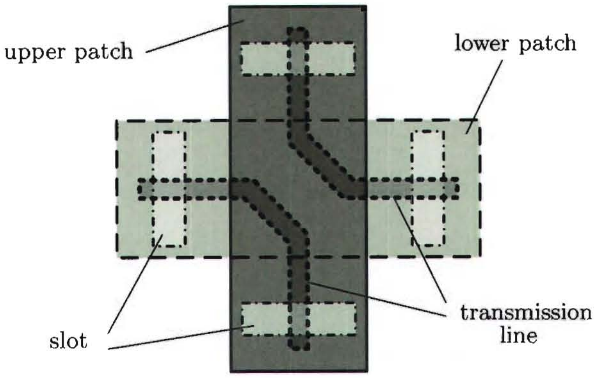

Figure 6.6: Final design of the deflector element

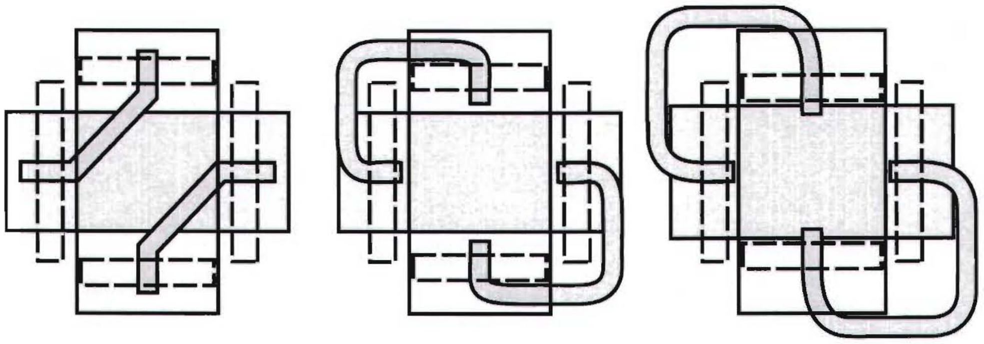

Figure 6.7: Deflector elements; −120 degrees (left), 0 degrees (middle) and 120 degrees (right)

structure, including transmission lines can be modelled and optimised as well with this approach, but this is too involved for now. The structure is modelled with CST Microwave Studio, a full-wave EM simulator. Three different elements incorporating transmission lines are designed, which realise a phase shift of -120, 0 and 120 degrees at a frequency of 60 GHz, respectively. These elements are shown in Fig. 6.7. The size of the elements is 3.2mm × 3.0mm, which corresponds to $0.64\lambda \times 0.60\lambda$ at 60 GHz. Simulations show that the element has good transmission properties for frequencies between 57 GHz and 63 GHz, which is a 10% bandwidth within the 60 GHz band. So the principle of transmission lines with varying length to obtain an appropriate phase shift can be applied successfully in the design of the deflector element.

6.3 Design of the deflector

A 9×5-element deflector has been designed by placing multiple deflector elements in a regular pattern. The three elements shown in Fig. 6.7 are placed in an alternating order along one direction. Along the other direction, the elements are identical. The deflector is simulated with plane wave excitation. The simulation program is not able to calculate a radiation pattern, if the structure is excited with a perfect plane wave. Therefore, four horn antennas are used next to each other to generate an approximated plane wave. By inspecting Eq. (2.1), it is clear that an incident EM wave of 60 GHz is deflected by 34 degrees, if the element spacing is equal to 3.2 mm. Because the transmission lines actually introduce a fixed time delay rather than a phase delay, the angle towards which power is deflected is independent of frequency. This is verified by the simulation results in the next section.

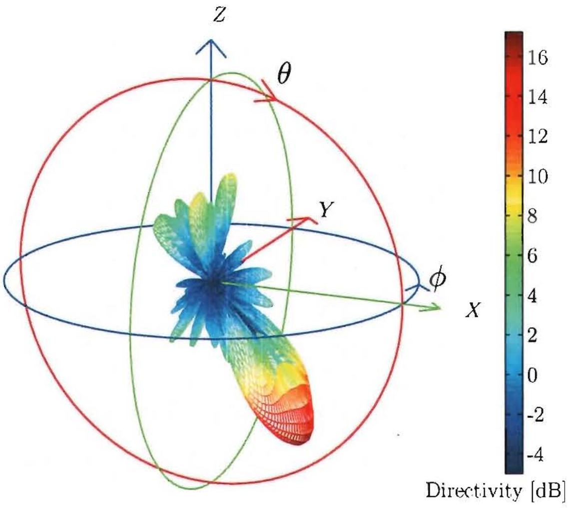

Figure 6.8: Radiation pattern (3D); $f = 60$ GHz

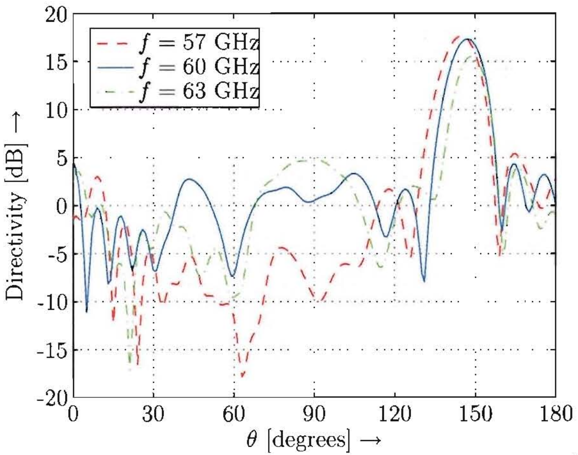

Figure 6.9: Radiation pattern (θ-cut, $\phi = 0$ deg); $f = 57$ GHz (−−), $f = 60$ GHz (−) and $f = 63$ GHz (− ·)

6.4 Simulation results

Fig. 6.8 and 6.9 show the resulting radiation patterns of the 9×5-element deflector for varying frequency, when an approximated wave is incident from $\theta = 0$ degrees. The wave is deflected by 34 degrees, towards $\theta = 146$ degrees, independent of frequency. For $f = 60$ GHz, the -10 dB main lobe width is 21 degrees. Side lobes are 12.4 dB lower than the main lobe. The directivity is 17.3 dBi. For $f = 57$ GHz and $f = 63$ GHz, the results are slightly different, but comparable. These results clearly show the wideband behaviour of the deflector.

6.5 Conclusion

The optimised canonical deflector element has been used as starting point for the design of the phase-shifting deflector element. The phase shifting property can be realised in two ways. It has been shown that the principle of varying patch size is not a suitable option, because reasonable transmission properties can only be obtained for the frequency range of 58 - 61 GHz. By using transmission lines to realise the phase shifting property, good transmission properties have been obtained for the frequency range of 57 - 63 GHz. Phase-shifting elements have been designed, using transmission lines, which realise a relative phase shift of -120, 0 and 120 degrees. Simulations show that a deflector, consisting of these elements placed in a regular pattern, is able to deflect an incoming EM wave by 34 degrees over the entire frequency band of 57 - 63 GHz. The resulting directivity at 60 GHz is 17.3 dBi and side lobes are 12.4 dB lower than the main lobe.

Chapter 7

Measurement and simulation results

7.1 Introduction

To verify the performance of the deflector, two 9 × 9-element deflectors are constructed, which we call deflector A and deflector B for convenience. The construction of the deflectors is discussed in Section 7.2 and the measurement setup is discussed in Section 7.3. In Section 7.4, the measurement results are given and compared to simulations.

7.2 Construction of the deflectors

Deflector A is constructed in the same way as the 9×5-element deflector of Chapter 6 and therefore deflects incident waves by 34 degrees. Deflector B is constructed out of identical elements, for which the middle element in Fig. 6.7 is used. This deflector does not change the phase distribution of the incident wave and therefore the outgoing wave propagates in the same direction. Both deflectors are realised in printed circuit board technique. The stack consists of four metal layers with dielectric material in between, as shown in Fig. 6.3. The upper and lower dielectric have a thickness of 0.254 mm and a relative permittivity of 2.17. The middle dielectric has a thickness of 0.112 mm and a relative permittivity of 2.6. The dimensions of both deflectors are 28.8 mm × 27.0 mm.

7.3 Measurement setup

The measurement setup is shown in Fig. 7.1. The deflectors are excited by a conical horn. The radius of the horn aperture is 11.0 mm. A HP/Agilent E8361A PNA Network Analyzer is used for S-parameter measurement up to a frequency of 67 GHz. To measure the radiation pattern, a custom-made measurement setup is used, able to measure the far field radiation pattern of the deflectors [3]. Averaging is used to limit the influence of noise and time gating is applied to remove the influence of reflections from the environment. Due to space limitations of the measurement setup, the horn is placed 13 mm away from the deflector. The deflector is therefore not in the far field region of the horn. Absorbing material is placed around the deflector to prevent spurious radiation from the horn from passing the deflector at the sides and thereby disturbing the radiation pattern of the deflector. The conical horn is connected to the network analyser by a coaxial cable, a coax-to-waveguide adapter, a rectangular-to-circular waveguide adapter and a piece of curved circular waveguide. To measure the radiation pattern, an open-ended waveguide is used, connected to the network analyser with the same type of coaxial cable and coax-to-waveguide adapter. We are interested in the gain of the conical horn together with the deflector.

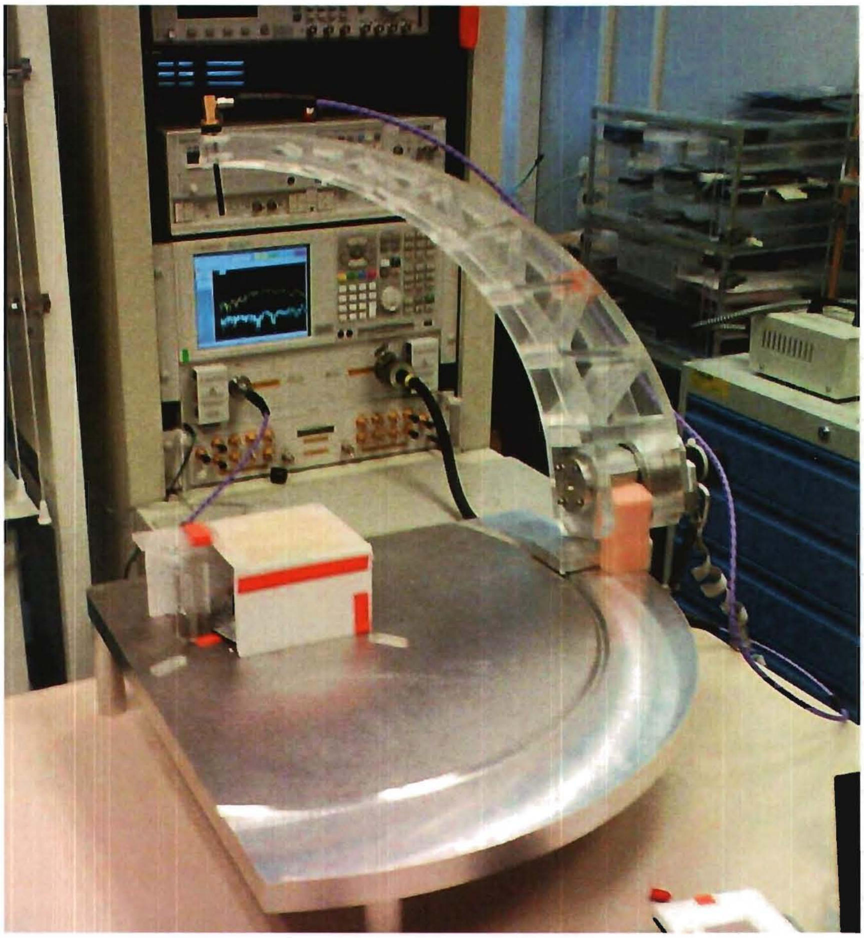

Figure 7.1: Measurement setup; conical horn not shown

7.3.1 Calibration

In order to remove the effects of the coaxial cables, adapters and the open-ended waveguide, two calibration measurements have been performed. In the first measurement, the S-parameters of the coaxial cables together with the adapters are measured. The adapters are connected back-to-back. It is assumed that all components are perfectly matched. This way the gain, or $|S_{12}|^2$, of one coaxial cable and adapter can be calculated. In the next measurement, an S-parameter measurement is performed of two open-ended waveguides, placed opposite to each other in the far field region. Friis equation is used to remove the effect of free space loss and the result of the first measurement is used to calculate the gain of the open-ended waveguides. The gain of the open-ended waveguide and the cables together with the adapter can be used to calculate the gain of the conical horn together with the deflector. The rectangular-to-circular waveguide adapter and the piece of curved circular waveguide are assumed to be lossless in this calculation.

7.4 Results

Fig. 7.2 and 7.3 show the gain as function of elevation angle θ for both deflectors in the deflecting plane at a frequency of 60 GHz. Deflector A has a clear peak at 34 degrees and Deflector B has a clear peak at 0 degrees, as expected. Sidelobe levels are in the order of -10 dB. Fig. 7.4 shows the results after normalisation. Good agreement between measured and simulated results is obtained

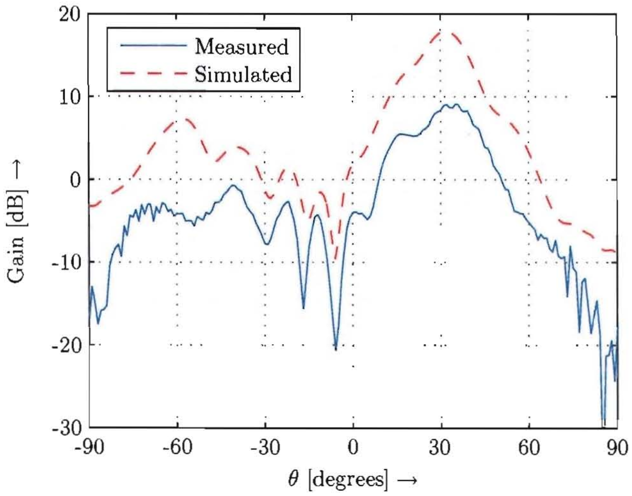

Figure 7.2: Gain of deflector A (deflecting plane, $f = 60$ GHz); measured (—); simulated (– –)

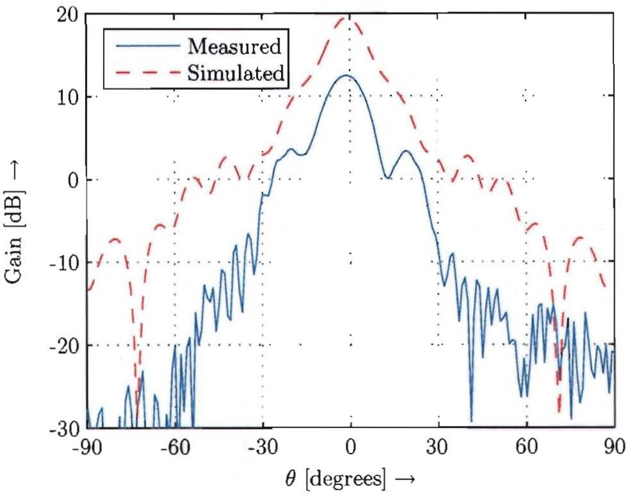

Figure 7.3: Gain of deflector B (deflecting plane, $f = 60$ GHz); measured (—); simulated (– –)

for both deflectors. Fig. 7.5 shows the normalised gain for both deflectors as function of frequency, measured at their peaks of $\theta = 0$ and $\theta = 34$ degrees. Deflector A, the 34-degrees deflector, shows best performance for a frequency of 59 GHz and 62 GHz and deflector B, the 0-degrees deflector, shows best performance for a frequency of 56 GHz and 62 GHz. The transmission of deflector B as function of frequency is slightly better than that of deflector A.

7.5 Discussion

Simulated results show a gain of 18-20 dB and measured results show a gain of 10-15 dB, which is a large difference. There are a number of reasons that can explain these differences.

- The absorbing material around the deflector has not been included in the simulations. This may account for some differences at angles further from the main beam angle.
- The rectangular-to-circular waveguide adapter and the piece of curved circular waveguide are assumed to be lossless, but these components might introduce a few dB loss.
- During calibration, we calculated the gain of the open-ended waveguide and found a value of 1 (0 dB). This value should be higher. Probably, some parts of the calibration procedure need more attention. This could explain part of the difference.

7.6 Conclusion

Two 9×9-element deflectors have been constructed. One deflector deflects incident waves by 34 degrees, the other deflector does not change the direction of incident waves. The measurement setup has been described and the calibration procedure has been explained. Measured and simulated results of both deflectors have been given. Good agreement exists between normalised measurement and simulation results. Both deflectors behave as expected, sidelobe levels are in the order of -10 dB. The transmission of the 0-degrees deflector as function of frequency is slightly better than that of the 34-degrees deflector. Quite some differences in gain exist between simulated and measured results. Several reasons have been given to explain these differences.

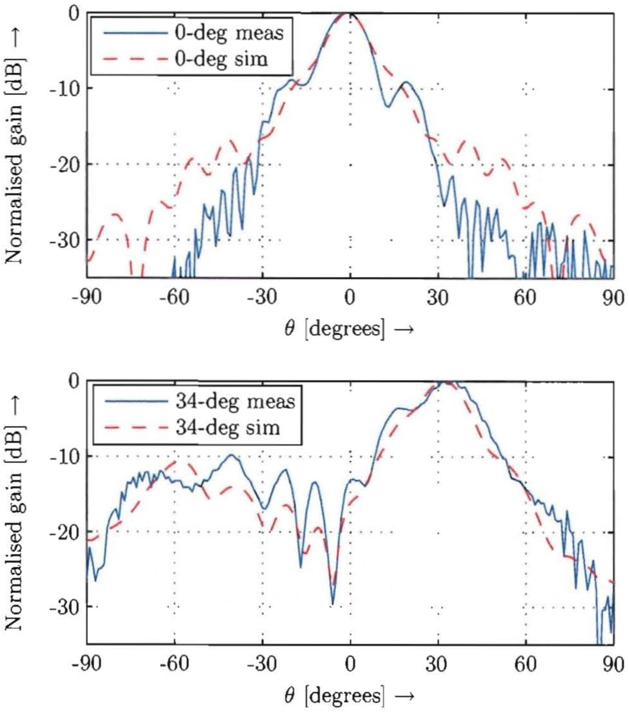

Figure 7.4: Normalised gain of both deflectors; measured (—); simulated (– –)

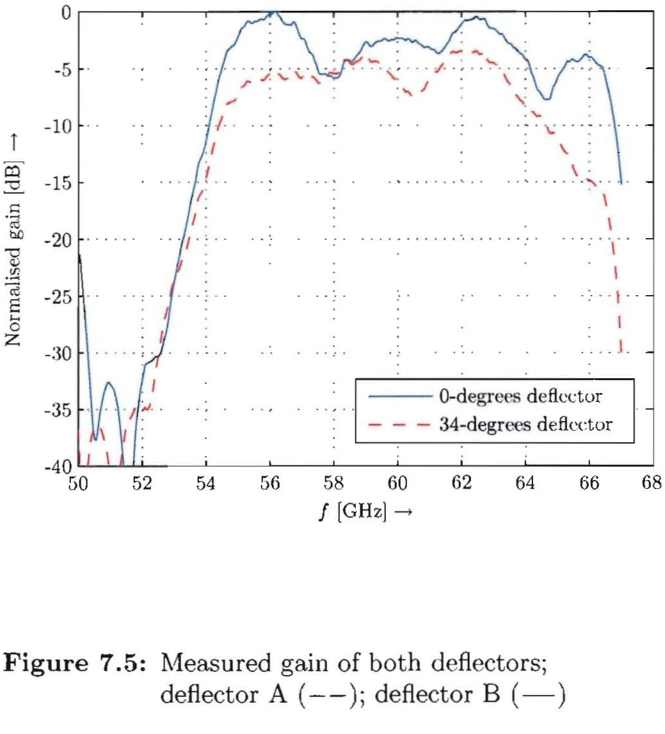

Figure 7.5: Measured gain of both deflectors; deflector A (– –); deflector B (—)

Chapter 8

Conclusions and recommendations

A summary and conclusions of the work are given in Section 8.1. Recommendations for further research are given in Section 8.2.

8.1 Conclusions

Wireless communication in the licence-free 60 GHz band requires a high gain, highly steerable antenna configuration. The coverage of a single antenna array is limited. A deflector-based design has been proposed to extend coverage. The proposed design consists of a steerable source and multiple deflectors. Advantages of this design are its simplicity and low cost.

In order to extend coverage, the deflectors should be designed to achieve a suitable centre steering angle and steerability. In Chapter 2, it has been investigated how the deflector should be designed in order to achieve a desired steerability. It has been explained that the phase distribution on the upside determines the deflecting behaviour and that a trade-off exists between directivity and steerability. This has been clarified by defining two scenarios. The behaviour of the deflector together with a source has been modelled and simulation results have been given for deflector designs that are suitable for those scenarios. These simulation results confirm the trade-off. Coverage can be extended to angles that can not be reached by the source itself, but in order to obtain beams with high directivity, the desired steerability should not be too large.

The desired phase distribution on the upside of the deflector is achieved by multiple phase-shifting elements, which change the phase distribution of the incident wave on the downside. An important aspect of the deflector element is its transmission of power. This should be as large as possible for the frequency band of interest. In order to gain insight into the behaviour of the deflector element, a simplified version of the final element has been studied in Chapter 5. The field solution of this canonical element has been found in a number of steps. First, the solution domain is decomposed into multiple sub domains by using the extinction theorem. Next, the field description in both sub domains has been found to be equivalent to the closed-form field solution of the grounded dielectric slab, as presented in Chapter 3. The total field description has been obtained by applying proper boundary conditions at the interface between the sub domains. The final field solution has been obtained by solving the boundary conditions using a Method of Moments approach. This field solution has been used to calculate transmitted power for an element with typical parameters in the frequency range of 50 - 70 GHz.

In Chapter 4, an optimisation method has been presented, which can be used to find a global optimum of a custom property. The property of interest is represented by a cost function. By approximating the cost function in closed-form by means of a Taylor expansion, finding a global optimum is straightforward, if one optimization parameter is considered. Finding the Taylor approximation is the challenging part of the method. This optimisation method has been used to optimise the canonical element for maximum transmitted power at 60 GHz.

In Chapter 6, the canonical deflector element is used as starting point for the design of a phase-shifting deflector element. The phase shifting property of the deflector element can be realised in a number of ways. It has been shown that the principle of varying patch size is not a suitable option, because reasonable transmission properties can only be obtained for the frequency range of 58 - 61 GHz. By using transmission lines to realise the phase shifting property, good transmission properties have been obtained over a frequency band of 57 - 63 GHz. Phase-shifting elements have been designed, using transmission lines, which realise a relative phase shift of -120, 0 and 120 degrees. Simulations show that a 9×5-element deflector, consisting of these elements, placed in a regular pattern, is able to deflect an incoming electromagnetic wave by 34 degrees over the entire frequency band of 57 - 63 GHz. The resulting directivity at 60 GHz is 17.3 dBi and side lobes are 12.4 dB lower than the main lobe.

Two 9x9-element deflectors have been constructed in a printed circuit board technique consisting of four metal layers. One deflector is constructed of three different phase-shifting elements and deflects incident waves by 34 degrees. The second deflector is constructed of identical elements and does not change the direction of incident waves. Measurement and simulation results have been given in Chapter 7. Good agreement exists between normalised measurement and simulation results. Both deflectors behave as expected, sidelobe levels are in the order of -10 dB. Differences in gain exist between simulated and measured results. In particular, the measured gain is not as high as expected. Several reasons have been given to explain these differences.

The measurements confirm that it is possible to create a passive planar structure that is able to deflect waves and thereby able to extend the coverage of an antenna configuration.

8.2 Recommendations

In order to design a deflector that can be incorporated into a 3D structure as proposed in Chapter 1, some more research should be performed on a number of aspects.

In Chapter 6 and 7, deflector designs have been presented that are suitable for plane-wave incidence. To obtain optimal gain, the deflectors should be designed specifically to match the wavefront originating from the source. If the source is a horn antenna, for example, the deflector should be designed to match a spherical wave.

In Chapter 6, three different elements have been designed, which achieve a phase shift of -120, 0 and 120 degrees. Therefore it was only possible to create a deflector that deflects an incident wave by 34 degrees. In order to design a deflector with custom deflecting behaviour, phase-shifting elements should be designed that are able to achieve a phase shift over the whole phase range of 0-360 degrees. To achieve a custom phase shift, the principle of transmission lines could be used, but there might be another type of element that achieves the desired phase shift while remaining good transmission properties.

Once elements with custom phase shift have been designed, it is possible to design a deflector suitable for one of the scenarios presented in Chapter 2. It would be interesting to do full-wave simulations, maybe even measurements, of such a deflector and compare the results with the results presented in Chapter 2.

Another aspect that should be investigated is the effect of reflections. Even with careful design of the deflector elements and the amount of phase shift they perform, reflections remain. Currently, it is not clear what would happen with the reflected energy if the deflectors are incorporated into a 3D structure. The reflected waves could be emitted by other deflectors and have a deteriorating effect on the resulting radiation pattern, or they might even enhance it. To obtain a global idea of the effects, an approximate simulation would be sufficient. If a simulation tool with more computing power would be available, even a full-wave simulation of a 3D structure could be possible.

Finally, for the construction of a 3D structure, the polarisation sensitivity of the deflector elements should be taken into account. Depending on the source orientation, the elements might need to be rotated to align with source fields.

The accuracy of the gain measurements should be improved. Currently, the difference in measured and simulated results is too big. This is partly due to the fact that the loss of the waveguides and the amount of spurious radiation produced by the conical horn are assumed to be zero. Some parts of the calibration procedure should be given more attention, as already indicated in Chapter 7.

Appendix A

Plane waves and Fourier transform

A plane wave propagating in the positive x-direction can be written as

$$\vec{E}(\vec{r}) = \vec{E}_0 e^{j(\omega t - k_x x)}, \tag{A.1}$$

where $\vec{E}_0$ holds the amplitude and phase of the wave components and where k_x is called the *propagation constant.* In this form, the phase of the wave increases with increasing time and the wave travels in the positive x-direction if $\mathrm{Re}(k_x) > 0$.
The Fourier transform between time and frequency is defined as

$$\hat{f}(\omega) = \mathcal{F}\{f(t)\} = \int_{-\infty}^{\infty} f(t) e^{-j\omega t} dt, \tag{A.2}$$

$$f(t) = \mathcal{F}^{-1}\left\{\hat{f}(\omega)\right\} = \frac{1}{2\pi} \int_{-\infty}^{\infty} \hat{f}(\omega) e^{j\omega t} d\omega. \tag{A.3}$$

The Fourier transform between space and spatial frequency is defined as

$$\hat{f}(k_x) = \mathcal{F}\{f(x)\} = \int_{-\infty}^{\infty} f(x) e^{jk_x x} dx, \tag{A.4}$$

$$f(x) = \mathcal{F}^{-1}\left\{\hat{f}(k_x)\right\} = \frac{1}{2\pi} \int_{-\infty}^{\infty} \hat{f}(k_x) e^{-jk_x x} dk_x. \tag{A.5}$$

In this way a physical plane wave will indeed contribute to the spatial frequency domain (also called *spectral domain*) representation at a k_x, whose real part is positive.

Appendix B

Antenna Parameters

Some important characteristics of an antenna are discussed. They are the *(normalised) power pattern*, the *total radiated power*, the *average radiated power*, the *directive gain*, the *directivity*, the *power gain* and the *radiation efficiency.* We are only interested in the angular dependence, rather than the radial dependence.

The *time average radiated power,* as a function of direction (θ, ϕ), radiated by the antenna, is given by

$$P_{rad}(\theta,\phi) = \frac{|\vec{E}(r,\theta,\phi)|^2 r^2}{2Z_0} \quad [W/\ \mathrm{sr}], \tag{B.1}$$

where Z_0 is the *characteristic impedance of vacuum,* which is $Z_0 = \sqrt{\mu_0/\varepsilon_0}$. The r-dependence of $|\vec{E}(\theta,\phi,r)|$ is cancelled by the multiplication with r. A plot of Eq. (B.1) is called the antenna *power pattern.*
The *normalised power pattern* is obtained if Eq. (B.1) is divided by its maximum over (θ, ϕ), i.e.

$$\tilde{P}_{rad}(\theta,\phi) = \frac{P_{rad}(\theta,\phi)}{\max_{(\theta,\phi)}\{P_{rad}(\theta,\phi)\}}. \tag{B.2}$$

The *total radiated power* is found by integrating Eq. (B.1) over a sphere S:

$$\begin{aligned} \mathbf{P}_{rad} &= \oint_S P_{rad}(r,\theta,\phi)\ dS \\ &= \frac{1}{2Z_0}\int_{\theta=0}^{\pi}\int_{\phi=0}^{2\pi} |\vec{E}(r,\theta,\phi)|^2 r^2\ d\Omega \\ &= \frac{1}{2Z_0}\int_{\theta=0}^{\pi}\int_{\phi=0}^{2\pi} |\vec{E}(r,\theta,\phi)|^2 r^2 \sin\theta\ d\theta d\phi, \end{aligned} \tag{B.3}$$

where $d\Omega = \sin\theta\ d\theta d\phi$ is the differential *solid angle,* measured in steradian (sr).
The *average radiated power* is obtained by dividing Eq. (B.3) by the total number of solid angles, which is 4π:

$$\overline{P_{rad}} = \mathbf{P}_{rad}/4\pi. \tag{B.4}$$

For the special case of an isotropic radiator, which radiates uniformly in all directions, the following applies:

$$\begin{aligned} P_{rad,isotropic}(\theta,\phi) &= \overline{P_{rad}} \\ &= \mathbf{P}_{rad}/4\pi. \end{aligned} \tag{B.5}$$

The *directivity* is defined as the power that an antenna radiates in a particular direction, divided by the power that an isotropic radiator would radiate in that direction:

$$D(\theta,\phi) = \frac{P_{rad}(\theta,\phi)}{P_{rad,isotropic}(\theta,\phi)}$$

$$= \quad 4\pi \frac{P_{rad}(\theta, \phi)}{\mathbf{P}_{rad}}. \tag{B.6}$$

The *maximum directivity* is defined as the maximum of the directive gain over (θ, ϕ):

$$\begin{aligned} D_{max} &= \max_{(\theta,\phi)} \{D(\theta, \phi)\} \\ &= 4\pi \frac{\max_{(\theta,\phi)} \{P_{rad}(\theta, \phi)\}}{\mathbf{P}_{rad}}. \end{aligned} \tag{B.7}$$

The (maximum) directivity can be regarded as a measure for the ability of an antenna to direct radiated power in a given direction.
The *gain* is defined as the ratio of the power that a certain antenna radiates in a particular direction, divided by the input power per steradian:

$$G(\theta, \phi) = 4\pi \frac{P_{rad}(\theta, \phi)}{\mathbf{P}_{in}}. \tag{B.8}$$

The *radiation efficiency* of an antenna is defined as

$$\eta = \frac{\mathbf{P}_{rad}}{\mathbf{P}_{in}}. \tag{B.9}$$

By comparing Eq. (B.6) and (B.8), a simple relation between the directivity and gain is obtained, i.e.

$$G(\theta, \phi) = \eta D(\theta, \phi). \tag{B.10}$$

Note that this relation is valid under perfect matching conditions between source and antenna.

Appendix C

Taylor approximation

The Taylor approximation of order K ($\tilde{f}_K(\vec{x})$) for a real valued continuous, differentiable function of multiple variables ($f(\vec{x})$, $\vec{x} \in \vec{X}$), about the point $\vec{x} = \vec{x}_0$, is defined as [6]

$$\tilde{f}_K(\vec{x}) = \sum_{k=0}^{K} \left[\frac{1}{k!} \left[(\vec{x} - \vec{x}_0) \cdot \nabla_{\vec{x}'} \right]^k f(\vec{x}') \right]_{\vec{x}'=\vec{x}_0} . \tag{C.1}$$

This approximation is exact if $K \to \infty$. For finite K, the approximation is exact for $\vec{x} = \vec{x}_0$ only. For $\vec{x} \neq \vec{x}_0$, the approximation deviates from the original function. This deviation is called the *remainder* and is defined as

$$R_K(\vec{x}) = f(\vec{x}) - \tilde{f}_K(\vec{x}). \tag{C.2}$$

The domain on which the approximation is considered acceptable is defined as

$$D_K = \left\{ \vec{x} \in \vec{X} \mid |R_K(\vec{x})| < \varepsilon_a |f(\vec{x})| \right\}, \tag{C.3}$$

for a sufficiently small[1] positive real number ε_a. As the order of approximation becomes higher (larger K), the boundary of the domain, on which the approximation is acceptable, moves away from $\vec{x}_0$. We express this as

$$D_K \in D_{K+1} \quad \forall\, K. \tag{C.4}$$

A consequence of this is, that if the approximation is acceptable on D_K, it is also acceptable on D_{K-1}. Extending the approximation to a higher order can be a computationally intensive task, especially when the order of approximation is already high. Therefore, the question arises, how large K should be chosen, to obtain a *reliable* approximation. The approximation is reliable, if it can be used to find the optimum of the original function on a certain domain D_{opt}. This is possible if the approximation function has the same extrema within D_{opt} as the original function and we state that this is true, if the approximation is acceptable within D_{opt}. Therefore, K must be chosen such, that

$$D_{opt} \in D_K, \tag{C.5}$$

with ϵ_a sufficiently small. Considering the fact that the boundary of the domain, on which the approximation is acceptable, moves away from $\vec{x}_0$, Eq. (C.5) holds if the approximation is acceptable for every point in ∂D_{opt}, the boundary of D_{opt}:

$$|R_K(\vec{x})| < \varepsilon_a |f(\vec{x})| \quad \forall\, \vec{x} \in \partial D_{opt}, \tag{C.6}$$

In practice, it is not possible to verify this condition for all $\vec{x} \in \partial D_{opt}$, so we define a finite subset of *validation points*, $V \subset \partial D_{opt}$. The original function is evaluated once for every $\vec{x}_V \in V$. For every order of approximation, Eq. (C.5) is verified by evaluating Eq. (C.6) for every $\vec{x}_V \in V$.

---

[1] see the explanation under *remarks*

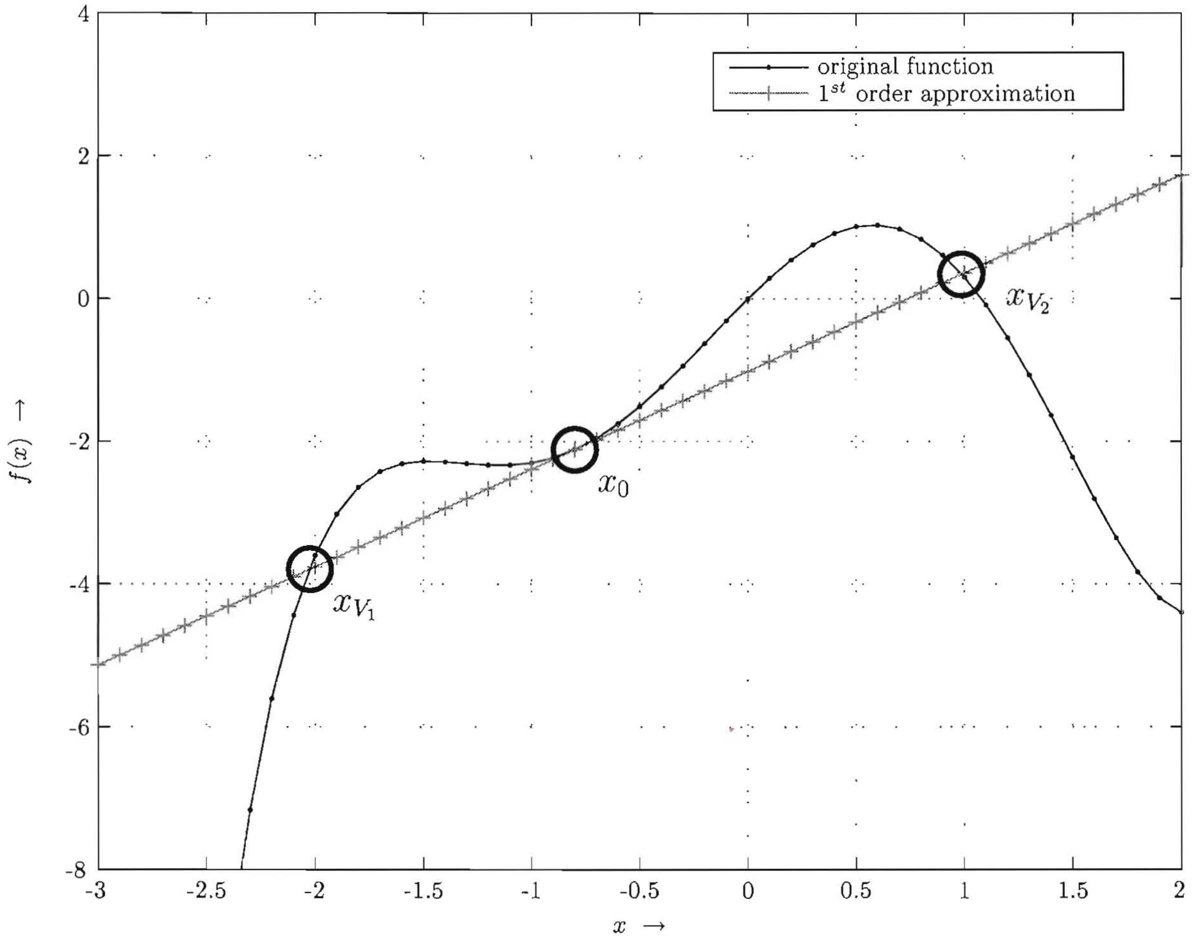

Figure C.1: False validation of a Taylor approximation

Remarks

The main text states that the approximation of order K is acceptable on D_{opt}, if, on ∂D_{opt}, the remainder is a small fraction of the original function value (Eq. (C.6)). Although this condition seems very plausible, it is not necessarily true. There are certain conditions, under which Eq. (C.6) is true, while the approximation is not acceptable. Fig. C.1 shows an example for the single-variable case. In this example, (Eq. (C.6)) is true, because the approximation function intersects the original function exactly in the validation points, while the approximation is clearly not acceptable on the entire domain $D_{opt} = \{x \in \mathbb{R} \mid x_{V_1} \leq x \leq x_{V_2}\}$. The chance of such a *false validation* can be minimised by choosing ε_a sufficiently small, and by defining multiple validation points (in a multi-variable case).

Appendix D

Plane wave incident on a grounded dielectric slab

The field solution of a plane wave, incident on a grounded dielectric slab, is considered. Assuming the incident plane wave is propagating in the z-direction and is linearly polarised along the y-direction, the field solution can be written as the sum of a forward (towards positive z) and backward (towards negative z) travelling component as

$$\begin{aligned} \vec{E}(z) &= E(z)\vec{u}_y, \\ \vec{H}(z) &= H(z)\vec{u}_x, \end{aligned} \tag{D.1}$$

with

$$\begin{aligned} E(z) &= E^+(z) + E^-(z) = E^+e^{-jkz} + E^-e^{jkz}, \\ H(z) &= \frac{1}{Z}\left[E^+(z) - E^-(z)\right] = \frac{1}{Z}\left[E^+e^{-jkz} - E^-e^{jkz}\right], \end{aligned} \tag{D.2}$$

where the '+' and '-' superscripts denote the forward and backward travelling component, respectively, and $Z = \sqrt{\mu/\varepsilon}$, the characteristic impedance of the medium. The components of the electric field at the dielectric slab are shown in Fig. (D.1). The incident fields on the slab are E_2^- and E_1^+, the scattered fields are E_2^+ and E_1^-. These fields are related according to

$$\begin{bmatrix} E_2^+ \\ E_1^- \end{bmatrix} = \begin{bmatrix} \tau_1 & \rho_2 \\ \rho_1 & \tau_2 \end{bmatrix} \begin{bmatrix} E_1^+ \\ E_2^- \end{bmatrix}, \tag{D.3}$$

where $\{\rho_1, \tau_1\}$ and $\{\rho_2, \tau_2\}$ are the elementary reflection and transmission coefficients from medium 1 to medium 2 and from medium 2 to medium 1, respectively, which can be written in terms of

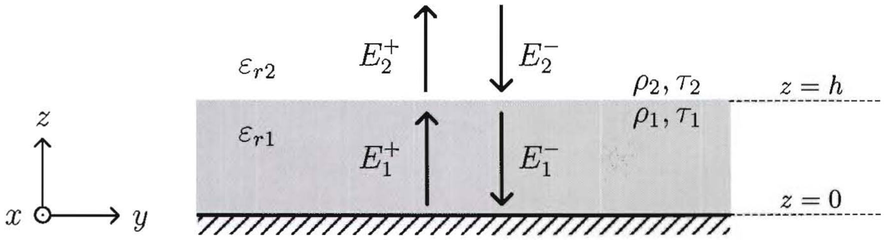

Figure D.1: Electric field components at the dielectric slab refractive indices as

$$\rho_1 = \frac{n_1 - n_2}{n_1 + n_2}, \qquad \tau_1 = \frac{2n_1}{n_1 + n_2}, \qquad \rho_2 = \frac{n_2 - n_1}{n_1 + n_2}, \qquad \tau_2 = \frac{2n_2}{n_1 + n_2}, \tag{D.4}$$

where $n = \sqrt{\varepsilon_r}$ for dielectric material. The forward and backward travelling components in medium 1 at $z = 0$ can be related to the respective components at $z = h$ according to

$$\begin{aligned} E_1^-(0) &= E_1^-(h)e^{-jk_1h}, \\ E_1^+(0) &= E_1^+(h)e^{jk_1h}. \end{aligned} \tag{D.5}$$

The forward and backward travelling components in medium 1 can be related to each other at $z = 0$ by considering the boundary condition on the ground plane, i.e. $\vec{u}_z \times \vec{E} = 0$, which results in

$$E_1^-(0) = -E_1^+(0). \tag{D.6}$$

Combining Eq. (D.5) and (D.6), the forward and backward travelling components in medium 1 can be related to each other at $z = h$ as

$$\begin{aligned} E_1^+(h) &= E_1^+(0)e^{-jk_1h} \\ &= -E_1^-(0)e^{-jk_1h} \\ &= -E_1^-(h)e^{-2jk_1h}. \end{aligned} \tag{D.7}$$

Furthermore, the backward travelling wave in medium 1 can be related to the backward travelling wave in medium 2 by (Eq. (D.3) and (D.7))

$$\begin{aligned} E_1^-(h) &= \rho_1 E_1^+(h) + \tau_2 E_2^-(h) \\ &= -\rho_1 e^{-2jk_1h} E_1^-(h) + \tau_2 E_2^-(h). \end{aligned}$$

Rearranging results in

$$\begin{aligned} (1 + \rho_1 e^{-2jk_1h})E_1^-(h) &= \tau_2 E_2^-(h) \\ E_1^-(h) &= \frac{\tau_2}{1 + \rho_1 e^{-2jk_1h}} E_2^-(h). \end{aligned} \tag{D.8}$$

We continue by evaluating the electric field at $z = h$ and the magnetic field at $z = 0$ in terms of the backward travelling wave in medium 2. Because the tangential field are continuous at the top of the dielectric slab, the electric field at $z = h$ can be evaluated in both media. In this analysis, it is evaluated in medium 1. Using Eq. (D.7) and (D.8), this yields

$$\begin{aligned} E_1(h) &= E_1^-(h) + E_1^+(h) \\ &= (1 - e^{-2jk_1h})E_1^-(h) \\ &= \frac{\tau_2(1 - e^{-2jk_1h})}{1 + \rho_1 e^{-2jk_1h}} E_2^-(h). \end{aligned} \tag{D.9}$$

The magnetic field at $z = 0$ is evaluated as (using Eq. (D.5), (D.6) and (D.8))

$$\begin{aligned} H_1(0) &= \frac{1}{Z_1}\left[E_1^+(0) - E_1^-(0)\right] \\ &= -\frac{2}{Z_1}E_1^-(0) \\ &= -\frac{2}{Z_1}e^{-jk_1h}E_1^-(h) \\ &= \frac{-2\tau_2 e^{-jk_1h}}{Z_1(1 + \rho_1 e^{-2jk_1h})} E_2^-(h). \end{aligned} \tag{D.10}$$

Appendix E

Spectral domain Green's functions of the grounded dielectric slab with magnetic sources

Consider a grounded dielectric slab of height $z = h$. Maxwell's equations with magnetic sources only in the frequency domain are given by [44]

$$\begin{aligned}
\nabla \times \vec{E}(\vec{r}) &= -j\omega\mu\vec{H}(\vec{r}) - \vec{M}(\vec{r}), \\
\nabla \times \vec{H}(\vec{r}) &= j\omega\varepsilon\vec{E}(\vec{r}) \\
\nabla \cdot \vec{E}(\vec{r}) &= 0, \\
\nabla \cdot \vec{H}(\vec{r}) &= \rho_m(\vec{r})/\mu.
\end{aligned} \tag{E.1}$$

Together with the continuity equation

$$\nabla \cdot \vec{M}(\vec{r}) + j\omega\rho_m(\vec{r}) = 0. \tag{E.2}$$

In analogy with the derivation in Chapter 3, the fields can be written in terms of the electric vector potential $\vec{F}$ and the scalar potential ϕ. Using the Lorenz gauge

$$\nabla \cdot \vec{H}(\vec{r}) = -j\omega\mu\phi(\vec{r}), \tag{E.3}$$

the fields can be expressed in terms of the electric vector potential only, i.e.

$$\begin{aligned}
\vec{E}(\vec{r}) &= -\nabla \times \vec{F}(\vec{r}), \\
\vec{H}(\vec{r}) &= \frac{-j\omega\varepsilon}{k^2}\left[k^2 + \nabla\nabla\cdot\right]\vec{F}(\vec{r}).
\end{aligned} \tag{E.4}$$

Using Eq. (E.1), (E.3) and (E.4), the Helmholtz equation for $\vec{F}$ is obtained, i.e.

$$(\nabla^2 + k^2)\vec{F}(\vec{r}) = -\vec{M}(\vec{r}). \tag{E.5}$$

The electric vector potential is related to the source magnetic current distribution through the Green's function $\bar{\bar{G}}^M(\vec{r}, \vec{r}_0)$, which is the field response due to a magnetic point source, according to

$$\vec{F}(\vec{r}) = \int_{V_0} \bar{\bar{G}}^M(\vec{r}, \vec{r}_0)\vec{M}(\vec{r}_0)\, dV_0. \tag{E.6}$$

Combining Eq. (E.4) and (E.6), the fields are written in terms of the source current distribution according to

$$\vec{E}(\vec{r}) = \int_{V_0} -\nabla \times \bar{\bar{G}}^M(\vec{r}, \vec{r}_0)\vec{M}(\vec{r}_0)\, dV_0,$$

$$\vec{H}(\vec{r}) = \int_{V_0} \frac{-j\omega\varepsilon}{k^2} \left[k^2 + \nabla\nabla\cdot\right] \bar{\bar{G}}^M(\vec{r},\vec{r}_0)\vec{M}(\vec{r}_0)\, dV_0. \tag{E.7}$$

In case of a planar source magnetic current distribution at $z = z_s$, the fields can be evaluated in the spectral domain using

$$\begin{aligned}
\vec{E}(\vec{r}) &= \frac{1}{4\pi^2}\int_{k_x}\int_{k_y} \hat{\bar{\bar{Q}}}_{EM}(k_x,k_y,z)\hat{\vec{\Psi}}(k_x,k_y)e^{-jk_x x}e^{-jk_y y}\, dk_x dk_y,\\
\vec{H}(\vec{r}) &= \frac{1}{4\pi^2}\int_{k_x}\int_{k_y} \hat{\bar{\bar{Q}}}_{HM}(k_x,k_y,z)\hat{\vec{\Psi}}(k_x,k_y)e^{-jk_x x}e^{-jk_y y}\, dk_x dk_y,
\end{aligned} \tag{E.8}$$

where $\hat{\vec{\Psi}}(k_x, k_y)$ is the spectral-domain form of the planar source magnetic current distribution and $\hat{\bar{\bar{Q}}}(k_x, k_y, z)$ the spectral domain dyadic Green's function that links the fields to the planar source magnetic current distribution at $z = z_s$. The fixed source coordinate is omitted from the argument list. The Green's function $\bar{\bar{G}}^M(\vec{r}, \vec{r}_0)$ is found by solving the Helmholtz equation (Eq. (E.5)), using (Eq. (E.6)), for $\vec{M}(\vec{r}) = \vec{u}_i\delta(\vec{r} - \vec{r}_0)$, with i equal to x, y or z, and applying the boundary conditions of the dielectric slab. Then the spectral domain equations (Eq. (E.8)) are obtained form the spatial domain equations (Eq. (E.7)) by Fourier transformation.

We are interested in the Green's functions that link electric and magnetic fields in the slab to magnetic current sources at the boundary of the slab. If we only consider a magnetic current distribution $\vec{M}_0$ on $z = 0$, which is at the lower boundary of the slab, the Helmholtz equation for fields in the slab becomes (Eq. (E.5))

$$(\nabla^2 + k^2)\vec{F}(\vec{r}) = \vec{0}, \tag{E.9}$$

and the boundary conditions become

$$\begin{aligned}
\vec{u}_z \times \vec{E}_1 &= -\vec{M}_0 & & z = 0,\\
\left.\begin{aligned}\vec{u}_z \times \vec{E}_1 &= \vec{u}_z \times \vec{E}_2\\ \vec{u}_z \times \vec{H}_1 &= \vec{u}_z \times \vec{H}_2\end{aligned}\right\} & & & z = h,
\end{aligned} \tag{E.10}$$

where $z = h$ is the location of the interface between the dielectric slab and the background medium. Assuming we need to link y-directed electric field at $z = h$ and x-directed magnetic field at $z = 0$ to x-directed source magnetic current at $z = 0$, this can be done by means of Green's function components, which are found by substituting Eq. (E.7) into the boundary conditions (Eq. (E.10)), with $\bar{\bar{G}}^M(\vec{r}, \vec{r}_0)$ found by solving the Helmholtz equation (Eq. (E.9)). This is the same approach as followed in Chapter 3. The resulting Green's function components are

$$\hat{Q}_{EMyx}(k_x,k_y,h) = \frac{1}{T_e T_m}\left[k_{z1}T_m + jk_y^2(\varepsilon_{r2} - \varepsilon_{r1})\sin(k_{z1}h)\right], \tag{E.11}$$

$$\begin{aligned}
\hat{Q}_{HMxx}(k_x,k_y,0) &= \frac{1}{Z_0 k_0 k_{z1} T_e T_m}\left[(\varepsilon_{r1} - \varepsilon_{r2})k_x^2 k_{z1}^2 - \right.\\
&\quad \left.(k_1^2 - k_x^2)(\varepsilon_{r2}k_{z1}\cos(k_{z1}h) + j\varepsilon_{r1}k_{z2}\sin(k_{z1}h)T_e)\right],
\end{aligned} \tag{E.12}$$

where the *vacuum impedance* $Z_0 = \sqrt{\mu_0/\varepsilon_0}$ and the other terms as defined in Chapter 3. Linking the respective fields to source electric current at $z = h$ is done by means of the Green's function components

$$\hat{Q}_{EJyy}(k_x,k_y,h) = -j\frac{Z_0\sin(k_{z1}h)}{k_0 T_e T_m}\left[k_0^2 T_m - k_y^2(k_{z2}\cos(k_{z1}h) + jk_{z1}\sin(k_{z1}h))\right], \tag{E.13}$$

$$\hat{Q}_{HJxy}(k_x,k_y,0) = -\frac{1}{T_e T_m}\left[k_{z1}T_m + jk_y^2(\varepsilon_{r2} - \varepsilon_{r1})\sin(k_{z1}h)\right]. \tag{E.14}$$

Appendix F

Complex element-wise product

The complex element-wise product is an operation that acts on 2 complex numbers to yield a new complex number.

F.1 Definition

The complex element-wise product ($\circledast$) of two complex numbers A and B is defined as

$$A \circledast B = \Re(A)\Re(B) + j\Im(A)\Im(B), \tag{F.1}$$

where $\Re(\cdot)$ and $\Im(\cdot)$ denote the real and imaginary part, respectively.
Furthermore, the *element-wise sum* of a complex numbers A is defined as

$$\{A\} = \Re(A) + \Im(A), \tag{F.2}$$

F.2 Properties

Some useful properties of the '$\circledast$' operator are:

F.2.1 Commutativity

The '$\circledast$' operator exhibits commutativity:

$$\begin{aligned} A \circledast B &= \Re(A)\Re(B) + j\Im(A)\Im(B) \\ &= \Re(B)\Re(A) + j\Im(B)\Im(A) \\ &= B \circledast A. \end{aligned} \tag{F.3}$$

F.2.2 Associativity

The '$\circledast$' operator exhibits associativity:

$$\begin{aligned} A \circledast (B \circledast C) &= A \circledast (\Re(B)\Re(C) + j\Im(B)\Im(C)) \\ &= \Re(A)\Re(B)\Re(C) + j\Im(A)\Im(B)\Im(C) \\ &= (\Re(A)\Re(B) + j\Im(A)\Im(B)) \circledast C \\ &= (A \circledast B) \circledast C. \end{aligned} \tag{F.4}$$

F.2.3 Distributivity

The '$\circledast$' operator exhibits distributivity over addition:

$$\begin{aligned}
A \circledast (B + C) &= A \circledast (\Re(B) + j\Im(B) + \Re(C) + j\Im(C)) \\
&= A \circledast ([\Re(B) + \Re(C)] + j[\Im(B) + \Im(C)]) \\
&= \Re(A)[\Re(B) + \Re(C)] + j\Im(A)[\Im(B) + \Im(C)] \\
&= \Re(A)\Re(B) + j\Im(A)\Im(B) + \Re(A)\Re(C) + j\Im(A)\Im(C) \\
&= A \circledast B + A \circledast C. \qquad \text{(F.5)}
\end{aligned}$$

F.2.4 Derivation

If f_A and f_B are two (analytic) complex functions, the '∇' operator (derivation) exhibits distributivity over the $\circledast$ operator:

$$\begin{aligned}
\nabla(f_A \circledast f_B) &= \nabla\left[\Re(f_A)\Re(f_B) + j\Im(f_A)\Im(f_B)\right] \\
&= [(\nabla\Re(f_A))\Re(f_B) + \Re(f_A)(\nabla\Re(f_B))] + j\left[(\nabla\Im(f_A))\Im(f_B) + \Im(f_A)(\nabla\Im(f_B))\right] \\
&= [(\nabla\Re(f_A))\Re(f_B) + j(\nabla\Im(f_A))\Im(f_B)] + [\Re(f_A)(\nabla\Re(f_B)) + j\Im(f_A)(\nabla\Im(f_B))] \\
&= (\nabla f_A) \circledast f_B + f_A \circledast (\nabla f_B). \qquad \text{(F.6)}
\end{aligned}$$

This property is very similar to the ordinary product rule, which states that

$$\nabla(f_A \cdot f_B) = (\nabla f_A) \cdot f_B + f_A \cdot (\nabla f_B), \qquad \text{(F.7)}$$

which is the basis for the Leibniz rule [1] to calculate the n^{th} order derivation of a product of two functions. This similarity enables us to calculate the n^{th} order derivation of a complex element-wise product of two complex functions, through a slightly modified Leibniz rule:

$$\nabla^n(f_A \circledast f_B) = \sum_{k=0}^{n} \binom{n}{k} (\nabla^k f_A) \circledast (\nabla^{n-k} f_B). \qquad \text{(F.8)}$$

The '∇' (derivation) and '$\{\cdot\}$' (element-wise sum) operators can be interchanged:

$$\begin{aligned}
\nabla\{f_A\} &= \nabla(\Re(f_A) + \Im(f_A)) \\
&= \nabla\Re(f_A) + \nabla\Im(f_A) \\
&= \Re(\nabla f_A) + \Im(\nabla f_A) \\
&= \{\nabla f_A\}. \qquad \text{(F.9)}
\end{aligned}$$

F.2.5 Relation with ordinary modulus

The element-wise sum of the complex element-wise product of two complex numbers A and B results in

$$\begin{aligned}
\{A \circledast B\} &= \{\Re(A)\Re(B) + j\Im(A)\Im(B)\} \\
&= \Re(A)\Re(B) + \Im(A)\Im(B). \qquad \text{(F.10)}
\end{aligned}$$

If $B = A$, Eq. (F.10) reduces to the following relation:

$$\begin{aligned}
\{A \circledast A\} &= \Re(A)^2 + \Im(A)^2 \\
&= |A|^2, \qquad \text{(F.11)}
\end{aligned}$$

where $|\cdot|$ denotes the ordinary modulus, i.e. the absolute value of the complex number A.

Acknowledgments

I would like to thank my supervisor Iwan Akkermans for his great help in completing this project. A lot of good ideas in this work find their origin in the many fruitful discussions between the two of us. So thanks a lot for being a great supervisor and such a fun person to be with!
I would also like to thank Peter Smulders for his guidance during my graduation period and for introducing me into the SiGi-Spot project. Furthermore, I would like to thank Matti Herben for his helpful discussions and suggestions. I would like to thank the people of TNO Defence, Safety and Security in The Hague for the opportunity to do the measurements and to use their equipment.
Finally, I want to thank everybody else in the Radio Communications group of the Eindhoven University of Technology for their help and for being such nice people to work with. Thank you all very much!

Bibliography

[1] M. Abramowitz and I.A. Stegun, *Handbook of Mathematical Functions with Formulas, Graphs, and Mathematical Tables*, p. 12, Dover, New York, 1972.

[2] J.A.G. Akkermans, M.C. van Beurden, and M.H.A.J. Herben, *Design of a millimeter-wave balanced-fed aperture-coupled patch antenna*, proc. EuCap 2006, ESA SP626 (Nice, France).

[3] J.A.G. Akkermans, R. van Dijk, and M.H.A.J. Herben, *Millimeter-wave antenna measurements (to be published)*, proc. European Microwave Conference, October 2007 (München, Germany).

[4] J.A.G. Akkermans and M.H.A.J. Herben, *Planar beam-forming array for millimetre-wave transceivers (to be published)*, proc. European Conference on Antennas and Propagation, November 2007 (Edinburgh, UK).

[5] R.J. Allard, D.H. Werner, and P.L. Werner, *Radiation pattern synthesis for arrays of conformal antennas mounted on arbitrarily-shaped three-dimensional platforms using genetic algorithms*, IEEE Transactions on Antennas and Propagation **51** (2003), no. 5, 1054–1062.

[6] G. Arfken, *Mathematical Methods for Physicists*, pp. 303–313, London: Academic Press, 1985.

[7] D. Berry, R. Malech, and W. Kennedy, *The reflectarray antenna*, IEEE Transactions on Antennas and Propagation [legacy, pre-1988] **11** (1963), no. 6, 645–651.

[8] D.C. Chang and M.C. Huang, *Microstrip reflectarray antenna with offset feed*, Electronics Letters **28** (1992), no. 16, 1489–1491.

[9] B. Chantraine-Bares, R. Sauleau, L. Le Coq, and K. Mahdjoubi, *A new accurate design method for millimeter-wave homogeneous dielectric substrate lens antennas of arbitrary shape*, IEEE Transactions on Antennas and Propagation **53** (2005), no. 3, 1069–1082.

[10] N.S. Cheng, A. Alexanian, M.G. Case, D.B. Rensch, and R.A. York, *40-W CW broad-band spatial power combiner using dense finlinearrays*, IEEE Transactions on Microwave Theory and Techniques **47** (1999), no. 7 Part 1, 1070–1076.

[11] W.C. Chew, *Waves and Fields in Inhomogeneous Media*, IEEE Press New York, 1995.

[12] N.K. Das and D.M. Pozar, *A generalized spectral-domain Green's function for multilayer dielectric substrates with application to multilayer transmission lines*, IEEE Transactions on Microwave Theory and Techniques **35** (1987), no. 3, 326–335.

[13] G.V. Eleftheriades, Y. Brand, J.F. Zurcher, and J.R. Mosig, *ALPSS: a millimetre-wave aperture-coupled patch antenna on asubstrate lens*, Electronics Letters **33** (1997), no. 3, 169–170.

[14] J.A. Encinar, *Design of two-layer printed reflectarrays using patches of variablesize*, IEEE Transactions on Antennas and Propagation **49** (2001), no. 10, 1403–1410.

[15] C. Fernandes, V. Brankovic, S. Zimmermann, M. Filipe, and L. Anunciada, *Dielectric Lens Antennas for Wireless Broadband Communications*, Wireless Personal Communications **10** (1999), no. 1, 19–32.

[16] C.A. Fernandes and L.M. Anunciada, *Constant flux illumination of square cells for millimeter-wavewireless communications*, IEEE Transactions on Microwave Theory and Techniques **49** (2001), no. 11, 2137–2141.

[17] C.A. Fernandes and J.G. Fernandes, *Performance of lens antennas in wireless indoor millimeter-wave applications*, IEEE Transactions on Microwave Theory and Techniques **47** (1999), no. 6, 732–737.

[18] J.A. Ferreira and F. Ares, *Pattern synthesis of conformal arrays by the simulated annealing technique*, Electronics Letters **33** (1997), no. 14, 1187–1189.

[19] A. Glisson and D. Wilton, *Simple and efficient numerical methods for problems of electromagnetic radiation and scattering from surfaces*, IEEE Transactions on Antennas and Propagation [legacy, pre-1988] **28** (1980), no. 5, 593–603.

[20] G. Godi, R. Sauleau, and D. Thouroude, *Performance of reduced size substrate lens antennas for Millimeter-wave communications*, IEEE Transactions on Antennas and Propagation **53** (2005), no. 4, 1278–1286.

[21] R.F. Harrington, *Time-Harmonic EM Fields*, McGraw-Hill Classic Textbook Reissue Series, 1961.

[22] ______, *Field Computation by Moment Methods*, Krieger Publishing Co., Inc. Melbourne, FL, USA, 1982.

[23] J. Huang, *Microstrip reflectarray*, Antennas and Propagation Society International Symposium, 1991. AP-S. Digest (1991), 612–615.

[24] J. Hubert, J. Schoenberg, and Z.B. Popovic, *High-power hybrid quasi-optical Ka-band amplifier design*, Microwave Symposium Digest, 1995 IEEE MTT-S International **2** (1995), 585–588.

[25] T. Ivanov, S. Ortiz, A. Mortazawi, E. Schlecht, and J. Hubert, *A passive double-layer microstrip array for the construction of millimeter-wave spatial power-combining amplifiers*, Microwave and Guided Wave Letters, IEEE [see also IEEE Microwave and Wireless Components Letters] **7** (1997), no. 11, 365–367.

[26] R.D. Javor, X.D. Wu, and K. Chang, *Design and performance of a microstrip reflectarray antenna*, IEEE Transactions on Antennas and Propagation **43** (1995), no. 9, 932–939.

[27] I. Jayakumar, R. Garg, B. Sarap, B. Lal, E. Res, D. Establishment, and I. Bangalore, *A conformal cylindrical microstrip array for producing omnidirectional radiation pattern*, IEEE Transactions on Antennas and Propagation [legacy, pre-1988] **34** (1986), no. 10, 1258–1261.

[28] S.S.D. Jones, H. Gent, and A.A.L. Browne, *Electromagnetic wave lens and mirror systems*, 1961, United States Patent US Pat. 2986734.

[29] K. Lam, S. Kwok, Y. Hwang, and T.K. Lo, *Implementation of transmitarray antenna concept by using aperture-coupled microstrip patches*, proc. Asia Pacific Microwave Conference 1997 (Asia Pacific), pp. 433–436.

[30] K.A. Michalski, *Extrapolation methods for Sommerfeld integral tails*, IEEE Transactions on Antennas and Propagation **46** (1998), no. 10, 1405–1418.

[31] K.A. Michalski and D. Zheng, *Electromagnetic scattering and radiation by surfaces of arbitraryshape in layered media. I. Theory*, IEEE Transactions on Antennas and Propagation **38** (1990), no. 3, 335–344.

[32] R. Mittra, C.H. Chan, and T. Cwik, *Techniques for analyzing frequency selective surfaces-a review*, Proceedings of the IEEE **76** (1988), no. 12, 1593–1615.

[33] R. Munson, *Conformal microstrip antennas and microstrip phased arrays*, IEEE Transactions on Antennas and Propagation [legacy, pre-1988] **22** (1974), no. 1, 74–78.

[34] S. Ortiz, J. Hubert, L. Mirth, E. Schlecht, and A. Mortazawi, *A 25 watt and 50 watt Ka-band quasi-optical amplifier*, Microwave Symposium Digest., 2000 IEEE MTT-S International **2** (2000).

[35] S.C. Ortiz, T. Ivanov, and A. Mortazawi, *A CPW-fed microstrip patch quasi-optical amplifier array*, IEEE Transactions on Microwave Theory and Techniques **48** (2000), no. 2, 276–280.

[36] D.N. Pattanayak and E. Wolf, *General form and a new interpretation of the Ewald-Oseen extinction theorem*, Optics Communications **6** (1972), no. 3, 217–220.

[37] R. Pous and D.M. Pozar, *A frequency-selective surface using aperture-coupled microstrip patches*, IEEE Transactions on Antennas and Propagation **39** (1991), no. 12 Part 1, 1763–1769.

[38] D.M. Pozar, *Flat lens antenna concept using aperture coupled microstrip patches*, Electronics Letters **32** (1996), no. 23, 2109–2111.

[39] D.M. Pozar and T.A. Metzler, *Analysis of a reflectarray antenna using microstrip patches of variable size*, Electronics Letters **29** (1993), no. 8, 657–658.

[40] D.M. Pozar and D.H. Schaubert, *Scan blindness in infinite phased arrays of printed dipoles*, IEEE Transactions on Antennas and Propagation **32** (1984), 602–610.

[41] D.M. Pozar, S.D. Targonski, and H.D. Syrigos, *Design of millimeter wave microstrip reflectarrays*, IEEE Transactions on Antennas and Propagation **45** (1997), no. 2, 287–296.

[42] S. Roman, *The Formula of FAA Di Bruno*, The American Mathematical Monthly **87** (1980), no. 10, 805–809.

[43] S. Romisch, D. Popovic, N. Shino, R. Lee, and Z. Popovic, *Multi-beam discrete lens arrays with amplitude-controlled steering*, Microwave Symposium Digest, 2003 IEEE MTT-S International **3** (2003).

[44] E.J. Rothwell and M.J. Cloud, *Electromagnetics*, p. 59, CRC Press, 2001.

[45] W. Rusch, *The current state of the reflector antenna art*, IEEE Transactions on Antennas and Propagation [legacy, pre-1988] **32** (1984), no. 4, 313–329.

[46] A.B. Smolders, *Microstrip Phased-Array Antennas: a Finite-Array Approach*, Ph.D. thesis, Eindhoven University of Technology, 1994.

[47] P.F.M. Smulders, *SiGi Spot: 60 GHz radio technology for high-capacity wireless in-home communication networks*, http://www.sigi-spot.nl.

[48] A. Sommerfeld, *Partial differential equations in physics*, Academic Press New York, 1949.

[49] D. Staiman, M. Breese, and W. Patton, *New technique for combining solid-state sources*, Solid-State Circuits, IEEE Journal of **3** (1968), no. 3, 238–243.

[50] F.C.E. Tsai and M.E. Bialkowski, *Investigations into the design of a spatial power combiner employing a planar transmitarray of stacked patch antennas*, 15th International Conference on Microwaves, Radar and Wireless Communications, 2004. MIKON-2004 **2** (2004).

[51] M.J.M. van der Vorst, *Integrated Lens Antennas for Submillimetre-wave Applications*, Technische Universiteit Eindhoven, 1999.

[52] M. Vrancken and G.A.E. Vandenbosch, *Semantics of dyadic and mixed potential field representation for 3-D current distributions in planar stratified media*, IEEE Transactions on Antennas and Propagation **51** (2003), no. 10, 2778–2787.

[53] J.R. Wait, *Electromagnetic waves in stratified media*, Pergamon, 1962.

[54] X. Wu, G.V. Eleftheriades, and T.E. van Deventer-Perkins, *Design and characterization of single-and multiple-beam mm-wavecircularly polarized substrate lens antennas for wireless communications*, IEEE Transactions on Microwave Theory and Techniques **49** (2001), no. 3, 431–441.